On topological Properties of Superconducting Nanowires

Pikulin, D.

On topological properties of superconducting nanowires

Proefschrift

ter verkrijging van
de graad van Doctor aan de Universiteit Leiden,
op gezag van Rector Magnificus
Prof. Mr. C. J. J. M. Stolker,
volgens besluit van het College voor Promoties
te verdedigen op dinsdag 26 november 2013
klokke 11.15 uur

door

Dmitry Igorevich Pikulin

geboren te Arsamas-16, Sovjet-Unie in 1987

Promotiecommissie

Promotores:	Prof. dr. C. W. J. Beenakker
	Prof. dr. Yu. V. Nazarov (Technische Universiteit Delft)
Overige leden:	Prof. dr. E. R. Eliel
	Prof. dr. ir. L. P. Kouwenhoven (Technische Universiteit Delft)
	Prof. dr. H. Schomerus (Lancaster University)
	Prof. dr. J. Zaanen

Casimir PhD Series 2013-29
ISBN 978-90-8593-170-6

Dit werk maakt deel uit van het onderzoekprogramma van de Stichting voor Fundamenteel Onderzoek der Materie (FOM), die deel uit maakt van de Nederlandse Organisatie voor Wetenschappelijk Onderzoek (NWO).

This work is part of the research programme of the Foundation for Fundamental Research on Matter (FOM), which is part of the Netherlands Organisation for Scientific Research (NWO).

Cover: *Dependence of the Andreev conductance in a narrow spin-orbit wire on the angle of applied magnetic field (horizontal axis) and the bias voltage. Compare with the right panel of Fig. 4.7.*

To Elena, to my parents, grandparents and all my family
Лене, моим родителям, бабушке с дедушкой и всей моей большой семье

Contents

Chapter 1

Introduction

1.1 Preface

There are many concepts in quantum mechanics that are counter-intuitive from the everyday life perspective. They range from the Heisenberg uncertainty principle to the concept of entangled states. Recently the collection has been enriched by the topological states of matter. They have intrinsic "skin effect", so that all the particle current flows on their surface, while the bulk of the material is insulating. This property does not depend on the exact details of a sample, disorder, etc. This is the reason the states are called topological. The first example of such states is the 2d Quantum Hall effect [1]. Later ones are Quantum Spin Hall [2–4] effect, 3d Topological Insulators [5–7] and Topological Superconductors [8, 9]. The results of the first experiments observing Quantum Hall and Spin Hall effects are in fig. 1.1. All the effects can be described in the framework of non-interacting quasiparticles above the Fermi sea. Based on this observation, the general classification of such topological states is constructed [10].

The most vivid example of the counter-intuitive structure of such materials is the Majorana fermion, which emerges on the boundary of a topological superconductor [11, 12] or in half-integer vortices in the topological superconductors [13, 14]. Majorana fermion is neither an electron nor a hole (absence of electron), it is half-electron half-hole at the same time. No classical analogy helps to understand this quasiparticle, as a half-empty glass is not an empty and a filled glass simultaneously. It is not a state that is empty in half of the cases and filled in

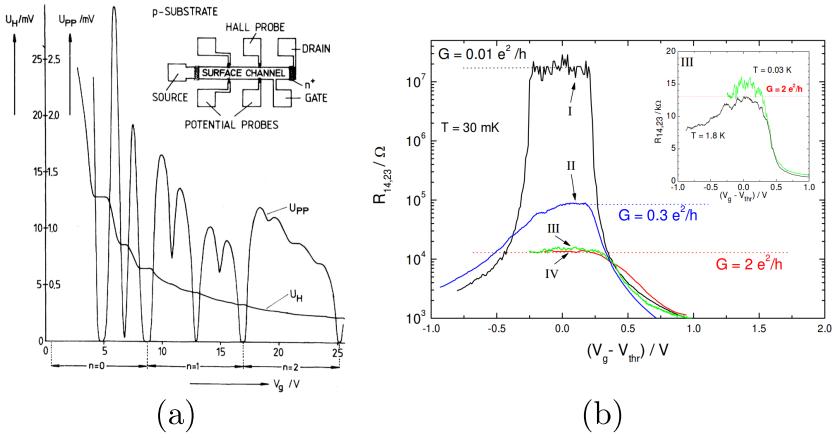

Figure 1.1. First measurements of the two topological systems in 2 dimensions. (a) Quantum Hall effect [1] conductance measurement as a function of gate voltage. The gate tunes through the plateaus for the Hall voltage (U_H) and dips in the voltage along the device (U_{PP}). (b) Quantum Spin Hall effect [4] conductance measurement as a function of gate voltage, tuning through the bandstructure of the material and showing quantized conductance in the bulk gap. Reprinted with permission from AAAS.

the other half. Rather it can be understood literally as a state, which is half of an electron and half of a hole at the same time. Only by bringing it together with another Majorana, it can really be measured if the combination of them is a full electron or a full hole. This property protects the state from any kind of local potential perturbation and makes devices based on it good candidates for a quantum memory [15] and quantum computations [16–18]. The name "Majorana fermion" comes from high-energy physics, where it refers to a freely moving elementary particle. In the superconducting context the Majorana is bound at zero energy to some defect (vortex or boundary), and is more precisely called "Majorana bound state" or "Majorana zero-mode". The combined object (Majorana plus defect) is actually not a fermion but a more exotic object called a "non-Abelian anyon" [19].

Majorana fermions are predicted to emerge on the boundary of both 1d and 2d topological superconductors [9, 10, 20–22]. They can be either propagating or localized excitations. As the title of the present thesis suggests, we deal with the 1d examples, which are bound states, in the setups of realistic quantum wires. The Majorana bound states are pre-

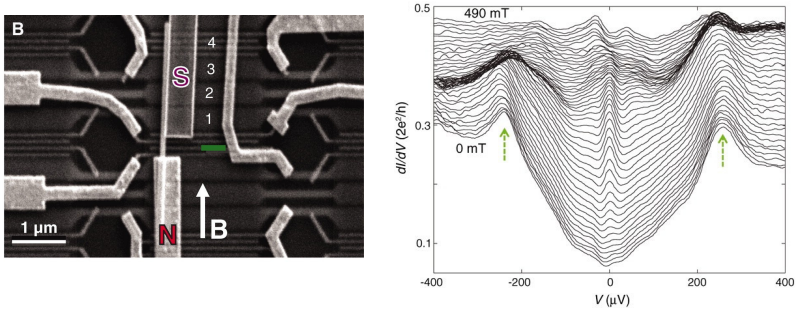

Figure 1.2. The first measurement of conductance for a spin-orbit coupled nanowire (setup on the left), showing zero-bias conductance peak, taken from [23]. The setup is very similar to the one we study in the chapter 4. Reprinted with permission from AAAS.

dicted to emerge in spin-orbit coupled nanowires under external magnetic field and in contact with the usual s-wave superconductors [21, 22]. Recently the predictions have found supporting experimental evidence [23–26]. Measurement from [23] is shown in fig. 1.2.

We start by examining the topological transition in finite wires and show that though it becomes a crossover there is a transition of different kind, which stays sharp. Then using model-independent techniques we study the wires in the vicinity of the two transitions, where their properties become universal. We study the effect of disorder in the nanowires also in a model-independent way. Then we discuss Josephson junctions with Majorana bound states of different lengths and in different setups: voltage biased short junction and phase biased long junction. We finish with a detour into the theory of Nernst effect in materials with anisotropic scattering and Fermi-surfaces.

1.2 Majorana bound state

Let us introduce the notion of the Andreev bound state. It is a state, which is localized in the vicinity of the superconductor and the wavefunction of which has both electron and hole component. Majorana bound state is a particular type of the Andreev bound state, when the

electron and hole component have equal weights:

$$\gamma_1 = \psi + \psi^\dagger, \tag{1.1}$$

$$\gamma_2 = i(\psi - \psi^\dagger), \tag{1.2}$$

where ψ is the electron annihilation operator and γ is the Majorana operator:

$$\gamma = \gamma^\dagger. \tag{1.3}$$

Particle-hole symmetry in the superconductors connects the creation and annihilation operators at energies $\pm E$ counted from the middle of the superconducting gap and requires:

$$\gamma(E) = \gamma^\dagger(-E), \tag{1.4}$$

therefore Majorana bound state can only appear at zero energy, in the middle of the gap.

1.2.1 Systems for observing Majorana bound state

In this thesis we will study two systems, where the Majorana bound state may emerge: the edge of the Quantum Spin Hall insulator and the spin-orbit nanowire in an external magnetic field, both coupled by proximity effect to the usual s-wave superconductor.

For the purposes of the present thesis it is important to know that the Quantum Spin Hall insulator can be thought of as two copies of the Quantum Hall systems with opposite magnetic fields, so that they are time-reversal partners of each other. This means that the Quantum Spin Hall system also has insulating bulk, but two copies of the Quantum Hall chiral edges. They are going in the opposite directions and are forming a Kramers pair. The latter forbids the scattering from one state to counter-propagating if the time-reversal symmetry is preserved. The dispersion of one edge of the Quantum Spin Hall insulator is shown in fig. 1.3.

Superconductor in proximity with the Quantum Spin Hall edge opens the gap in the edge dispersion, but the argument above still holds and it is forbidden to scatter from the right-moving to the left-moving state of an electron. Nevertheless, the superconductor opens up another possibility for backscattering: Andreev reflection [27]. It is the process of

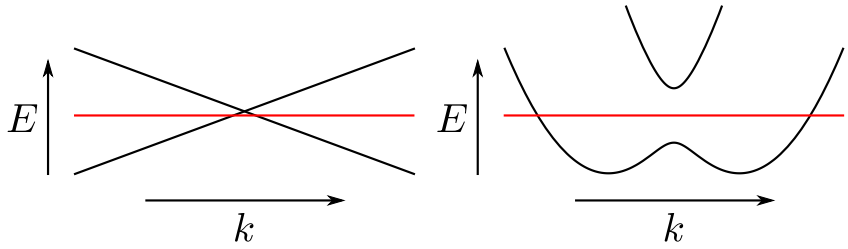

Figure 1.3. Schematic depiction of the dispersion relation of the edge states of the Quantum Spin Hall insulator (left) and the lowest band of the single-channel spin-orbit nanowire (right), the two materials being used for the detection of the Majorana fermions. The Fermi level is shown with the horizontal red line

an incident electron reflecting back as a hole and transferring a Cooper pair into the superconductor. As described above, the normal reflection is forbidden in the Quantum Spin Hall system and there is an ideal Andreev reflection. It turns out that if one breaks time-reversal symmetry, the ideal Andreev reflection is lost except at zero bias. The zero-bias peak in Andreev conductance is one of the signatures of Majorana bound state [28, 29]. It is clear that the Andreev bound state near the normal metal-superconductor boundary in such a system will have the Majorana nature, as the Andreev reflection is perfect, the wavefunction of the state is forced to be equally electron- and hole-like. Schematically the arrangement is shown in fig. 1.4.

What is the similarity between the Quantum Spin Hall edge and the spin-orbit nanowire, the other setup we discuss in the thesis? It turns out that the crucial factor for the Majoranas to emerge is the non-degenerate conducting channel, which is obviously the case for the Quantum Spin Hall system. For the nanowire one needs quite strong spin-orbit coupling in combination with the external magnetic field to completely lift the degeneracy [21, 22]. Sketch of the dispersion relation is shown in fig. 1.3. In the nanowires one also expects to observe the Majorana-related zero-bias peak, first measurements have been reported [23–25].

The analysis of the conductance properties of the non-interacting normal-superconductor junctions is very convenient to perform with the scattering matrix formalism. Scattering matrices are powerful tools for describing the non-interacting systems [30]. Once we know the scattering matrix of the system, we can understand the conductance of it

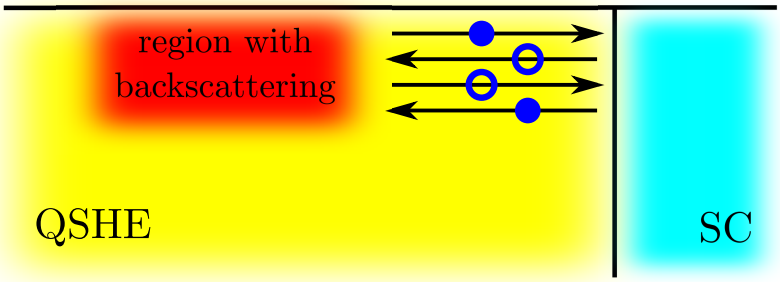

Figure 1.4. Majorana bound state formation on the edge of the Quantum Spin Hall insulator in between the region of backscattering, where time-reversal symmetry is broken, and the superconductor, which provides the Andreev reflection

both in usual and superconducting cases [31] and we apply them for the latter in the present thesis. The conductance from normal lead to the superconductor via the Andreev process is calculated as:

$$G = \frac{2e^2}{h} \mathrm{Tr}\, r_A r_A^\dagger, \tag{1.5}$$

where r_A is the subblock of the scattering matrix, corresponding to the Andreev reflection. Majorana resonant Andreev reflection manifests itself in the eigenvalue 1 of the reflection matrix at zero energy. In this thesis we will analyse the general topological properties of the scattering matrix and will use the random scattering matrix to model disordered normal-superconductor junction.

1.2.2 4π Josephson effect

Josephson effect is the phenomenon of current going between the two superconductors connected by a piece of normal metal [32]. The current may flow without resistivity if it is not too large, or if one applies voltage to the junction between the superconductors, the current is modulated with Josephson frequency [33].

Majorana bound states when present in the Josephson junction, i.e. when the weak link in the junction is the spin-orbit wire or the Quantum Spin Hall edge, has a peculiar quasi-equilibrium property: the dependence of the energy of the ground state of the junction is 4π periodic in

the superconducting phase difference between the sides of the junction [15]. By quasi-equilibrium we mean that the measurement is done faster than the parity relaxation time, or inverse tunnelling rate through one of the superconducting contacts. This is true in the current- or phase-biased case, which are discussed in the chapter 6. In the voltage-biased case, however small the tunnelling is, it affects the periodicity of the modulated current, which is discussed in the chapter 5.

The current through the Josephson junction can be calculated using the scattering matrix approach in two ways: one can derive from the scattering matrix the phenomenological Hamiltonian of the junction and study its dynamics (see chapter 5), or use the scattering matrix directly to obtain the density of states in the junction and therefore the free energy (see chapter 6). In either case it is used that the charge and superconducting phase difference are the conjugate variables and the current I can be expressed as:

$$I = \frac{2e}{\hbar}\frac{\partial F}{\partial \phi}, \tag{1.6}$$

where F is the free energy of the junction and ϕ is the superconducting phase difference between the two leads.

1.3 Symmetries

We will turn to the general classification of the topological states to understand what is the position of the topological superconductors in the classification.

The basis of the theory of a topological insulator or a superconductor is the symmetry it obeys [10]. There is a range of unitary symmetries, which a Hamiltonian can have. These include crystallographic symmetries, inversion symmetry, etc. They may also influence the classification of the Topological insulators [34], but the most important symmetries are the anti-unitary ones, time-reversal and particle-hole, and their combination, chiral symmetry. Their operators read:

$$\mathcal{T} = U_T K, \tag{1.7}$$

$$\mathcal{P} = U_P K, \tag{1.8}$$

$$\mathcal{C} = U_T U_P^*, \tag{1.9}$$

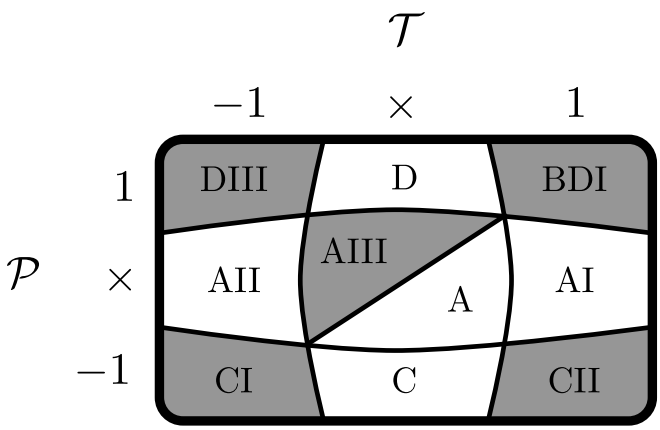

Figure 1.5. Symmetry classes of non-interacting fermions as defined by their symmetries. Numbers indicate the value of the square of the corresponding symmetry, $\times$ means the symmetry is absent. Gray areas represent symmetry classes with chiral symmetry.

where U_T and U_P are basis-dependent unitary hermitian matrices.

Though the particle-hole and the time-reversal symmetries look the same in the previous equation, they are separated by their action on the Hamiltonian:

$$\mathcal{T}H\mathcal{T}^{-1} = H, \tag{1.10}$$

$$\mathcal{P}H\mathcal{P}^{-1} = -H, \tag{1.11}$$

$$\mathcal{C}H\mathcal{C}^{-1} = -H. \tag{1.12}$$

If the symmetry is present for a system, further classification is based on the value of the $\mathcal{T}^2$ ($U_T U_T^*$) and $\mathcal{P}^2$ ($U_P U_P^*$), both can be ± 1. The simple way to see the difference between the two cases is to notice that not any Hamiltonian may be brought to the basis, where the time-reversal or particle-hole is purely complex conjugation just by rotating it with $\sqrt{U_T}$ or $\sqrt{U_P}$ correspondingly, only the ones that square to $+1$.

By this classification all the non-interacting fermion systems may be divided into 10 classes, see fig. 1.5. We will later on refer to them by the names in the table (D, BDI, CII, etc.).

These symmetries are usually based on the physical time-reversal symmetry ($\mathcal{P}^2 = -1$) and on the particle-hole symmetry, which originates from the structure of the mean-field equation for superconductors, Bogoliubov-de Gennes equation. For the latter $\mathcal{P}^2 = 1$ always.

Nevertheless a unitary symmetry may change the symmetry class of the Hamiltonian as well as the absence of some terms in the Hamiltonian due to different requirements. Let us give two examples of the change of the symmetry class of the Hamiltonian.

i. If the Hamiltonian has some unitary symmetry as an addition to the anti-unitary described above. For example:

$$\sigma_y H \sigma_y = H, \tag{1.13}$$

then along with time-reversal symmetry $\mathcal{T}$ it has

$$\mathcal{T}' = -U_T \sigma_y K, \tag{1.14}$$

$$\mathcal{T}^2 = -\mathcal{T}'^2. \tag{1.15}$$

This does not mean that the system has two time-reversal symmetries, but it means that one needs to write the Hamiltonian in the basis, where the unitary symmetry is diagonal and then study the symmetry class of each block. As the blocks are completely decoupled only the symmetry class of a single block plays a role for the physical properties of the system. Let us study an example:

$$\mathcal{T} = \sigma_y K, \tag{1.16}$$

$$\mathcal{T}' = K. \tag{1.17}$$

Then when we diagonalize the Hamiltonian, the first symmetry becomes inter-block symmetry and the second stays in-block, and squares to $+1$, which means that by the unitary symmetry we have moved the system from one symmetry class to another.

ii. When some terms are absent from the Hamiltonian due to the configuration of the system, artificial additional symmetry may be produced. BDI superconducting nanowire [36], discussed also in the chapter 4, is an example of such a case. The usual 2d class D Hamiltonian of a spin-orbit coupled material with external magnetic field in y direction reads [21]:

$$H = \left(\frac{p^2}{2m} - \mu\right)\tau_z + v_{so}(p_x \sigma_y \tau_z - p_y \sigma_x) + E_Z \sigma_x \tau_z + \Delta \sigma_y \tau_y, \tag{1.18}$$

where v_{so} is the scale, associated with the spin-orbit energy, and E_Z is the Zeeman energy due to magnetic field. The only symmetry of

the Hamiltonian is $\mathcal{P} = \tau_x K$, it belongs to class D. Notice, that if the transverse direction of a nanowire made from such a material is small compared to the spin-orbit length, then:

$$H' = \left(\frac{p^2}{2m} - \mu\right)\tau_z + v_{so} p_x \sigma_y \tau_z + E_Z \sigma_x \tau_z + \Delta \sigma_y \tau_y, \tag{1.19}$$

which has an additional symmetry $\mathcal{T} = K$ and brings the system into BDI symmetry class.

1.4 Effective theories of topological phase transitions

We now proceed to the description of the generic topological phase transition. Once the system is in symmetry class AIII, D, DIII, BDI or CII in 1 dimension, it can be made topological. Which means, under some parameters it will have end states. The transition to such state is always accompanied with the bulk gap closing. Actually, the mechanism of forming edge states is the same: the transition is in real space, with edge being the region of the closed gap on the boundary.

Near the transition the system can always be described by the linear dispersion with a small gap opening on either sides of it. Exactly at the transition the Hamiltonian reads:

$$p\sigma \otimes \tau, \tag{1.20}$$

where the subscript and the structure of the σ and τ matrices is chosen based on the symmetry class.

For the purposes of this thesis we will concentrate on the 1d case and derive the effective theories near the topological transition for all the classes. The symmetries in the topological classes are [10]: AIII – $\mathcal{C}$; BDI – $\mathcal{P}^2 = 1$, $\mathcal{T}^2 = 1$; DIII – $\mathcal{P}^2 = 1$, $\mathcal{T}^2 = -1$; D – $\mathcal{P}^2 = 1$; and CII – $\mathcal{P}^2 = -1$, $\mathcal{T}^2 = -1$. Let us describe the minimal models, tuning through the topological transition for all the classes above.

The most simple one is for the class D (also discussed later on in the chapter 3) and may be written in the basis of the states, for which the topological gap closes, as:

$$H_{\mathrm{D}} = v_0 p \sigma_0 + v_z p \sigma_z + a \sigma_y. \tag{1.21}$$

Here $v_z \pm v_0$ are the velocities of right (left) movers and a is the parameter, tuning through the topological transition, $a = 0$ is the point of

the transition. The only symmetry the Hamiltonian has is the particle-hole symmetry $\mathcal{P} = K$. There always is a Majorana bound state on the boundary between $a > 0$ and $a < 0$ regions.

By analogy, in the symmetry class AIII:

$$H_{\text{AIII}} = \mu\sigma_z + v_z p\sigma_z + a\sigma_y, \tag{1.22}$$

and the only symmetry here is the chiral one $\mathcal{C} = \sigma_x$, as all the anti-unitary symmetries act differently on $\mu\sigma_z$ and $p\sigma_z$. Again a tunes through the transition. The most well-known example of a system from the symmetry class is polyacetylene, which is described exactly by the model above. There the excitations on the boundary of the two phases are fermions with the charge which is half of an electron charge. Note that the AIII case and the D one have very similar phenomenology, since they coincide for $v_z = \mu = 0$.

Now, BDI is the version of class D with time-reversal symmetry, which squares to $+1$. Minimal model for that is:

$$H_{\text{BDI}} = v_z p\sigma_z + a\sigma_y, \tag{1.23}$$

where the symmetries read: $\mathcal{P} = K$, $\mathcal{T} = \sigma_x K$. The BDI class has $\mathbb{Z}$ topological number, but the model above describe the system only near one of the possible series of topological transitions. The excitations of the phase boundaries are multiple Majorana bound states, decoupled due to the time-reversal symmetry. The way to obtain this class in the nanowire setup was described above and we will return to it in the section 4.

We proceed with DIII case, where the minimal Hamiltonian must be written in a 4×4 matrix form, as at the transition point there are 4 states with nearly zero energy (particle-hole partners along with Kramers ones). Then:

$$H_{\text{DIII}} = v_{0z} p\tau_z + a\tau_z\sigma_y + b\tau_y + c\tau_y\sigma_z, \tag{1.24}$$

and $\mathcal{T} = \tau_x\sigma_y K$ and $\mathcal{P} = K$. The minimal number of terms in the minimal Hamiltonian is 4 for 4×4 one with both $\mathcal{T}$ and $\mathcal{P}$ symmetries. This can be understood as following: we need that there is no possible unitary symmetry on top of the two. That means that any combination of Pauli matrices should not commute with the Hamiltonian. For that you need at least $2 \times 2 = 4$ matrices, as one needs two in both Pauli matrix spaces. It is easy to see that if we put $b = c = 0$, the phase

boundary is at $a = 0$. Indeed, then there are two decoupled blocks of class D, where the transition is at $a = 0$. Once we couple them with b and c, we cannot remove the degeneracy between the Majorana modes, as they are Kramers pair of each other.

The last remaining class is CII, where:

$$H_{\mathrm{CII}} = v_{yz} p \sigma_y \tau_z + a \tau_y + b \sigma_x \tau_x + c \tau_z, \tag{1.25}$$

and the symmetries are $\mathcal{P} = \tau_y K$, $\mathcal{T} = \tau_z \sigma_y K$, again for $b = c = 0$ phase boundary is $a = 0$, as then the model is two decoupled AIII systems at that point. These subsystems are eigenfunctions of σ_y with eigenvalues ± 1, and the chiral symmetry $\mathcal{C} = \tau_x \sigma_y$ acts within a block.

1.5 Scattering matrix description

The Hamiltonians above can easily be transformed into scattering matrices of finite systems, described by these Hamiltonians. For any 1d system we can write a transfer matrix, connecting the right and the left ends of it. As all the Hamiltonians above are of the form $H = Ap + B$, where A and B are some matrices, the transfer matrix at energy ϵ is:

$$A \frac{\partial \psi}{\partial x} = (iB - i\epsilon)\psi, \tag{1.26}$$

$$\psi(x) = \exp\left[A^{-1}(iB - i\epsilon)x\right] \psi(0). \tag{1.27}$$

Transfer matrix M of a system of length L then reads:

$$M = \exp\left[A^{-1}(iB - i\epsilon)L\right]. \tag{1.28}$$

This matrix can be transformed into scattering matrix either from one side of a closed system (for that one finds the boundary conditions on the far end of the system, see chapter 3 for an example), or constructs a scattering matrix of a system, open from both sides by choosing the propagation basis on both sides. For the first approach we write the boundary condition on the far end of the wire of a general kind:

$$(1 - Q)\psi_{\mathrm{right}} = 0, \tag{1.29}$$

where Q is the hermitian unitary matrix, which has only eigenvalues $+1$ and -1, but it also must have equal number of them, $+1$ for the

wavefunctions (eigenfunctions of the matrix), growing in the direction outside the wire, and -1 for all other. Then we write the transfer matrix in the basis of in- and outgoing waves:

$$M \begin{pmatrix} \psi_{\text{in}} \\ \psi_{\text{out}} \end{pmatrix} = \psi_{\text{right}}, \tag{1.30}$$

$$(1-Q)M \begin{pmatrix} 0 \\ \psi_{\text{out}} \end{pmatrix} = (1-Q)M \begin{pmatrix} \psi_{\text{in}} \\ 0 \end{pmatrix} \tag{1.31}$$

The symmetries of the scattering matrix can be deduced from the procedure above, but a more simple way is to look at an infinitely narrow piece of the material in question. Then the scattering matrix coincides with the time evolution matrix over the time the particle takes to scatter. There are now time shifts in such a setup. Then:

$$S(\epsilon) = e^{i\Delta t(H-\epsilon)}, \tag{1.32}$$

and the symmetries of H are directly transformed into the ones of the S. For example:

$$KHK = -H, \tag{1.33}$$

$$KS(\epsilon)K = e^{i\Delta t(H+\epsilon)} = S(-\epsilon). \tag{1.34}$$

This symmetries transform into the analytical properties of the S. For example for the matrix above:

$$KS(\epsilon + i\Gamma)K = S(-\epsilon + i\Gamma). \tag{1.35}$$

This will be used in the chapter 2, where we will study the analytical properties of the scattering matrices in more details.

1.6 This thesis

1.6.1 Chapter 2

Motivated by the recent developments in the field of one-dimensional topological superconductors, in this chapter we investigate the topological properties of the scattering matrix of generic superconducting junctions where dimension should not play any role. We argue that for any finite junction the scattering matrix is always topologically trivial.

The apparent contradiction with the previous results is resolved by taking into account the low-energy resonant poles of the scattering matrix. Thus, no common topological transition occurs in a finite junction. This is what one expects from the general theory of phase transitions, which predicts that they become crossovers in finite systems. A transition of a different kind is revealed. It concerns the configuration of the resonant poles of the scattering matrix of the system. We also introduce a sample setup, where the transition can be artificially induced. In later chapters we will return to this transition.

1.6.2 Chapter 3

This chapter builds on the the results of the previous one and addresses the correspondence between the common topological transition in infinite system and the topological transition of the other type that manifests itself in the positions of the poles of the scattering matrices. The setup studied is a nanowire coupled to a lead through a tunnel barrier. In the vicinity of the common transition we establish a universal dependence of the pole positions on the parameter controlling the transition. The manifestations of the pole transitions in the differential conductance are discussed.

1.6.3 Chapter 4

This chapter shows that weak antilocalization by disorder competes with resonant Andreev reflection from a Majorana zero-mode and produces a zero-voltage conductance peak of order e^2/h in a superconducting nanowire. The phase conjugation needed for quantum interference to survive a disorder average is provided by particle-hole symmetry - in the absence of time-reversal symmetry and without requiring a topologically nontrivial phase. We identify methods to distinguish the Majorana resonance from the weak antilocalization effect. The mechanism for the individual system to show a peak in zero-bias conductance is the pole transition studied in chapters 2 and 3. An example of the dependence of the conductance of a single normal metal-superconductor contact is shown in fig. 1.6.

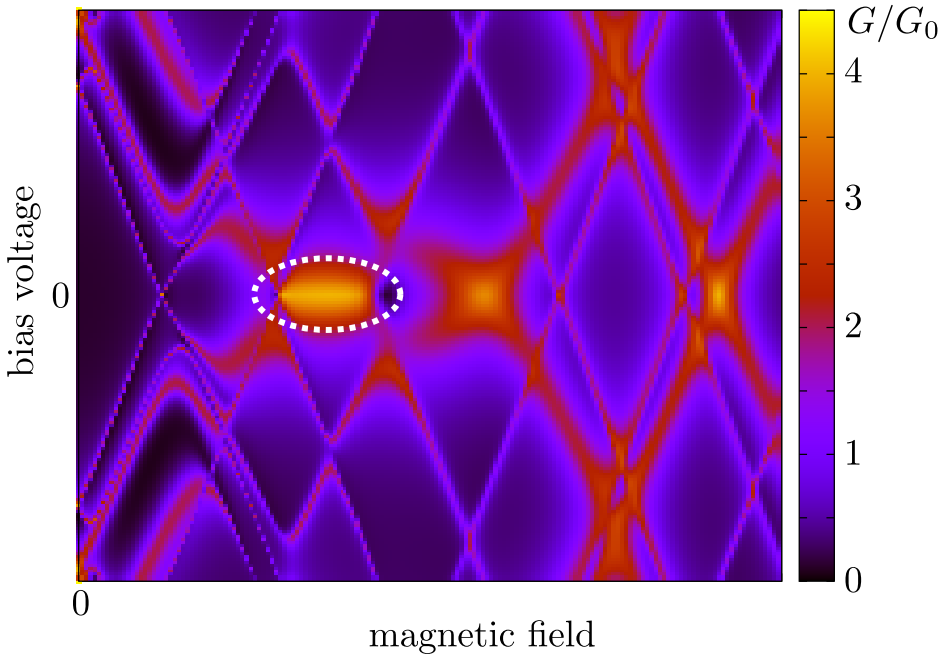

Figure 1.6. Example of a conductance dependence of magnetic field and bias voltage for a narrow nanowire. It shows that the zero-bias peak is developed in a region of magnetic fields, and the peak is not connected with the topology, but with the pole transition from chapters 2 and 3. Averaging over the systems gives the effect, discussed in the chapter 4, weak antilocalization.

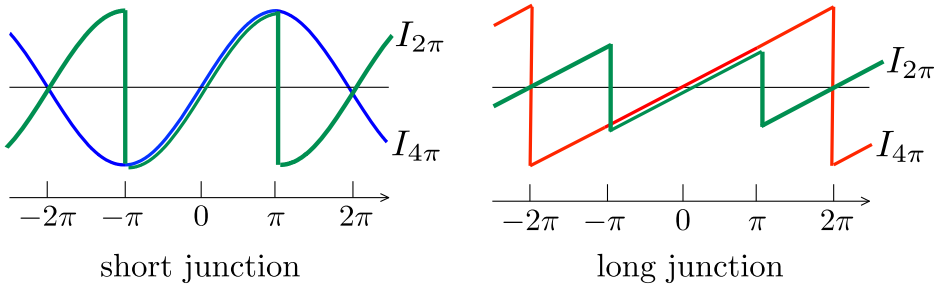

Figure 1.7. Sketch of the dependences of the 2π (parity non-conserving) and 4π (parity conserving) supercurrents for long and short Josephson junctions. The picture shows doubling of the supercurrent in the case of the long junction.

1.6.4 Chapter 5

In this chapter we study the other setup, already discussed in the chapter 2, Josephson junction made with a topological nanowire. We derive and discuss a generic phenomenological model that accounts for avoided crossing of Andreev states. This allows for a model-independent study. We investigate the dynamics of the junction at constant bias voltage to reveal an unexpected pattern of *any-*π Josephson effect in the limit of slow decoherence.

1.6.5 Chapter 6

This chapter investigates the Josephson current through the helical edge state of a quantum spin-Hall insulator. The separation L between the superconducting electrons and the coherence length ξ can have arbitrary relation with each other. We calculate the maximum (critical) current I_c that can flow without dissipation along a single edge, going beyond the short-junction restriction $L \ll \xi$ of earlier work, and find a dependence on the fermion parity of the ground state when L becomes larger than ξ. Fermion-parity conservation doubles the critical current in the low-temperature, long-junction limit, while for a short junction I_c is the same with or without parity constraints, see fig. 1.7. This provides a phase-insensitive, DC signature of the 4π-periodic Josephson effect.

1.6.6 Chapter 7

This chapter steps out of the main topic of the current thesis. Motivated by recent interest in the Nernst effect in cuprate superconductors, we calculate the magneto-thermo-electric effect for an arbitrary (anisotropic) quasiparticle dispersion relation and elastic scattering rate. The exact solution of the linearised Boltzmann equation is compared with the commonly used relaxation-time approximation. We find qualitative deficiencies of this approximation, to the extent that it can get the sign wrong of the Nernst coefficient. Ziman's improvement of the relaxation-time approximation, which becomes exact when the Fermi surface is isotropic, also cannot capture the combined effects of anisotropy in dispersion and scattering.

Bibliography

[1] K. von Klitzing, G. Dorda and M. Pepper, Phys. Rev. Lett. **45**, 494 (1980).

[2] C. L. Kane and E. J. Mele, Phys. Rev. Lett. **95**, 226801 (2005).

[3] B. A. Bernevig, T. L. Hughes, and S.-C. Zhang, Science, **314**, 1757 (2006).

[4] M. König, S. Wiedmann, C. Brüne, A. Roth, H. Buhmann, L. W. Molenkamp, X.-L. Qi, and S.-C. Zhang, Science **318**, 766 (2007).

[5] L. Fu, C. L. Kane and E. J. Mele, Phys. Rev. Lett. **98**, 106803 (2007).

[6] J. E. Moore and L. Balents, Phys. Rev. B **75**, 121306(R) (2007).

[7] D. Hsieh, D. Qian, L. Wray, Y. Xia, Y. S. Hor, R. J. Cava, and M. Z. Hasan, Nature **452**, 970 (2008).

[8] L. Fu and C. L. Kane, Phys. Rev. Lett. **100**, 096407 (2008).

[9] J. Nilsson, A. R. Akhmerov, and C. W. J. Beenakker, Phys. Rev. Lett. **101**, 120403 (2008).

[10] A. P. Schnyder, S. Ryu, A. Furusaki and A. W. W. Ludwig, Phys. Rev. B **78**, 195125 (2008).

[11] C. W. J. Beenakker, Annu. Rev. Con. Mat. Phys. **4**, 113 (2013).

[12] J. Alicea, Rep. Prog. Phys. **75**, 076501 (2012).

[13] G. Moore and N. Read, Nucl. Phys. B **360** 362 (1991).

[14] D. A. Ivanov, Phys. Rev. Lett. **86**, 268 (2001).

[15] A. Yu. Kitaev Phys. Usp. **44**, 131 (2001).

[16] A. Yu. Kitaev Ann. Phys. **303**, 2 (2013).

[17] J. Alicea, Y. Oreg, G. Refael, F. von Oppen, and M. P. A. Fisher, Nature Physics **7**, 412 (2011).

[18] T. Hyart, B. van Heck, I. C. Fulga, M. Burrello, A. R. Akhmerov, and C. W. J. Beenakker, Phys. Rev. B **88**, 035121 (2013).

[19] C. Nayak, S. H. Simon, A. Stern, M. Freedman, and S. Das Sarma, Rev. Mod. Phys. **80**, 1083 (2008).

[20] L. Fu and C. L. Kane, Phys. Rev. B **79**, 161408R (2009).

[21] R. M. Lutchyn, J. D. Sau, and S. Das Sarma, Phys. Rev. Lett. **105**, 077001 (2010).

[22] Y. Oreg, G. Refael, and F. von Oppen, Phys. Rev. Lett. **105**, 177002 (2010).

[23] V. Mourik, K. Zuo, S. M. Frolov, S. R. Plissard, E. P. A. M. Bakkers, and L. P. Kouwenhoven, Science **336**, 1003 (2012).

[24] M. T. Deng, C. L. Yu, G. Y. Huang, M. Larsson, P. Caroff, and H. Q. Xu, Nano Lett. **12**, 6414-6419 (2012).

[25] A. Das, Y. Ronen, Y. Most, Y. Oreg, M. Heiblum, and H. Shtrikman, Nature Physics **8**, 887 (2012).

[26] L. P. Rokhinson, X. Liu, and J. K. Furdyna, Nature Physics **8**, 795 (2012).

[27] A. F. Andreev, Sov. Phys. JETP **19**, 1228 (1964).

[28] Shuo Mi, D. I. Pikulin, M. Wimmer, and C. W. J. Beenakker, Phys. Rev. B **87**, 241405(R) (2013).

[29] K. T. Law, P. A. Lee, and T. K. Ng, Phys. Rev. Lett. **103**, 237001 (2009).

[30] C. W. J. Beenakker, Rev. Mod. Phys. **69**, 731 (1997).

[31] Y. V. Nazarov and Y. M. Blanter, *Quantum Transport*, (Cambridge University Press, Cambridge, 2009).

[32] B. D. Josephson, Rev. Mod. Phys. **36**, 216 (1964).

[33] P.-G. de Gennes, *Superconductivity of Metals and Alloys*, Addison-Wesley, Reading, MA (1986).

[34] L. Fu, Phys. Rev. Lett., **106**, 106802 (2011).

[35] I. C. Fulga, F. Hassler, and A. R. Akhmerov, Phys. Rev. B **85**, 165409 (2012).

[36] S. Tewari and J. D. Sau, Phys. Rev. Lett. **109**, 150408 (2012).

Chapter 2

Topological properties of superconducting junctions

2.1 Introduction

Superconducting junctions, including superconducting - normal (SN) ones where dissipative conduction can take place and superconducting - superconducting (SS) ones where a discrete spectrum of bound Andreev states is formed, have been in focus of condensed-matter research for almost fifty years [1, 2]. An indispensable compact approach to superconducting junctions employs a scattering matrix that relates incoming and outgoing wave amplitudes that obey the Bogolyubov-deGennes (BdG) equation [3, 4]. The beauty and power of this approach stems from its ability to incorporate numerous microscopic details in a compact form of the scattering amplitudes. Straightforward extensions permit to include magnetism, spin-orbit interaction, non-trivial superconducting pairing [5]. The s-matrix approach can be easily combined with semiclassical treatment of electron transport in the framework of a quantum circuit theory [2].

Recent developments in the field of superconductivity require revision of the common assumptions concerning the structure and properties of the scattering matrix of a superconducting junction. Kitaev in 2000 has suggested a model 1d p-wave superconductor [6] that exhibits a topological order. It has been shown recently that the same topological order can be realized in more realistic systems that combine spin magnetic field [7] with strong spin-orbit interaction [8, 9]. Similar situ-

ation would occur in a superconductor on the top of topological insulator or half-metal [10]. The relevance of these developments for generic superconducting junctions is not immediately obvious. Indeed, the general properties of those are not supposed to depend on dimension [11], while topological ordering considered is specific for one dimension [12] thus suggesting that the topological properties are not at all manifested in junctions. However, a number of spectacular predictions and device schemes that relate the topology and junction properties has appeared in the last years. Those include: prediction of so-called 4π periodic Josephson effect [8, 9, 13, 14], formulation of a criterion for topological transition in terms of reflection matrix of a junction [15], proposals of topological qubits based on majorana bound states [6, 14] as well as their readout with qubits of different type [16].

This motivated us to focus on a general BdG scattering matrix that bears no information on such details as dimensionality, absence/presence of disorder and concrete values of parameters responsible for the lifting of spin and time-reversal degeneracies. We have performed a topological analysis of such matrix concentrating on energy dependence of its eigenvalues. This rather elementary analysis shows that *i*. there are topologically non-trivial s-matrices (TNTM) characterized by real eigenvalues at zero energy, *ii*. there are topologically non-trivial trajectories (TNTT) in the space of topologically trivial s-matrices (TTM), that pass a matrix with real eigenvalues at $E = 0$ odd number of times.

TNTM would correspond to a "topological" SN junction [17], while TNTT would explain 4π-periodicity of Josephson effect in SS junctions [8, 9, 13]. However, if we proceed with the same topological agruments we are able to prove the topological triviality of all physical (i.e. describing finite junctions) s-matrices. *There are no TNTM neither TNTT.* This brings about a paradox that requires an explanation. We resolve it by recognizing a potentially sharp energy dependence of a s-matrix near zero energy. Such energy dependence is due to resonant poles [18] that manifest formation and coupling of zero-energy quasilocalized states. With this, we reconcile the predictions of [8, 9, 13], show the absence of a common topological transition and reveal topological transitions related to the resonant poles.

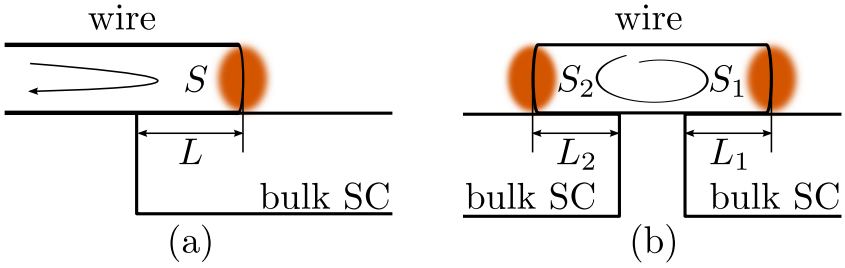

Figure 2.1. Setups to illustrate general topological properties of BdG s-matrices. a. Finite-length wire with strong spin-orbit coupling on the top of superconducting lead forming a SN junction. b. Finite-length wire between two superconductors forming SS junction. Orange ellipses indicate "buried" zero-energy states.

2.2 Setups

We illustrate these results with two minimal setups, SN and SS junctions (Fig. 2.1), where a single-channel wire with strong spin-orbit coupling and subject to magnetic field is brought in contact with a bulk superconductor. The Hamiltonian description of this situation is found in [8]. In distinction from [8], we assume finite length of the contact. The solutions of BdG equation for a single channel encompass spin and electron-hole degree of freedom so that the minimal single-channel scattering matrix is 4×4. The parameter space of the model that includes the superconducting gap, chemical potential, strength of spin-orbit interaction, and magnetic field, can be separated into two ranges: "topological" and non-"topological".

2.3 General topological properties

Let us consider a general s-matrix of a SN junction assuming no symmetries. The only constraint on such matrix stems from the structure of BdG equation: its Hamiltonian satisfies $\hat{H}^* = -\tau_1 \hat{H} \tau_1$, where the operator τ_1 switches electrons and holes. The constraint is convenient to represent in so-called Majorana basis [19] where the Hamiltonian is antisymmetric and the scattering matrix satisfies $S(E) = S^*(-E)$, E being energy counted from the chemical potential of the superconductor. We will consider only energies E within the energy gap of the bulk su-

perconductor. In this case, there are no scattering waves in the bulk of superconductor, the matrix $\hat{S}$ is in the basis of normal-metal scattering waves satisfying unitary condition.

Let us concentrate on (continuous) energy dependence of the matrix eigenvalues $e^{i\chi(E)}$. That can be represented as a manifold of curves in $\chi - E$ plane (Fig. 2.2). The BdG constraint implies that if a point (χ, E) belongs to the manifold, the inverted point $(-\chi, -E)$ belongs to it as well. These two points can belong to either the same curve or to two distinct curves. In the first case, the curve is topologically distinct: it is forced to pass either $\chi = 0$ or $\chi = \pm\pi$ at zero energy. If two such curves pass the same point, they can be deformed by continuous change of Hamiltonian parameters into a pair of trivial curves. However, a single curve is topologically stable: the fact it passes the point cannot be changed by Hamiltonian variations. We note that the dimension of the physical s-matrices can be always chosen even. With all this, all s-matrices can be separated onto two classes. Topologically trivial matrices (TTM) have no topologically distinct curves while topologically non-trivial (TNTM) have two topologically distinct curves passing respectively $\chi = 0$ and $\chi = \pm\pi$ at $E = 0$. Indeed, at zero energy s-matrices are real forming O(2N) group. TTM belong to SO(2N) subgroup of O(2N), while TNTM belong to O(2N)/SO(2N). The matrices from these distinct submanifolds cannot be continuously deformed into one another: indeed, at $E = 0$ $\det(TTM) = 1$ while $\det(TNTM) = -1$.

This classifies s-matrices of SN junction. An SS junction is characterized by a combination of two s-matrices (Fig. 2.3). The spectrum of Andreev states of the junction as function of superconducting phase difference ϕ is obtained from the equation [4]

$$0 = \det\left(\hat{1} - \hat{S}\right);\ \hat{S} = \hat{s}_1 e^{i\phi\tau_3/2}\hat{s}_2 e^{-i\phi\tau_3/2}, \tag{2.1}$$

τ_3 being Nambu matrix distinguishing electrons and holes. It is instructive to note that the unitary matrix $\hat{S}(\phi)$ satisfies the same BdG constraint as an SN s-matrix. Therefore, the above topological classification applies to SS junctions as well.

In this respect it is crucial to note another topological property that concerns continuous one-parameter closed manifolds of TTM (trajectories). Intuitively, eigenvalues of a generic matrix "repel" each other and never come together. This applies to BdG matrices expect a special situation: $E = 0$ and real eigenvalues. Owing to this peculiarity, a trajectory

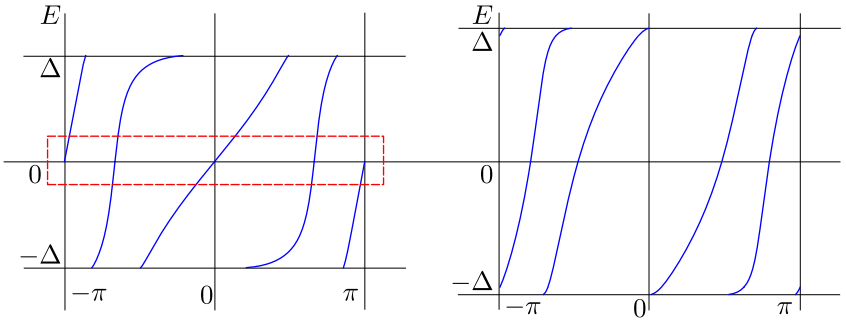

(a): non-trivial (b): trivial

Figure 2.2. Energy dependence of s-matrix eigenvalues. (a) Topologically non-trivial (TNTM) case, corresponding to the "topological" parameter range in [8]. (b) Generic topologically trivial (TTM) case. (Numerical results for the setup in Fig. 1a in the limit $L \to \infty$.)

in matrix space can in principle pass a matrix where two eigenvalues, say, $+1$, are the same. It turns out that the trajectories of the kind can be separated onto two topological classes that differ by parity of the number of passes. (Fig. 2.4) To see the possibility for odd number of passes, let us take a closed trajectory with a single pass and concentrate on two eigenvectors corresponding to the eigenvalue $+1$. In this situation, if the parameter cycles over the trajectory, a given eigenvector is transformed not to itself but rather to its orthogonal counterpart, this guarantees the stability of this topologically non-trivial trajectory (TNTT).

Let us understand the results of [8, 14, 13] in terms of the above classification. Without going into details, we enunciate that TNTM are realized in the "topological" parameter range. The TNTT give the topological explanation of the 4π Josephson effect described in these articles. The trajectory parameter in this case is the superconducting phase difference ϕ.

2.4 Paradox

However, similar topological considerations show that *no* physical s-matrix belongs to TNTM class, *neither* any closed trajectory in parameter space is a TNTT. "Physical" in this case means a finite junction between infinite leads where the "topological" [8, 9, 13] transition is necessary

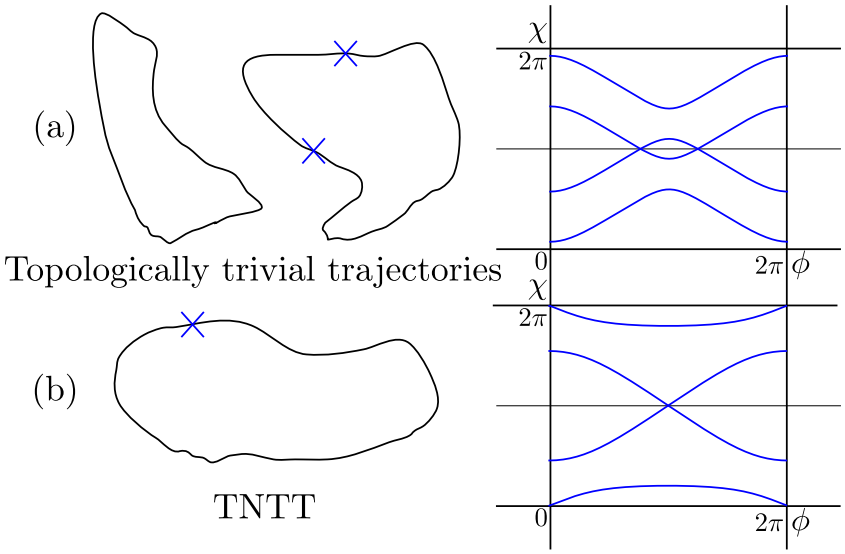

Figure 2.3. Topological classes of trajectories in the space of TTM. A trajectory is topologically non-trivial (TNTT) provided it passes the matrix with two degenerate real eigenvalues *odd* number of times. Illustration: the dependencies of eigenvalues of the scattering matrix characterizing the SS junction on superconducting phase difference ϕ for (a) non-"topological" and (b) "topological" parameter ranges.

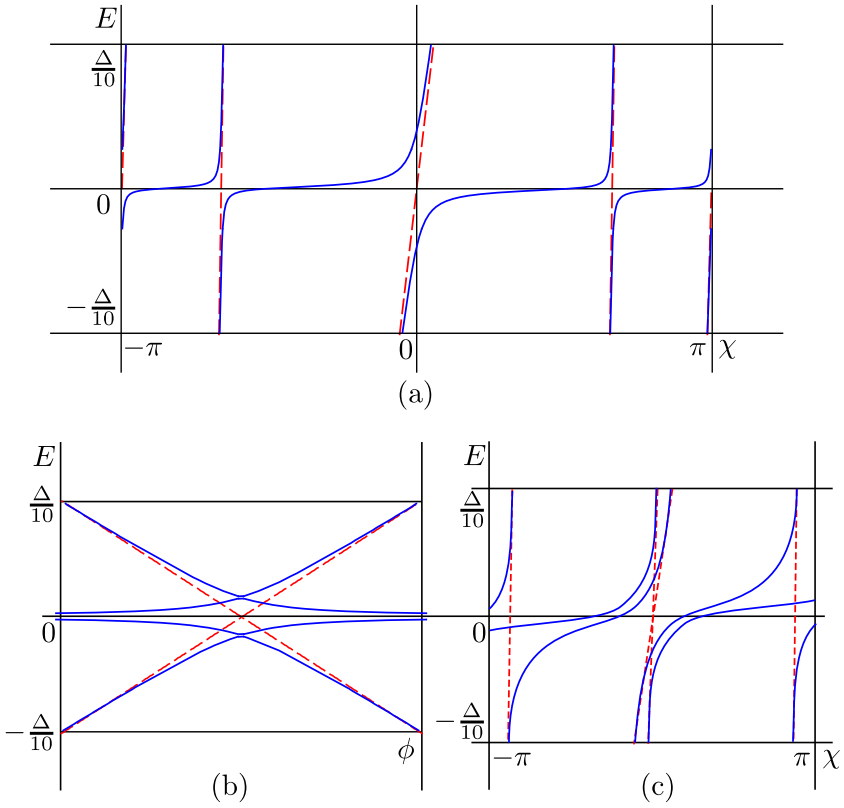

Figure 2.4. (a): Energy dependence of eigenvalues for NS junction in a narrow energy interval illustrates the topological triviality of s-matrix for finite length of the contact (L=7 in units of [8]). Dashed lines: "high"-energy TNTM eigenvalues. We see the reconnection of neighboring eigenvalues. (b): Andreev levels in SS junction versus superconducting phase difference at $L_1 = L_2 = 7$ (solid lines) as compared to TNTT case at $L_{1,2} = \infty$ (dashed lines). (c) Energy dependence of eigenvalues for case (b) and $\phi = \pi$. Dashed lines: TNTT case.

smoothed. To prove, let us start with a common junction manifesting no exotic properties. For our examples, this may correspond to a junction in zero magnetic field and zero spin-orbit interaction. The s-matrix at this parameter choice as well as all trajectories are topologically trivial. Since there is no continuous way to tune scattering matrix from TTM to TNTM class, and the transition is smoothed, the s-matrix will stay trivial at any strength of magnetic field/spin-orbit interaction, even after the "topological" transition. This proof is in a seeming contradiction with the predictions mentioned [8, 9, 13]. This "*paradox*" motivated us for the deeper research.

Prior to presenting the solution of the paradox, let us mention that the absence of TNTT resolves an annoying problem that concerns the parity of particle number of the ground state of the SS junction. The level crossings at $E = 0$ are known in the context of ferromagnetic SS junctions. Upon passing the crossing, it becomes energetically favourable to put a single polarized quasiparticle to the junction [20]. Therefore, the parity of the ground state must be different at two sides of the crossing. In this work, we concentrate on the properties of the ground state. However, the odd number of crossings at a closed curve suggest that the parity of this ground state cannot be unamgiguously defined: a situation that is annoyingly difficult to comprehend.

2.5 Resolution of the paradox. Poles of a scattering matrix

To see how the paradox is resolved, let us consider numerical results for a finite SN junction in "topological" parameter range.(Fig. 4a) If the results are plotted at energy scale of the superconducting gap, the pattern of energy dependent eigenvalues is apparently of TNTM type as in Fig. 2a. However, replotting the results near $E = 0$ at smaller scale reveals topological triviality (cf. Fig. 4a and Fig. 2b). The eigenvalues move fast in the vicinity of $E = 0$ reconnecting the branches visible at larger energy scale in a rather unexpected way. The typical energy scale of such reconnection is small depending exponentially on the contact length L, and shrinks to zero at $L \to \infty$. Therefore, the ground state is always of even parity and its energy is 2π periodic. The 4π periodicity may only be observed if the phase is swept fast enough to get the setup to an excited state (of the same parity).

The adequate description of the situation combines a smooth energy dependence of s-matrix at $E \simeq \Delta$ with a pole or poles that are anomalously close to $E = 0$. Let us consider a single pole. The BdG constraints restrict it to purely imaginary energy, $-i\Gamma \ll \Delta$. The s-matrix reads

$$\hat{s} = \left(\hat{1} - \left(\frac{\epsilon - i\Gamma}{\epsilon + i\Gamma} - 1 \right) |\Psi><\Psi| \right) \hat{S}_0, \tag{2.2}$$

where Ψ is the eigenvector associated with the resonant level and $\hat{S}_0$ is the matrix, with smooth energy dependence to disregard at $E \simeq \Gamma$. The eigenvalues in this energy range are determined from equation $\epsilon/\Gamma = \sum_k |\Psi_k|^2 \cot(\chi_k - \chi_k^{(0)})$, $\exp(i\chi_k^{(0)})$ being "high-energy" ($|E| \gg \Gamma$) eigenvalues of S_0 . They follow the pattern in Fig. 2.4 connecting neighboring "high-energy" eigenvalues, $\exp(i\chi_k^{(0)}) \to \exp(i\chi_{k+1}^{(0)})$. This guarantees that the total shift of phases of all eigenvalues upon crossing a single pole equals 2π. Physically, the pole is associated with a quasi-localized zero-energy state being formed at the far end of the wire. If the contact length exceeds the localization length, this state is efficiently "buried" ($\Gamma \ll \Delta$) in the superconductor and hardly accessible for incoming electron or hole waves except $E = 0$ when the scattering of the waves become resonant. Andreev conductance of the junction is expressed as $G_A = G_Q \mathrm{Tr}\left(\tau_3 \hat{s} \tau_3 \hat{s}^\dagger\right)$. In the resonant energy interval, the energy dependence of the conductance assumes a universal form $G_A(E) = G_A + \frac{\Gamma^2}{E^2+\Gamma^2}(G_A(0) - G_A)$, $G_A(0), G_A$ being its values at $E = 0, |E| \gg \Gamma$ that depend on details of the junction.

Let us turn to the SS junction in the "topological" parameter range. Solving Eq. 2.1 gives the spectrum of Andreev states (Fig. 2.5b). We observe the level crossing at $E = 0, \phi = \pi$ being lifted in a narrow energy interval. Strikingly, we observe another pair of levels with energies remaining small in the whole range of phase. These levels are absent in TNTT picture and emerge as a consequence of topological triviality of the s-matrix. Since there is no level crossing at $E = 0$, the parity of the ground state is always even.

The situation can be comprehended if we notice that each matrix $\hat{s}_1, \hat{s}_2$ forming the resulting $\hat{s}$ brings a resonant pole corresponding to a "buried" zero-energy state at far end of each wire. The $\hat{s}$ thus has two resonant poles. The mixing of the two "buried" states results in their (phase-dependent) energy splitting and formation of the pair of low-energy Andreev levels. The eigenvalues of s-matrix move in the

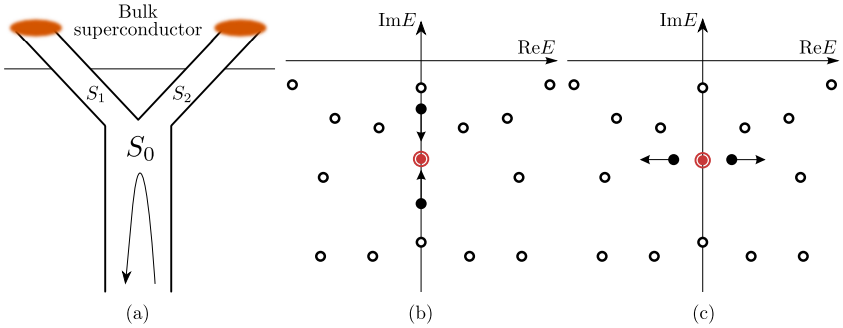

Figure 2.5. (a): Fork SN junction to illustrate topological transitions concerning the resonant poles. (b,c): Configurations of the resonant poles in the complex energy plane (b) before and (c) after a transition. At the transition point, the poles are degenerate (double red circle)

narrow energy interval reconnecting next-to-nearest (two poles) neighbour "high-energy" eigenvalues (Fig.2.3b). This brings four rather than two states in the vicinity of the crossing point $E = 0, \phi = \pi, \chi = 0$, all being involved in the lifting of the degeneracy. The detailed theory of the crossing point will be presented elsewhere.

2.6 Topological transition in the properties of the scattering matrix

Since the s-matrix remains topologically trivial, there seem to be no sharp transition in its characteristics that would correspond to the "topological" transition in the (rather unphysical) limit of infinite wire. However, a BdG s-matrix with resonant poles is characterized by a topological number that can change sharply upon changing the parameters. This, not directly connected to the limit of the infinite wire, transition happens near the point of "topological" transition in the finite wire.

Let us illustrate this with a two-pole scattering matrix correspond to the fork setup in Fig. 5 a. Here the scattering matrices S_1, S_2 of fork tines bring a resonant pole each. The BdG symmetry leaves two distinct possibilities for the poles of the total scattering matrix :*i*. both poles lie on the imaginary energy axis ($E = -i\Gamma_1, -i\Gamma_2$), *ii*. they form a pair symmetric with respect to reflection Re$E \to -$ReE ($E = \pm\varepsilon - i\Gamma$). One can now change the s-matrix $\check{S}_0$ describing the normal scattering in

the fork. If the tines are open to the lead states, the pole configuration should be like one for two parallel SN junctions: the possibility *ii* is realized. If the tines are isolated, the "buried" states mix resulting in an energy spitting: the possibility *i* is realized. We thus expect the transition at intermediate coupling.

Generally, one can characterize a BdG s-matrix of arbitrary dimension with a topological number that is just the number of poles lying precisely on the imaginary axis. We expect this number to change by 2 upon changing the parameters, this gives a series of "topological" transitions. (Fig. 5 b,c) Two poles are degenerate at the transition point. However, since in general the degenerate poles are at finite imaginary energy Γ, the manifestations of the transitions in transport properties are limited. The energy-dependent Andreev conductance does not seem to have a singularity at the transition point.

2.7 Conclusion

We have performed the topological analysis of the properties of SN and SS junctions characterized by BdG s-matrices. We have proven topological triviality of physical matrices that describe finite-size junctions: there is neither TNTM, nor TNTT. This implies the absence of a sharp "topological" transition upon crossing to "topological" parameter range as well as the absence of 4π-periodic Josephson effect. We have resolved the apparent contradiction with results of [8, 9, 14, 13] by considering the low-energy poles of s-matrices. The resulting sharp energy dependence at $E \approx 0$ leads to Lorentian energy dependence of Andreev conductance. We have demonstrated a topological transition (or a series of transitions) of a different kind associated with a change of the configuration of the resonant poles in complex energy plane.

Bibliography

[1] B. D. Josephson, Rev. Mod. Phys. **36**, 216 (1964); A. F. Andreev, Zh. Teor. Eksp. Fiz. **46**, 1823 (1964) [Sov. Phys. JETP **19**, 1228 (1964)].

[2] Y. V. Nazarov and Y. M. Blanter, *Quantum Transport*, (Cambridge University Press, Cambridge, 2009).

[3] A. L. Shelankov, Zh. Eksp. Teor. Fiz., Pis'ma. **32**, 2, 122-125 (1980); G. E. Blonder, M. Tinkham, and T. M. Klapwijk, Phys. Rev. B **25**, 4515 (1982).

[4] C. W. J. Beenakker, Phys. Rev. Lett. **67**, 3836 (1991).

[5] M. J. M. de Jong and C. W. J. Beenakker, Phys. Rev. Lett. **74**, 1657 (1995); N. M. Chtchelkatchev, W. Belzig, Yu. V. Nazarov, and C. Bruder, 2001, Pis'ma Zh. Eksp. Teor. Fiz. **74**, 357–361 (2001) [JETP Lett. **74**, 323–327 (2001)]; O. V. Dimitrova and M. V. Feigel'man, J. Exp. Theor. Phys. **102**, 652 (2006); C. Bruder, Phys. Rev. B **41**, 4017 (1990); Y. Tanaka and S. Kashiwaya, Phys. Rev. Lett. **74**, 3451 (1995).

[6] A. Y. Kitaev, Phys.-Usp. **44**, 131–136 (2001).

[7] J. D. Sau, R. M. Lutchyn, S. Tewari, and S. Das Sarma, Phys. Rev. Lett. **104**, 040502 (2010).

[8] R. M. Lutchyn, J. D. Sau, S. Das Sarma, Phys. Rev. Lett. **105**, 077001 (2010).

[9] Y. Oreg, G. Refael, and F. von Oppen, Phys. Rev. Lett. **105**, 177002 (2010).

[10] L. Fu and C.L. Kane, Phys. Rev. Lett. **100**, 096407 (2008); M. Duckheim and P. W. Brouwer, Phys. Rev. B **83**, 054513 (2011); S. B. Chung,

H.-J. Zhang, X.-L. Qi, and S.-C. Zhang, Phys. Rev. B **84**, 060510 (2011).

[11] C. W. J. Beenakker, Rev. Mod. Phys. **69**, 731 (1997).

[12] S. Ryu, A. Schnyder, A. Furusaki, and A. Ludwig, New J. Phys. **12**, 065010 (2010).

[13] L. Fu and C. L. Kane, Phys. Rev. B **79**, 161408(R) (2009).

[14] J. Alicea, Y. Oreg, G. Refael, F. von Oppen and M. P. A. Fisher, Nature Physics **7**, 412 (2011).

[15] F. Merz and J. T. Chalker, Phys. Rev. B **65**, 054425 (2002); A. R. Akhmerov, J. P. Dahlhaus, F. Hassler, M. Wimmer, and C. W. J. Beenakker, Phys. Rev. Lett. **106**, 057001 (2011)

[16] F. Hassler, A. R. Akhmerov, C.-Y. Hou, and C. W. J. Beenakker, New J. Phys. **12**, 125002 (2010).

[17] C. W. J. Beenakker, J. P. Dahlhaus, M. Wimmer, and A. R. Akhmerov, Phys. Rev. B **83**, 085413 (2011).

[18] E. Wigner, Phys. Rev. **70**, 15 (1946).

[19] E. Majorana, Nuovo Cimento **14**, 170 (1937).

[20] S.V.Kuplevakhskii and I. I. Falko, Pis'ma Zh. Eksp. Teor. Fiz. **52**, 957 (1990) [JETP Lett. **52**, 340 (1990)].

Chapter 3

Two types of topological transitions in finite Majorana wires

3.1 Introduction

Majorana bound states have been predicted to exist in various condensed matter setups: $5/2$ FQHE state [1], in vortices found in $p + ip$ superconductors [2] and in specific models of 1d superconductors[3]. The importance of the Majorana states for quantum computation [4] has brought them to the focus of the condensed matter research [5]. Next step were the suggestions to realize the Majorana states in more experimentally feasible setups, those include topological insulators [6, 7] and semiconductor nanostructures with big spin-orbit interaction brought in proximity to s-wave superconductors. Two- [8, 9] and one-dimensional [10, 11] nanostructures have been considered.

The observation of Majorana bound states in 1d nanowires has been reported by several groups by measuring zero-bias conductance peak [12–14] and 4π Josephson effect [15]. The signature of Majorana's is their emergence upon a topological transition [16] separating the regions of parameter space with and without zero-energy excitations. In all cases the experiments have been performed with finite and rather short wires. This brings about the question: how a topological transition taking place in infinite system is manifested in properties of a finite wire.

Strictly speaking, this common topological transition is absent in a

finite system where excitation energies continuously depend on the control parameter of the transition and are never precisely zero [17, 3, 10]. This may be shown in several ways. In [17] we gave the most general formulation in terms of the topology of the energy-dependent scattering matrix characterising a finite nanostructure. Same study revealed a topological transition of other kind that takes place in finite systems and manifests itself in the properties of the poles of the scattering matrix. The topological number in this case is the number of poles at purely imaginary energy, and the topological transition is the change of this integer even number upon the continuous variation of the control parameter. This is in contrast to a common expectation from a phase transition: if it becomes a crossover, no sudden changes of any quantity would occur.

In the present work we link these two topological transitions of different types: bulk one and finite system one. We show in this Article that in general case the common topological transition is accompanied by the pole topological transition (the opposite is not true, there can be a pole topological transition in topologically trivial situation [18]). The points of the transitions differ at the scale inversely proportional to the wire length. We implement the generic model of the Majorana wire that is always valid in the vicinity of the transition point and obtain the universal dependence of the pole positions on the control parameter and a single parameter characterizing the coupling of the wire to a normal metal lead. We discuss how the same correspondence occurs for more specific models and how the universal picture is manifested in a transport measurement.

3.2 Generic 2×2 model

The "standard" model describing a Majorana wire encompasses a single-band spectrum that includes spin-orbit interaction, proximity effect from the bulk superconductor and spin magnetic field [10, 11]. Let us derive a phenomenological effective model valid near the common topological transition point. We can start with a multi-mode wire where the spectrum at each k is described by a general Hamiltonian matrix $\hat{H}(k)$ in the space of the modes and Nambu index. The general symmetry of BdG equations [19] requires $\hat{H}(k) = -\hat{H}^T(-k)$ in a certain (Majorana) basis. In the usual basis the BdG symmetry reads $\hat{H}(k) = -\tau_x \hat{H}^T(-k)\tau_x$,

where τ_x is the Pauli matrix in the Nambu space, which connects particles with holes. Then by rotation of the Hamiltonian $\hat{H}'(k) = U^\dagger \hat{H}(k) U$, where $U = \frac{1}{\sqrt{2}}(1 + i\tau_x)$ we bring it to the Majorana basis. The common topological transition takes place when an eigenvalue of $\hat{H}(k = 0)$ passes 0 indicating a closing of the superconducting proximity gap in the wire.

Owing to BdG symmetry, the zero eigenvalue is doubly degenerate. Thus we concentrate on two modes corresponding the eigenvalue, and mutually related by the complex conjugation: in this basis, the BdG symmetry is expressed in the above form. Near the transition point the general form for this Hamiltonian in Majorana basis reads $H(k = 0) = a\sigma_y$, where σ's here and below are usual Pauli matrices. The phenomenological parameter a controls the proximity to the transition and is a function of physical control parameters like magnetic field or chemical potential, $a = 0$ in the transition point. Expanding near $k = 0$ and taking into account the BdG symmetry, we find two possible terms $\propto k\sigma_x$ and $\propto k\sigma_z$. The combination of the two can be brought to $\propto k\sigma_z$ by a rotation of the pseudospin about y axis. This brings us to the generic Hamiltonian we will use in further consideration:

$$H = vk\sigma_z + a\sigma_y. \tag{3.1}$$

It has been first introduced in [20].

Let us turn to a finite wire, setup on Fig. 3.1a. The boundary conditions at the wire ends must be consistent with the current conservation. The operator of current reads $\hat{I} = \frac{\partial H}{\partial k} = v\sigma_z$ so the conservation implies that the wavefunction $\Psi = \{\psi_1, \psi_2\}^T$ has to satisfy:

$$|\psi_1|^2 = |\psi_2|^2, \tag{3.2}$$

At zero energy the wavefunction is real [21], and we are left with binary choice $\psi_1 = \pm\psi_2$. We fix the signs to $+$ at the right end of a system and $-$ at the left one. In this case, in the limit of infinite wire length the Majorana states are formed at $a < 0$ while the phase at $a > 0$ is topologically trivial (Fig. 3.1b).

Let us now contact the left end of the wire with a normal metal lead and describe the situation in therms of the scattering matrix from/to normal lead modes. Scattering matrices are very useful objects to study the properties of the superconducting junctions [22]. They incorporate

relevant details of the setup in few parameters and allow to compute different properties of the junction, like conductivity. They also allow for the topological classification of the junction in a concise way [17]. The BdG symmetry equation in the Majorana basis implies for any scattering matrix that $S^*(-E) = S(E)$.

3.3 Scattering matrix

There are two interesting modes in the wire propagating in opposite directions. The scattering matrix of the contact S_c is in the basis of the incoming waves in the lead and the single mode of the wire and is thus of size $M+1 \times M+1$, M is the number of modes in the normal lead. We separate it into blocks as:

$$S_c = \begin{pmatrix} \check{r}_{11} & \check{r}_{21} \\ \check{r}_{12} & r \end{pmatrix}. \tag{3.3}$$

Here $\check{r}_{11}$ is $M \times M$ matrix of the (Andreev) reflection to the leads that also incorporates the scattering in all other wire modes, $\check{r}_{21,12}$ are scattering amplitudes from/to the wire and r is a number, which gives the reflection amplitude in the wire ($r = 1$ corresponding to the wire isolation) [23]. By virtue of BdG condition S_c is real at zero energy. Since the interesting energy dependence comes from the wire, we can neglect the energy dependence of S_c.

To get the full $M \times M$ scattering matrix in the space of normal lead modes, we need to combine the S_c with the scattering amplitude S_w that describes the propagation along the wire, reflection from the right and the propagation back to the left end. This amplitude is easy to find from the Hamiltonian (1) and reads

$$S_w = e^{i\chi} = \frac{\left(\coth(\sqrt{a^2-\epsilon^2}L/v) + \frac{a+i\epsilon}{\sqrt{a^2-\epsilon^2}}\right)}{\left(\coth(\sqrt{a^2-\epsilon^2}L/v) + \frac{a-i\epsilon}{\sqrt{a^2-\epsilon^2}}\right)}. \tag{3.4}$$

L being the wire length. The whole peculiarity of the limit of the infinite wire may be seen from this formula. If we formally set $L \to \infty$ and then set energy to zero, we obtain $S_w(\epsilon = 0) = \mathrm{sign}(a)$, which is thus topologically trivial (nontrivial) for $a < 0$ ($a > 0$). However, at any finite L $S_w(\epsilon = 0) = 1$ and is thus topologically trivial.

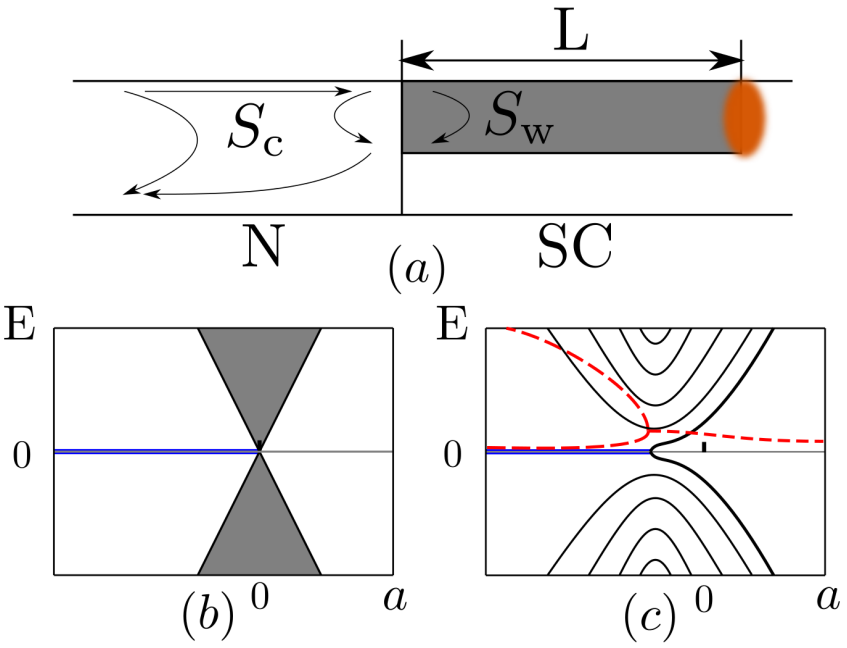

Figure 3.1. (a) The setup: the Majorana wire of the length L at the top of a superconductor is connected to a normal-metal lead. The total scattering matrix at low energy incorporates that of the contact (S_c) and energy-dependent scattering matrix describing propagation in the wire, S_w. Orange ellipse shows the position of the "buried" Majorana (b) Sketch of the (continuous) spectrum in the limit of infinite L: a Majorana level emerges upon the *common* topological transition. (c) The common topological transition becomes a crossover for finite L. The quantized energy levels (real parts of the pole energy positions) are sketched versus the control parameter a. The lowest level reaches 0 at the point of the *pole* topological transition. Dashed lines give the imaginary parts of the pole positions for the lowest level.

The full scattering matrix thus reads

$$S = \check{r}_{11} + \check{r}_{21} e^{i\chi} \frac{}{1 - re^{i\chi}} \check{r}_{12}. \tag{3.5}$$

3.4 Poles of the matrix and the topological transitions

We concentrate on *poles* of the matrix (3.5). Those are solutions of

$$\sqrt{a^2 - \epsilon^2} \coth(\sqrt{a^2 - \epsilon^2} L/v) + a - i\epsilon \frac{1-r}{1+r} = 0. \tag{3.6}$$

At finite length L the common topological transition becomes a crossover taking place in an interval of a of the order of effective level spacing in the wire v/L and at the corresponding energy scale. We call this interval crossover region and aim to describe this universal crossover. To this end we rescale a, ϵ to dimensionless units $\tilde{a} = a\frac{v}{L}$, $\tilde{\epsilon} = \epsilon \frac{v}{L}$. The equation becomes

$$\sqrt{\tilde{a}^2 - \tilde{\epsilon}^2} \coth(\sqrt{\tilde{a}^2 - \tilde{\epsilon}^2}) + \tilde{a} - i\tilde{\epsilon} \frac{1-r}{1+r} = 0. \tag{3.7}$$

Numerical solutions for pole positions are shown in Fig. 3.2a,b for two values of r as functions of the control parameter $\tilde{a}$. We see a sharp feature in the crossover region: the pole topological transition. At this point, the real part of the energy of the lowest pole becomes strictly zero. This occurs at finite negative values of $\tilde{a}$. The higher the transmission through the S_c, the closer to 0 is the transition point. This dependence is presented in Fig.3.2c. In the limit of low transmissions, the pole transition takes place at $|\tilde{a}| \simeq \ln(1-r)$ where the exponentially small splitting of Majorana states matches small decay rate of the left-end state to the normal metal. The real parts of energies of all other poles follow the hyperbola-like curves indicating formation of discrete energy levels in the wire above the gap edge $|\tilde{a}|$. The same transition is seen in imaginary parts of energy positions as a splitting of the curve corresponding to the lowest pole. The upper (lower) parts of the split curve give the decay rates of the left(right) end Majorana state. The decay rate for the Majorana "buried" at the right end falls off exponentially with increasing $|\tilde{a}|$: $\tilde{\epsilon} \approx 2i\tilde{a} \exp(-2|\tilde{a}|)\frac{1+r}{1-r}$.

Let us reveal the peculiarity of the pole positions in the vicinity of the transition point. For this, we expand (3.7) near the transition point

$\tilde{a} = a_0$, $\tilde{\epsilon} = i\epsilon_0$ to obtain the relation between the deviations $\delta\epsilon$,δa from the point in the lowest non-vanishing order:

$$\delta a = C\delta\epsilon^2;\ C \simeq 1. \tag{3.8}$$

Here $\mu = \frac{1-r}{1+r}$. This gives square root splitting of either real parts of the energy positions $\delta\epsilon = \pm\sqrt{\delta a/C}$ at $\delta a > 0$ or imaginary ones, $\delta\epsilon = \pm i\sqrt{|\delta a|/C}$ at $\delta a < 0$. This square root dependence of $\delta\epsilon$ on δa is in full agreement with Fig. 3.2a,b.

3.5 Conductance signatures of the transition

The experimentally observable quantity is the differential conductance of the contact, $G(\epsilon = eV)$, V being the voltage drop at the contact. It is known that each pole in the scattering matrix produces a Lorentian-shaped peak or deep in the conductance curve [17]. In terms of the scattering matrix, the conductance reads $G = \frac{e^2}{2\pi\hbar}\mathrm{Tr}(1 - \tau_y S\tau_y S^\dagger)$. Substituting S in the form of (3.5), we obtain a universal energy dependence of the conductance in the crossover region,

$$G(\epsilon) = G_0 + G_1 f(a,\epsilon); \tag{3.9}$$

$$f(a,\epsilon) = \frac{(1-r^2)^2}{1 + r^2 + 2r\cos\chi(a,\epsilon)}. \tag{3.10}$$

The dependence is governed by the universal function $f(a,\epsilon)$ ($0 < f < 4$) while the non-universal coefficients G_0, G_1 depend on the details of the S_c,

$$G_0 = \frac{e^2}{2\pi\hbar}\mathrm{Tr}\left(1 - (\check{r}_{11} - r^{-1}\check{r}_{21}\check{r}_{12})\tau_y\check{r}_{11}^T\tau_y\right),$$
$$G_1 = \frac{e^2}{2\pi\hbar}\frac{\mathrm{Tr}\left(\tau_y\check{r}_{21}\check{r}_{12}\tau_y(\check{r}_{12}^T\check{r}_{12}^T + (r - r^{-1})\check{r}_{11}^T)\right)}{(1-r^2)^2}. \tag{3.11}$$

The coefficient $G_1 \simeq e^2/\hbar$ and can be of *any* sign while G_0 can be much bigger than $e^2/\hbar$. The function f (Fig. 3.3) at any r gives a sequence of peaks associated with the poles of the scattering matrix. The peaks are narrow in the isolation limit $r \to 1$. Before the transition, the peaks are far from zero energy. Upon the crossover, the peaks come close to zero and almost merge near the transition point. However, they never

merge to a single peak: the Majorana state at far end of the wire is manifested in the conductance as a dip that becomes increasingly narrow upon increasing $-\tilde{a}$.

Since the poles always have a finite imaginary part, and the conductance is defined at real energy, there is no singularity in $f(\epsilon)$ at the point of the pole topological transition. However, this singularity can be readily identified from the experimental data by numerical analytical continuation to complex energy plane. This amounts to fitting the conductance trace by a superposition of Lorentian peaks. The positions of the fitted Lorentians will give the real parts of the pole positions while their widths give the imaginary parts.

3.6 Discussion

Another setup proposed [20] to reveal the signatures of Majorana fermions encompasses normal leads at both ends of a finite nanowire. Also in this case the common topological transition is accompanied by a pole transition and proceeds in a similar way. The qualitative difference is that far below the transition both Majorana states retain a finite width and each of the two associated poles is manifested only in the scattering from the corresponding end of the wire. In the model under consideration, the Majorana splitting retains the same sign. More detailed models, e.g. [10], predict spectacular oscillations of the splitting [24]. We stress that in the limit of the long wires $Lk_F \gg 1$ such oscillations can only start far from the common topological transition, that is, at the values of the control parameter that are parametrically bigger than v/L.

3.7 Conclusion

To conclude, we have formulated and studied a universal model that describes the crossover in the vicinity of the common topological transition for finite clean Majorana wires. Importantly, we have shown that the sharp pole topological transition takes place in the crossover interval of the control parameter and computed the dependence of the pole positions on the control parameter in this interval. We have also found a universal shape of differential conductance for this model, this enables its straightforward experimental verification.

We stress the universal character of our conclusions, in particular, the predictions for the conductance: those should hold in any sufficiently long wire with small disorder in the vicinity of the topological transition. Some features of our results have been seen in Ref. [12]: the authors have observed a narrow zero-bias peak on the background of a wider dip as seen in Fig. 3.3d (assuming G_1 is negative). From the other hand, no regular patten of peaks moving to zero upon changing the control parameter has been observed so far. More experimental data, in particular, for longer wires are required to clarify the discrepancy that can be due to sufficiently strong disorder or finite temperature effects.

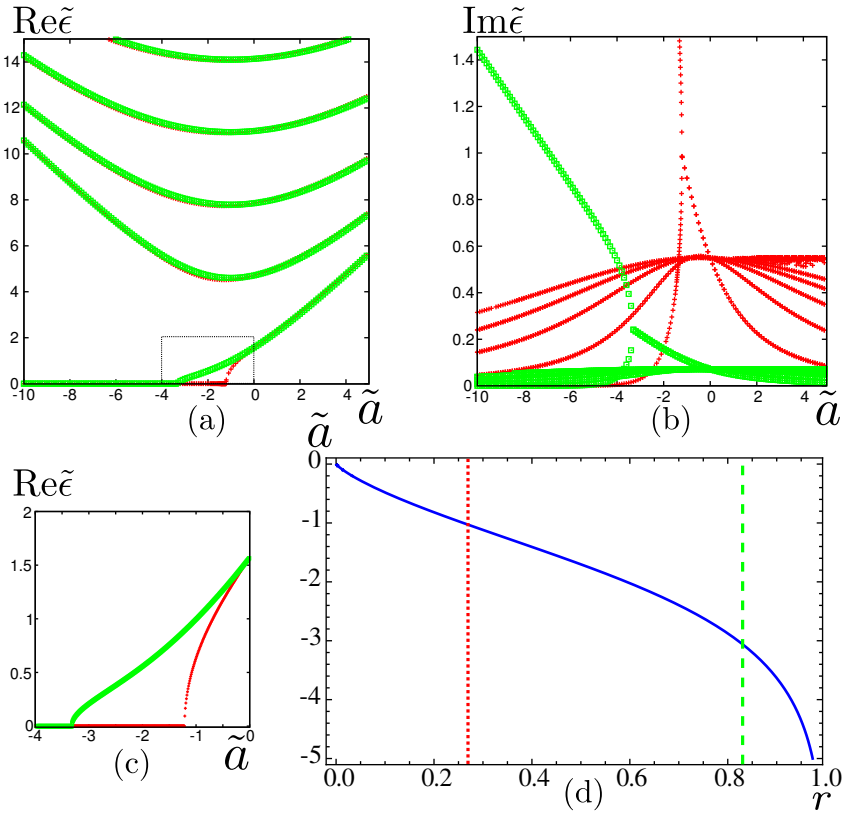

Figure 3.2. The real (a) and and imaginary (b) parts of the pole energy positions versus the control parameter $\tilde{a}$ at two values of the reflection amplitude r: $r = 0.86$ (green dots, almost isolated)and $r = 0.34$ (red crosses, almost transparent). The part of (a) within the rectangular is replotted in (c). The pole topological transition occurs at $a_0 = -1.2$ for $r = 0.86$ and $a_0 = -3.3$ for $r = 0.34$. (d) The dependence of the transition point a_0 on r.

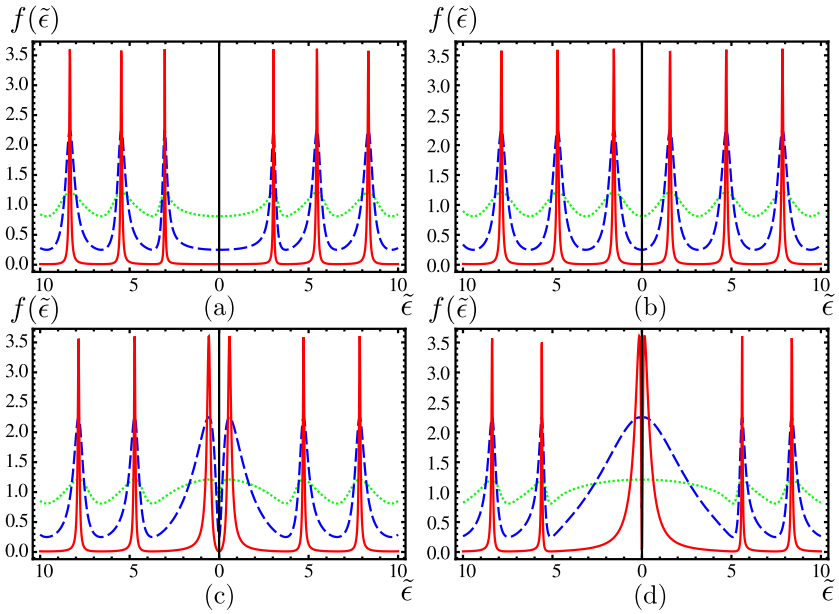

Figure 3.3. The universal bias-dependent contribution to differential Andreev conductance of the contact versus energy/voltage. Solid, dashed, dotted curves correspond to $r = 0.9, 0.5, 0.1$ respectively ($\tilde{a}_0 \approx -0.5, -1.7, -3.5$). (a) $\tilde{a} = 2$, long before the transition. (b) $\tilde{a} = 0$, the bulk topological transition, no sharp features in the conductance curves. (c) $\tilde{a} = -2$ in the crossover interval. (d) $\tilde{a} = -4$ long after the transition. The Majorana at the far end of the wire is manifested as a narrow dip at zero bias.

Bibliography

[1] G. Moore and N. Read, Nucl. Phys. B **360**, 362 (1991).

[2] D. A. Ivanov, Phys. Rev. Lett. **86**, 268 (2001).

[3] A. Y. Kitaev, Phys.-Usp. **44**, 131 (2001).

[4] A. Y. Kitaev, Ann. Phys. **303**, 2 (2003).

[5] See C. W. J. Beenakker, Annu. Rev. Con. Mat. Phys. **4**, 113 (2013) for a review.

[6] Liang Fu and C. L. Kane, Phys. Rev. Lett. **100**, 096407 (2008).

[7] A. R. Akhmerov, Johan Nilsson, and C. W. J. Beenakker, Phys. Rev. Lett. **102**, 216404 (2009).

[8] M.Sato, Y. Takahashi, and S. Fujimoto, Phys. Rev. Lett. **103**, 020401 (2009).

[9] J. D. Sau, R. M. Lutchyn, S. Tewari, and S. Das Sarma, Phys. Rev. Lett. **104**, 040502 (2010).

[10] R. M. Lutchyn, J. D. Sau, and S. Das Sarma, Phys. Rev. Lett. **105**, 077001 (2010).

[11] Y. Oreg, G. Refael, and F. von Oppen, Phys. Rev. Lett. **105**, 177002 (2010).

[12] V. Mourik, K. Zuo, S. M. Frolov, S. R. Plissard, E. P. A. M. Bakkers, and L. P. Kouwenhoven, Science **336**, 1003 (2012).

[13] M. T. Deng, C. L. Yu, G. Y. Huang, M. Larsson, P. Caroff, and H. Q. Xu, Nano Lett. **12**, 6414 (2012).

[14] A. Das, Y. Ronen, Y. Most, Y. Oreg, M. Heiblum, and H. Shtrikman, Nature Physics **8**, 887 (2012).

[15] L. P. Rokhinson, X. Liu, and J. K. Furdyna, Nature Physics **8**, 795 (2012).

[16] G. E. Volovik, *The Universe in a Helium Droplet*, Oxford University Press (2003).

[17] D. I. Pikulin and Yu. V. Nazarov, JETP Letters, **94**, 9, 693-697 (2011).

[18] D. I. Pikulin, J. P. Dahlhaus, M. Wimmer, H. Schomerus, and C. W. J. Beenakker, New J. Phys. **14**, 125011 (2012).

[19] P.-G. de Gennes, *Superconductivity of Metals and Alloys*, Addison-Wesley, Reading, MA (1986).

[20] A. R. Akhmerov, J. P. Dahlhaus, F. Hassler, M. Wimmer, and C. W. J. Beenakker, Phys. Rev. Lett. **106**, 057001 (2011).

[21] The wavefunction may be chosen real by choosing it real in arbitrary point of the setup and then using the fact that S-matrix is real in Majorana basis at zero energy.

[22] A. L. Shelankov, Zh. Eksp. Teor. Fiz., Pis'ma, **32**, 2, 122-125 (1980); G. E. Blonder, M. Tinkham, and T. M. Klapwijk, Phys. Rev. B **25**, 4515 (1982).

[23] We should also require $0 \leq r < 1$, since r passing 0 would have indicated another topological transition, in this case somewhere outside the wire [20] and not related to it.

[24] J. Klinovaja and D. Loss, Phys. Rev. B **86**, 085408 (2012).

Chapter 4

Zero-voltage conductance peak from weak antilocalization in a Majorana nanowire

4.1 Introduction

Weak localization (or antilocalization) is the systematic constructive (or destructive) interference of phase conjugate series of scattering events. In disordered metals it is time-reversal symmetry that provides for phase conjugation of backscattered electrons and protects their interference from averaging out to zero [1, 2]. A magnetic field breaks time-reversal symmetry, changing the disorder-averaged conductance by an amount δG of order e^2/h. The sign of δG distinguishes weak localization ($\delta G < 0$, conductance dip) from weak antilocalization ($\delta G > 0$, conductance peak).

Andreev reflection at a superconductor provides an alternative mechanism for phase conjugation due to particle-hole symmetry. No time-reversal symmetry is needed, so weak (anti)localization can coexist with a magnetic field and is only destroyed by a bias voltage [3, 4]. The resulting zero-bias anomaly in the conductance of a normal-metal–superconductor (NS) junction is obscured in zero magnetic field by the much larger effects of induced superconductivity, which scale with the number of

transverse modes N in the junction. These order Ne^2/h effects are suppressed by a magnetic field, only the order e^2/h effect from weak (anti)localization remains [5].

In a superconducting nanowire there is an altogether different origin of zero-bias anomalies in a magnetic field, namely the midgap state that appears at the NS interface following a topological phase transition [6–8]. Resonant Andreev reflection from the zero-mode gives a $2e^2/h$ conductance peak at zero voltage [9]. The first reports [10–12] of this signature of a Majorana fermion are generating much excitement [13]. There is an urgent need to understand the effects of disorder, in order to determine whether it may produce low-lying resonances that obscure the Majorana resonance [14–18].

These recent developments have motivated us to investigate the interplay of Majorana zero-modes and weak (anti)localization. Earlier studies of weak (anti)localization at an NS junction [3, 4, 19–21] did not consider the possibility of a topologically nontrivial phase with Majorana fermions. Calculations of the local density of states near a zero-mode [22–24] address the same physics of midgap quantum interference that we do, but cannot determine the conductance.

This paper consists of two parts: We first give in Sec. 4.2 a simple model of a disordered NS interface that allows us to obtain analytical results for δG with and without Majorana zero-modes. We then turn in Sec. 4.3 to a numerical simulation of a Majorana nanowire and compare the conductance peak due to weak antilocalization (in the topologically trivial phase) with that from a Majorana zero-mode (in the nontrivial phase). The two effects can appear strikingly similar, but in the concluding Sec. 4.4 we will discuss several ways in which they may be distinguished.

Before we present our findings, we wish to emphasise that it is not the purpose of this work to diminish the significance of experiments reporting the discovery of Majorana fermions in superconductors. On the contrary, we feel that existing [10–12] and forthcoming experiments will gain in significance if possible alternative mechanisms for zero-voltage conductance peaks in a magnetic field are identified and understood, so that they can be ruled out. Weak antilocalization was so far overlooked as one such mechanism.

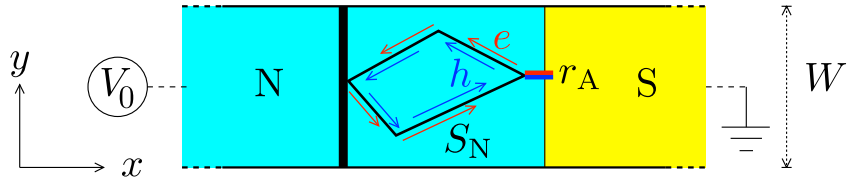

Figure 4.1. A bias voltage V_0 applied to the normal metal (N) drives a current I into the grounded superconductor (S). Electrons and holes (e, h) are scattered by disorder or a tunnel barrier in N and converted into each other by Andreev reflection at the NS interface, as described by the scattering matrices S_N and r_A. Particle-hole symmetry ensures that the phase shifts accumulated by e and h along a closed trajectory cancel, irrespective of whether time-reversal symmetry is broken or not. Such phase conjugate series of scattering events permit weak (anti)localization to persist in a magnetic field.

4.2 Analytical theory

For the analytical calculation we consider a superconducting wire that supports Q topologically protected zero-modes at the interface with a normal metal (see Fig. 4.1). The stability of Majorana zero-modes depends crucially on the fundamental symmetries of the system [25]. At most a single zero-mode is topologically protected if both time-reversal symmetry is broken (by a magnetic field) and spin-rotation symmetry is broken (by spin-orbit coupling), so that only particle-hole symmetry remains. This is called symmetry class D with $Q \in \{0, 1\}$. If the wire is sufficiently narrow (relative to the spin-orbit coupling length), an approximate chiral symmetry [26, 27] stabilizes up to N zero-modes. (The integer N is the number of propagating electronic modes through the wire in the normal state, counting both spin and orbital degrees of freedom.) This is called symmetry class BDI with $Q \in \{0, 1, 2, \ldots N\}$.

4.2.1 Scattering matrix

We construct the scattering matrix of the NS junction at the Fermi level by assuming a spatial separation of normal scattering in N and Andreev reflection in S. Within the excitation gap there is no transmission through the superconductor. The matrix r_A of Andreev reflection amplitudes from the superconductor is then a $2N \times 2N$ unitary matrix. Mode mixing at the NS interface can be incorporated in the scattering matrix S_N of the normal region, so we need not include it in r_A. It has the block

form [28, 29]

$$r_{\mathrm{A}} = \begin{pmatrix} \Gamma & \Lambda \\ \Lambda^* & \Gamma \end{pmatrix}, \quad \Gamma = \bigoplus_{m=1}^{M} \begin{pmatrix} \cos\alpha_m & 0 \\ 0 & \cos\alpha_m \end{pmatrix} \oplus \varnothing_Q \oplus \mathbb{1}_\zeta,$$
$$\Lambda = \bigoplus_{m=1}^{M} \begin{pmatrix} 0 & -i\sin\alpha_m \\ i\sin\alpha_m & 0 \end{pmatrix} \oplus \mathbb{1}_Q \oplus \varnothing_\zeta. \tag{4.1}$$

We have defined $\zeta = 0$ if the difference $N - Q$ is even and $\zeta = 1$ if $N - Q$ is odd, so that $N - Q - \zeta \equiv 2M$ is an even integer. The Andreev reflection eigenvalues $\rho_m = \sin^2\alpha_m$ that are not pinned at 0 or 1 are twofold degenerate [30].

The symbols $\mathbb{1}_n, \varnothing_n$ denote, respectively, an $n \times n$ unit matrix or null matrix for $n \geq 1$. The empty set is intended for $n = 0$. To make the notation more explicit, we give some examples of the direct sums,

$$\mathbb{1}_1 \oplus \varnothing_1 = \begin{pmatrix} 1 & 0 \\ 0 & 0 \end{pmatrix}, \quad \mathbb{1}_2 \oplus \varnothing_1 = \begin{pmatrix} 1 & 0 & 0 \\ 0 & 1 & 0 \\ 0 & 0 & 0 \end{pmatrix},$$
$$\mathbb{1}_2 \oplus \varnothing_0 = \begin{pmatrix} 1 & 0 \\ 0 & 1 \end{pmatrix}, \quad \mathbb{1}_1 \oplus \varnothing_0 = 1, \quad \mathbb{1}_0 \oplus \varnothing_1 = 0. \tag{4.2}$$

The normal region has scattering matrix

$$S_{\mathrm{N}} = \begin{pmatrix} s_0 & 0 \\ 0 & s_0^* \end{pmatrix}, \quad s_0 = \begin{pmatrix} r' & t' \\ t & r \end{pmatrix}. \tag{4.3}$$

The electron and hole blocks (with $N \times N$ reflection and transmission matrices r, r', t, t') are each others complex conjugate at the Fermi level. The off-diagonal blocks of S_{N} vanish, because the normal metal cannot mix electrons and holes. The matrix s_0 is unitary, $s_0 s_0^\dagger = 1$, without further restrictions in class D. In class BDI chiral symmetry requires that $s_0 = s_0^{\mathrm{T}}$ is also a symmetric matrix.

To separate the mixing of modes from backscattering, we make use of the polar decomposition

$$s_0 = \begin{pmatrix} U & 0 \\ 0 & V \end{pmatrix} \begin{pmatrix} -\sqrt{1-\mathcal{T}} & \sqrt{\mathcal{T}} \\ \sqrt{\mathcal{T}} & \sqrt{1-\mathcal{T}} \end{pmatrix} \begin{pmatrix} U' & 0 \\ 0 & V' \end{pmatrix}. \tag{4.4}$$

The matrices U, V, U', V' are $N \times N$ unitary matrices and $\mathcal{T} = \mathrm{diag}\,(T_1, T_2, \ldots T_N)$ is a diagonal matrix of transmission eigenvalues of the normal region. In class BDI chiral symmetry relates $U' = U^{\mathrm{T}}$, $V' = V^{\mathrm{T}}$.

4.2.2 Conductance

We combine $S_{\rm N}$ and $r_{\rm A}$ to obtain the matrix r_{he} of Andreev reflection amplitudes (from electron e to hole h) of the entire system. This calculation is much simplified in the case $\zeta = 0$, $\rho_m = 1$ ($m = 1, 2, \ldots M$) that all modes at the NS interface are Andreev reflected with unit probability. For this case $\Gamma = 0$, $N - Q = 2M$, we obtain

$$r_{he} = t'^{*}\Lambda^{*}(1 - r\Lambda r^{*}\Lambda^{*})^{-1}t, \;\; \Lambda = \sigma_y^{\oplus M} \oplus \mathbb{1}_Q. \tag{4.5}$$

The notation $\sigma_y^{\oplus M}$ signifies the $2M \times 2M$ matrix constructed as the direct sum of M Pauli matrices.

The Andreev reflection matrix determines the conductance

$$G = G_0 \,\mathrm{Tr}\, r_{he} r_{he}^{\dagger}, \;\; G_0 = 2e^2/h. \tag{4.6}$$

Substitution of the polar decomposition (4.4) gives the compact expression

$$\begin{aligned} &G/G_0 = \mathrm{Tr}\, \mathcal{T}\mathcal{M}\mathcal{T}\mathcal{M}^{\dagger}, \\ &\mathcal{M} = (1 - \Omega^{*}\sqrt{1-\mathcal{T}}\Omega\sqrt{1-\mathcal{T}})^{-1}\Omega^{*}, \;\; \Omega = V'\Lambda V^{*}. \end{aligned} \tag{4.7}$$

This is the zero-temperature conductance at the Fermi level, in the limit of zero bias voltage. Away from the Fermi level particle-hole symmetry is broken, so the electron and hole blocks in $S_{\rm N}$ are distinct unitary matrices s_e and s_h. If the bias voltage V_0 remains small compared to the excitation gap, we can keep the same $r_{\rm A}$. The finite-voltage differential conductance $\tilde{G} = dI/dV_0$ is then given by

$$\begin{aligned} &\tilde{G}/G_0 = \mathrm{Tr}\, \mathcal{T}_h\tilde{\mathcal{M}}\mathcal{T}_e\tilde{\mathcal{M}}^{\dagger}, \\ &\tilde{\mathcal{M}} = (1 - \Omega_h^{*}\sqrt{1-\mathcal{T}_e}\Omega_e\sqrt{1-\mathcal{T}_h})^{-1}\Omega_h^{*}, \\ &\Omega_e = V_e'\Lambda V_h^{*}, \;\; \Omega_h = V_h'\Lambda V_e^{*}. \end{aligned} \tag{4.8}$$

The electron matrices are evaluated at energy eV_0 above the Fermi level and the hole matrices at energy $-eV_0$ below the Fermi level. Chiral symmetry remains operative away from the Fermi level, hence $V_e' = V_e^{\rm T}$, $V_h' = V_h^{\rm T} \Rightarrow \Omega_h = \Omega_e^{\dagger}$ in class BDI. We will apply Eq. (4.8) to voltages large compared to the Thouless energy, when the electron and hole matrices may be considered to be statistically independent.

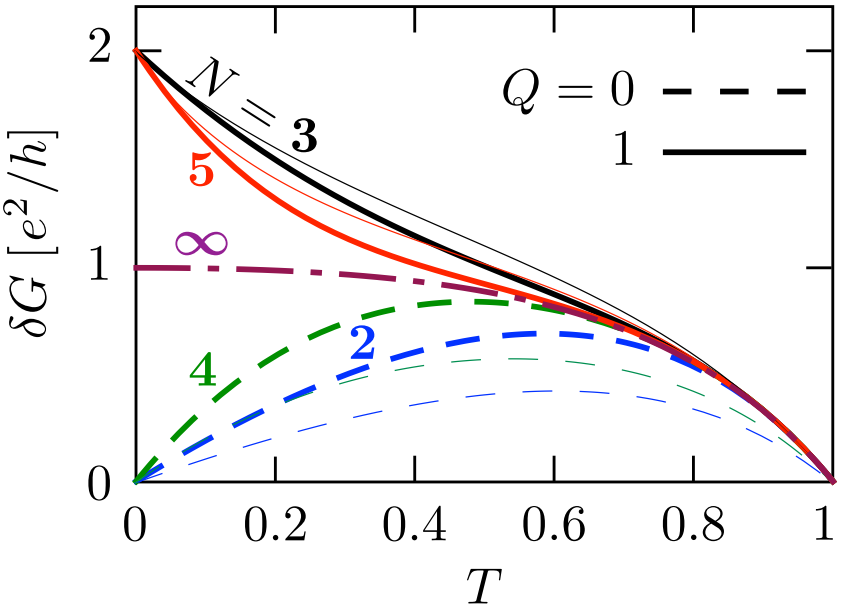

Figure 4.2. Amplitude δG of the average zero-voltage conductance peak as a function of (mode-independent) transmission probability T, in symmetry class D (thick curves) and BDI (thin curves) for different number of modes N. The superconductor is topologically trivial when N is even ($Q = 0$, dashed curves) and nontrivial when N is odd ($Q = 1$, solid curves). The dash-dotted curve is the Q-independent large-N limit (4.14).

4.2.3 Random matrix average

Isotropic mixing of the modes by scattering in the normal region means that the unitary matrices in the polar decomposition (4.4) are uniformly distributed in the unitary group $\mathcal{U}(N)$. We can calculate the average conductance for a given set of transmission eigenvalues by integration over $\mathcal{U}(N)$ with the uniform (Haar) measure. A full average would then still require an average over the T_n's, but if these are dominated by a tunnel barrier they will fluctuate little and the partial average over the unitary matrices is already informative.

The calculation is easiest if all T_n's have the same value $0 \leq T \leq 1$. The average zero-voltage conductance $\langle G \rangle$ is then given by the integral

$$\langle G \rangle = T^2 G_0 \int_0^{2\pi} d\phi\, \rho(\phi) \left| 1 - (1-T)e^{i\phi} \right|^{-2}, \tag{4.9}$$

with $\rho(\phi) = \langle \sum_n \delta(\phi - \phi_n) \rangle$ the density on the unit circle of the eigenvalues $e^{i\phi_n}$ of $\Omega\Omega^*$. The corresponding finite-voltage expression has a uniform $\rho = N/2\pi$, leading to

$$\langle \tilde{G} \rangle = NG_0T/(2-T), \tag{4.10}$$

irrespective of the symmetry class and independent of the topological quantum number Q.

The zero-voltage average (4.9) does depend on Q and is different for class D and BDI. The calculations are given in the Appendix. Explicit expressions in class D are

$$\frac{\langle G \rangle_{\rm D}}{G_0} = \begin{cases} 2T & \text{for } N=2, \ Q=0, \\ 1+2T^2 & \text{for } N=3, \ Q=1, \\ 2T(2-T+T^2) & \text{for } N=4, \ Q=0, \\ 1+2T^2(3-2T+T^2) & \text{for } N=5, \ Q=1. \end{cases} \tag{4.11}$$

The Q-dependence appears to second order in the reflection probability $R = 1 - T$, while the general first-order result

$$\langle G/G_0 \rangle_{\rm D} = N(1-2R) + 2R + \mathcal{O}(R^2) \tag{4.12}$$

is Q-independent. The corresponding expressions in class BDI are more lengthy, and we only record the small-R result

$$\langle G/G_0 \rangle_{\rm BDI} = N(1-2R) + 2R\frac{Q^2+N}{N+1} + \mathcal{O}(R^2), \tag{4.13}$$

to show that it is Q-dependent already to first order in R. These are all finite-N results. In the large-N limit the Q-dependence is lost,

$$\langle G/G_0 \rangle = \frac{NT}{2-T} + \frac{2(1-T)}{(2-T)^2} + \mathcal{O}(N^{-1}), \tag{4.14}$$

irrespective of the symmetry class.

As illustrated in Fig. 4.2, for this case that all T_n's have the same value T the difference $\delta G = \langle G \rangle - \langle \tilde{G} \rangle$ is positive, corresponding to weak *anti*localization and a conductance *peak*. The sign of the effect may change if the T_n's are very different, in particular in class BDI — which has $\delta G < 0$ in a quantum dot geometry (circular ensemble) [29]. This is a special feature of quantum interference in a magnetic field, that the distinction between weak localization and antilocalization is not uniquely determined by the symmetry class [21, 31, 32].

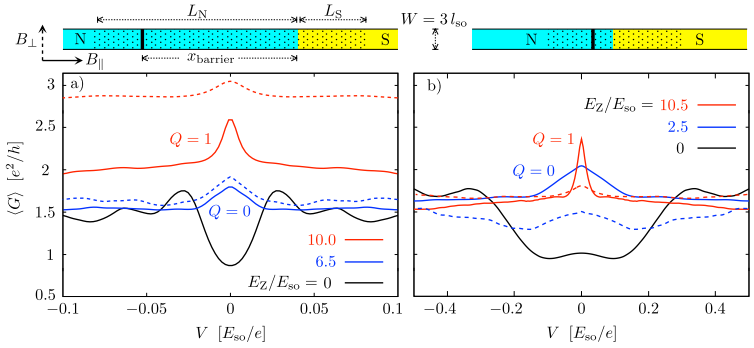

Figure 4.3. Disorder-averaged differential conductance as a function of bias voltage, for a nanowire modeled by the Hamiltonian (4.15). The two panels a) and b) correspond to the two geometries shown to scale above each plot. (The solid vertical line indicates the position of the tunnel barrier, relative to the NS interface; disordered regions are dotted.) Each panel shows data for zero magnetic field (black), and for two nonzero magnetic field values (blue and red). The solid curves are for parallel field $B_\parallel$ and the dashed curves for perpendicular field $B_\perp$. The system is topologically trivial ($Q = 0$) in all cases except for the red solid curves ($Q = 1$). (The parameter values are listed in Ref. 35.)

4.3 Simulation of a microscopic model

The random-matrix calculation serves a purpose for a qualitative understanding of the weak antilocalization effect. For a quantitative description we need to relax the assumption of channel-independent T_n's. For that purpose we now turn to a microscopic model of a Majorana nanowire.

4.3.1 Model Hamiltonian

Folowing Refs. 6, 7, we consider a conducting channel parallel to the x-axis on a substrate in the x-y plane (width W, Fermi energy E_F), in a magnetic field $\boldsymbol{B}$ (orientation $\hat{n}$, Zeeman energy $E_Z = \frac{1}{2} g_{\rm eff} \mu_B B$), with Rashba spin-orbit coupling (characteristic energy $E_{so} = m_{\rm eff} \alpha_{so}^2/\hbar^2$, length $l_{so} = \hbar^2/m_{\rm eff}\alpha_{so}$), and induced s-wave superconductivity (excita-

tion gap Δ_0). The Hamiltonian is

$$\begin{aligned}\mathcal{H} &= \begin{pmatrix} H_0 - E_\mathrm{F} & \Delta\sigma_y \\ \Delta^*\sigma_y & E_\mathrm{F} - H_0^* \end{pmatrix}, \\ H_0 &= \frac{p_x^2 + p_y^2}{2m_\mathrm{eff}} + U(x,y) + \frac{\alpha_\mathrm{so}}{\hbar}(\sigma_x p_y - \sigma_y p_x) + E_Z \hat{n}\cdot\boldsymbol{\sigma}.\end{aligned} \tag{4.15}$$

The electrostatic potential $U = U_\mathrm{gate} + \delta U$ contains the gate potential U_gate that creates the tunnel barrier and the impurity potential δU that varies randomly from site to site on a square lattice (lattice constant a), distributed uniformly in the interval $(-U_\mathrm{disorder}, U_\mathrm{disorder})$. The disordered region is $-L_\mathrm{N} < x < L_\mathrm{S}$, an NS interface is constructed by increasing the pair potential Δ from 0 to Δ_0 at $x = 0$, and a rectangular barrier of height U_barrier, thickness $\delta L_\mathrm{barrier}$, is placed at $x = -x_\mathrm{barrier}$. The conductance of the normal region ($x < 0$) contains a contribution G_disorder from disorder and G_barrier from the barrier.

The orientation of the magnetic field plays an important role [6, 7]: It lies in the x-y plane to eliminate orbital effects on the superconductor and we will only include its effect on the electron spin (through the Zeeman energy). A topologically nontrivial phase needs a nonzero excitation gap for $E_Z > \Delta_0$, which requires a parallel magnetic field $B_\parallel$ ($\hat{n} = \hat{x}$). We will consider that case in the next subsection, and then discuss the case of a perpendicular magnetic field $B_\perp$ ($\hat{n} = \hat{y}$) in Sec. 4.3.3.

4.3.2 Average vs. sample-specific conductance

To avoid the complications from chiral symmetry we first focus on a relatively wide junction, $W = 3\,l_\mathrm{so}$, when symmetry class D (rather than BDI) applies [29]. (We turn to class BDI in the next subsection.) The normal region has $N = 8$ propagating modes (including spin) in zero magnetic field, for $E_\mathrm{F} = 12\,E_\mathrm{so}$. The topological quantum number Q was determined both from the determinant of the reflection matrix [33, 34], and independently by counting the gap closings and reopenings upon increasing the magnetic field. A transition from $Q = 0$ to $Q = 1$ is realized by increasing $B_\parallel$ at fixed $\Delta_0 = 8\,E_\mathrm{so}$.

Results are shown in Fig. 4.3 (solid curves) for two geometries, one with the tunnel barrier far from the NS and another with the barrier close to the interface [35].

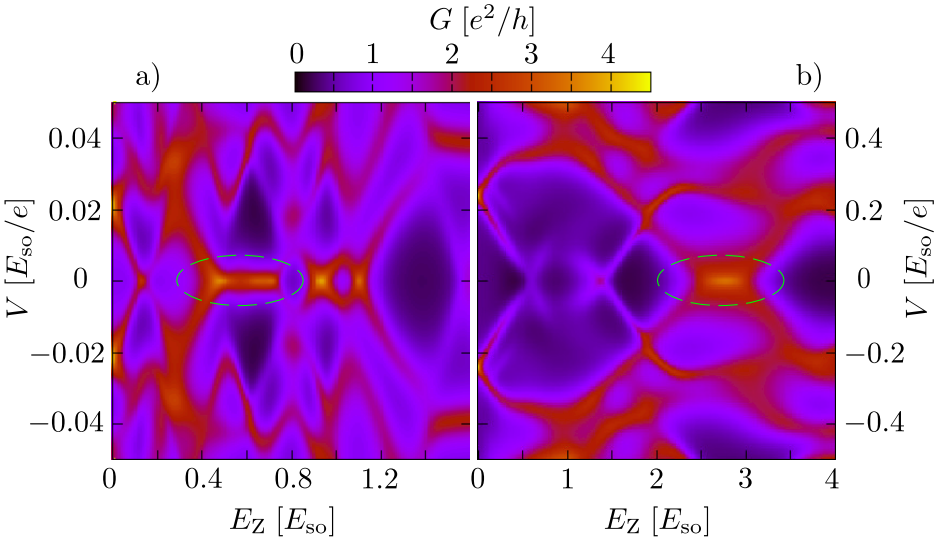

Figure 4.4. Numerical simulation of a nanowire for a single disorder realization (no averaging). The color scale gives the differential conductance as a function of bias voltage (vertical axis) and parallel magnetic field (horizontal axis). The parameters in panels a,b correspond to those in Fig. 4.3a,b, as listed in Ref. 35. The magnetic field range in both panels is in the topologically trivial phase ($Q = 0$), but still exhibits a conductance peak pinned to zero voltage (green circle).

The disorder-averaged conductance shows a zero-voltage peak in a magnetic field, regardless of whether the nanowire is topologically trivial ($Q = 0$) or nontrivial ($Q = 1$). The peak disappears in zero magnetic field and instead a conductance minimum develops, indicative of an induced superconducting minigap in the normal region. The two geometries in panels 4.3a and 4.3b show comparable results, the main difference being a broadening of the zero-bias peak when the tunnel barrier is brought closer to the NS interface — as expected from the increase in Thouless energy [36]. The shallow maximum which develops around zero voltage in the $B = 0$ curve of panel 4.3b is a precursor of the reflectionless tunneling peak, which appears in full strength when the barrier is placed at the NS interface [5].

This all applies to the average conductance in an ensemble of disordered nanowires. Individual members of the ensemble show mesoscopic, sample-specific conductance fluctuations, in addition to the sys-

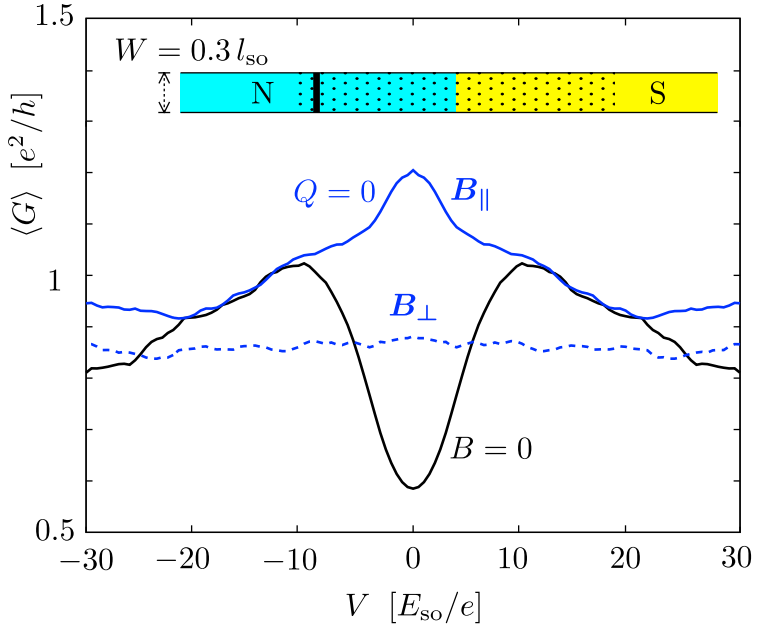

Figure 4.5. Same as Fig. 4.3, but now for a narrower wire in symmetry class BDI (rather than D). The system is topologically trivial, without Majorana zero-modes. The weak antilocalization peak vanishes if the magnetic field is rotated from $B_\parallel$ to $B_\perp$. (The parameter values are listed in Ref. 38.)

tematic weak antilocalization effect. For some disorder realizations the zero-voltage conductance peak remains clearly visible, see Fig. 4.4. The peak sticks to zero bias voltage over a relatively wide magnetic field range, even though the superconductor is topologically trivial ($Q = 0$). The appearance and disappearance of the peak is not associated with the closing and reopening of an excitation gap, so it cannot produce Majorana fermions [37].

4.3.3 Parallel vs. perpendicular magnetic field

So far we considered a class D nanowire with magnetic field $B_\parallel$ parallel to the wire axis. In a perpendicular magnetic field $B_\perp$ (perpendicular to the wire in the plane of the substrate) the symmetry class remains D (broken time-reversal and spin-rotation symmetry), although the topologically nontrivial phase disappears [6, 7]. We therefore expect the class D zero-bias peak to persist in a perpendicular field as a result of the

weak antilocalization effect.

This expectation is borne out by the computer simulations, see the dashed curves in Fig. 4.3. A zero-bias peak exists for both $B_\perp$ and $B_\parallel$. If the nanowire is topologically trivial, there is not much difference in the peak height for the two magnetic field directions (compare blue solid and dashed curves). In contrast, if the nanowire is topologically nontrivial for parallel field then the peak is much reduced in perpendicular field (red solid versus dashed curves). The disappearance of the Majorana zero-mode and the collapse of the zero-bias peak may be accompanied by the appearance of propagating modes in the superconducting part of the nanowire. This explains the increased background conductance in the red dashed curve of Fig. 4.3a.

The effect of a magnetic field rotation is entirely different when $W \lesssim l_{\rm so}$ and the symmetry class is BDI rather than D [26, 29]. The term $\sigma_x p_y$ in the Hamiltonian (4.15) can then be neglected, so that $\mathcal{H}$ commutes with σ_y in a perpendicular magnetic field ($\hat{n} = \hat{y}$). The two spin components along $\pm\hat{y}$ decouple and for each spin component separately the particle-hole symmetry is broken. We therefore expect both the Majorana resonance and the weak antilocalization peak to disappear in a perpendicular magnetic field for sufficiently narrow wires.

This is demonstrated by the computer simulations shown in Fig. 4.5, for the average conductance in a topologically trivial wire of width $W = 0.3\,l_{\rm so}$. The main difference with the data in Fig. 4.3 is that the symmetry class is now BDI rather than D, because of the narrower wire. This change of symmetry class does not significantly affect the weak antilocalization peak in a parallel magnetic field. But if the magnetic field is rotated to a perpendicular direction, the peak disappears — as expected for a class BDI nanowire.

4.3.4 Effects of thermal averaging

All results presented so far are in the zero-temperature limit. We calculate the temperature dependence of the differential conductance from the finite-T_0 and finite-V_0 generalization of Eq. (4.6),

$$G = \frac{2e}{h}\int_{-\infty}^{\infty} d\varepsilon\, \frac{df(\varepsilon - eV_0)}{dV_0}\, \mathrm{Tr}\, r_{he}(\varepsilon) r_{he}^\dagger(\varepsilon), \tag{4.16}$$

$$f(\varepsilon) = \frac{1}{1+\exp(\varepsilon/k_{\rm B}T_0)}. \tag{4.17}$$

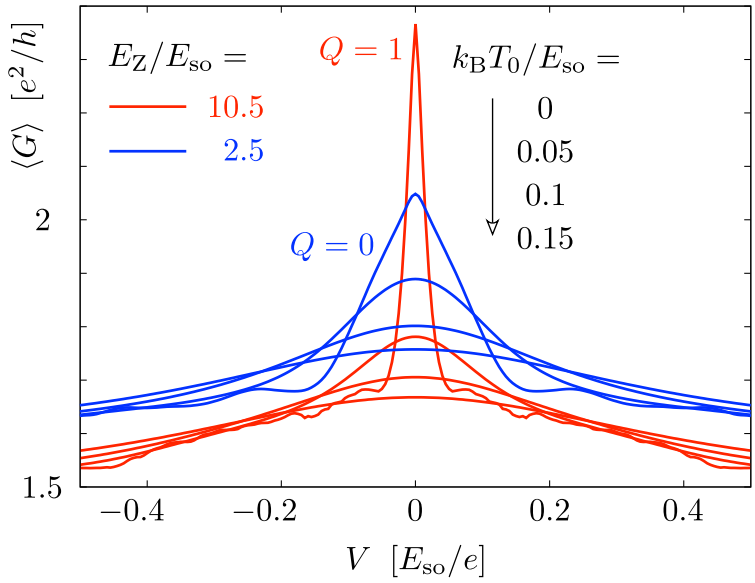

Figure 4.6. Temperature dependence of the conductance peaks from Fig. 4.3b. The four blue curves ($Q = 0$, topologically trivial) correspond from top to bottom to four increasing temperatures, and likewise the four red curves ($Q = 1$, topologically nontrivial).

Thermal averaging at a nonzero temperature T_0 broadens the conductance peak around $V_0 = 0$ and reduces its height, at constant area $\int G\, dV_0$ under the peak.

This effect of thermal averaging applies to both the weak antilocalization peak and to the Majorana resonance, but the characteristic temperature scale is different, as shown in Fig. 4.6. The Majorana zero-mode is more sensitive to thermal averaging because it is more tightly bound to the NS interface, with a smaller Thouless energy and therefore a smaller characteristic temperature.

4.4 Discussion

In conclusion, we have shown that random quantum interference by disorder in a superconducting nanowire can systematically produce a zero-voltage conductance peak in the absence of time-reversal symmetry. This weak antilocalization effect relies on the same particle-hole

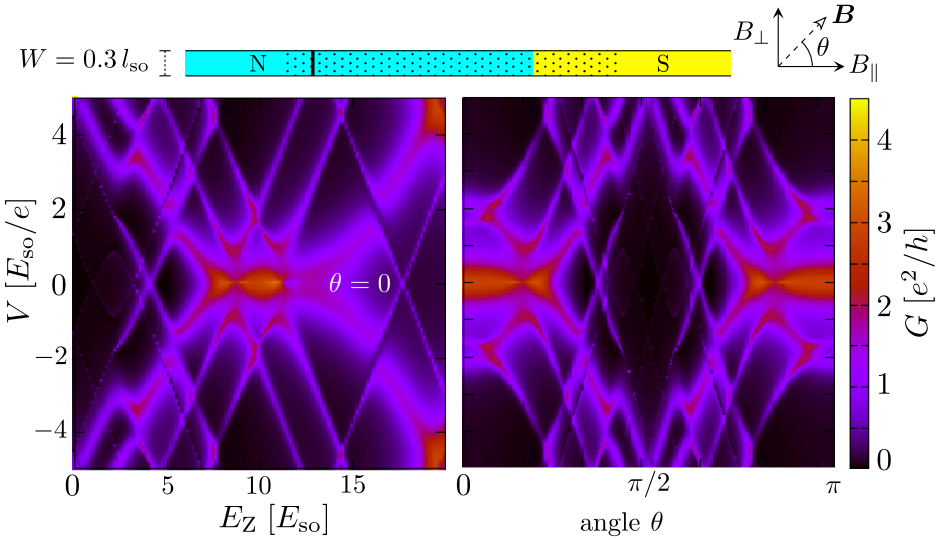

Figure 4.7. Differential conductance for a single disorder realization of a nanowire ($N = 2$ spin-resolved modes, parameter values are listed in Ref. 40). The left panel shows the appearance of a zero-voltage peak in a range of magnetic field values, for $\boldsymbol{B}$ parallel to the wire. The right panel shows the dependence on the orientation of the magnetic field, for a fixed field strength ($E_{\rm Z} = 10\,E_{\rm so}$). The zero-voltage peak vanishes if $\boldsymbol{B}$ is perpendicular to the wire. This is the same phenomenology as for a Majorana resonance, but here it happens in the topologically trivial phase.

symmetry that protects the Majorana zero-mode, but it exists in both the topologically trivial and nontrivial phase of the superconductor. A conclusive demonstration of Majorana fermions will need to rule out this alternative mechanism for a conductance peak.

There are several strategies one might follow for this purpose:

- Increasing the tunnel barrier with a gate voltage suppresses the weak antilocalization effect, but not the Majorana resonance. The resonance does become narrower, so at finite temperatures thermal smearing will still lead to a suppression with increasing barrier height and this might not be the most effective strategy to distinguish the two effects.

- The disappearance of the conductance peak when the magnetic field is rotated (in the plane of the substrate) towards a direction perpendicular to the wire, the technique used in Refs. 10, 12, can

identify the Majorana zero-mode — but only if the ratio W/l_{so} is sufficiently large that the wire is in class D rather than BDI. In class BDI the Zeeman energy in the rotated field commutes with the Rashba energy, precluding the weak antilocalization effect as well as the Majorana resonance. Both Refs. 10, 12 have $W \lesssim l_{so}$ and are believed to be in class BDI [16, 26], so this complication seems quite relevant.

- Measuring the conductance through a single-mode point contact is a very effective strategy: for $N = 1$ the zero-temperature conductance $G = Q \times 2e^2/h$ directly measures the topological quantum number even without any tunnel barrier [39], and this signature of a Majorana zero-mode is quite robust against finite temperatures. (The chararacteristic energy scale is the induced superconducting gap in the region between the point contact and the superconductor.) The single mode in the point contact should be spin resolved for this to work: If instead the point contact transmits both spins in one orbital mode ($N = 2$), then the ambiguity between weak antilocalization and the Majorana resonance remains (see Fig. 4.7).

- The Majorana resonance from a wire of finite length should split into two at the lowest temperatures, because of the nonzero overlap of the zero-modes at the two ends of the wire [12]. No such systematic splitting will occur for the weak antilocalization peak.

4.5 Appendix

4.5.1 Random-matrix theory

To evaluate the average conductance (4.9) we seek the density of the eigenvalues $x_n = e^{i\phi_n}$ of the product $X = \Omega\Omega^*$ of the unitary matrix Ω and its complex conjugate. We denote $\mu_n = \cos\phi_n \in [-1, 1]$ and determine the joint probability distribution $P(\{\mu_n\})$ using methods from random-matrix theory [41].

In symmetry class D, we have $\Omega = V'\Lambda V^*$ with V and V' independently and uniformly distributed according to the Haar measure dU of the unitary group $\mathcal{U}(N)$. Because $d(UU') = dU$ for a fixed unitary matrix U', the matrix $\Omega \equiv U$ is itself uniformly distributed in $\mathcal{U}(N)$.

In class BDI, we have $V' = V^{\mathrm{T}}$ and we may write $\Omega \equiv U\lambda U^{\dagger}$ with U uniformly in $\mathcal{U}(N)$. The diagonal matrix $\lambda = \mathrm{diag}(\lambda_1, \lambda_2, \ldots \lambda_N)$ contains the eigenvalues $\lambda_n = \pm 1$ of Λ. The number $q = |Q|$ of Majorana zero-modes is encoded in the topological invariant $Q = \mathrm{Tr}\,\Lambda = \sum_n \lambda_n$. (For full generality we allow Q to also take on negative values, but the final result will only depend on the absolute value q.)

Brownian motion of unitary matrices

We employ Dyson's Brownian motion approach [42], which sets up a stochastic process for the unitary matrix U whose stationary distribution coincides with the Haar measure on $\mathcal{U}(N)$. In each infinitesimal step of the process, $U \to U\exp(iH)$, where H is a Hermitian matrix from the Gaussian unitary ensemble, with identically normal distributed complex numbers $H_{lm} = H^*_{ml}$ $(l \leq m)$, $\overline{H_{lm}} = 0$, $\overline{H_{kl}H_{mn}} = \delta_{kn}\delta_{lm}\tau$, $\overline{H_{kl}H^*_{mn}} = \delta_{km}\delta_{ln}\tau$; the limit $\tau \to 0$ is implied to generate infinitesimal increments.

The corresponding increments $\delta\mu_n$ can be calculated in perturbation theory. The drift coefficients $c_l = \lim_{\tau\to 0} \tau^{-1}\overline{\delta\mu_l}$ and the diffusion coefficients $c_{lm} = \lim_{\tau\to 0} \tau^{-1}\overline{\delta\mu_l\delta\mu_m}$ follow by averaging over the random variables in H. As we will see, the symmetries in the classes D and BDI are restrictive enough so that these coefficients can be expressed in terms of the quantities μ_n alone, without requiring data from the eigenvectors of X. Thus, the stochastic process for these quantities closes.

Introducing a fictitious time t, the evolution of the joint probability distribution is governed by a Fokker-Planck equation,

$$\frac{\partial P}{\partial t} = \left[-\sum_l \frac{\partial}{\partial \mu_l} c_l + \frac{1}{2}\sum_{l,m} \frac{\partial}{\partial \mu_l}\frac{\partial}{\partial \mu_m} c_{lm} \right] P(\{\mu_n\}, t). \tag{4.18}$$

The stationary solution $P(\{\mu_n\})$, for which the right-hand-side of the Fokker-Planck equation vanishes, is the required eigenvalue distribution.

Symmetry class D

In class D we have $X = UU^*$ with U uniformly distributed in $\mathcal{U}(N)$. Notice that the operation of complex conjugation is basis dependent; if $B = A^*$ in one basis then this relation is only preserved under orthogonal transformations, but not under general unitary transformations.

Thus, we work in a fixed basis $|r\rangle$ (at most permitting orthogonal basis changes), and define for any $|\psi\rangle = \sum_r \psi_r |r\rangle$ a complex-conjugated vector $|\psi^*\rangle \equiv \sum_r \psi_r^* |r\rangle$. As usual, $\langle\psi| = \sum_r \psi_r^* \langle r|$; thus $\langle\psi^*| = \sum_r \psi_r \langle r|$.

The matrices X and U are unitary and obey $\mathrm{Det}\, X = |\mathrm{Det}\, U|^2 = 1$. Moreover, the matrix X^* has the same eigenvalues $x_1, x_2, \ldots x_N$ as the matrix X. For even N, it follows that all eigenvalues appear in complex-conjugated pairs; every eigenvalue x_k has a partner $x_{\bar{k}} = x_k^* = x_k^{-1}$. For odd N, in addition to such pairs there is a single unpaired eigenvalue, denoted as x_N, which (because of the constraint on the determinant) is pinned at $x_N = 1$. The paired eigenvectors are related according to

$$|\bar{k}\rangle = \xi_k U |k^*\rangle. \tag{4.19}$$

Here we have to set ξ_k such that $\xi_k^2 = \lambda_k$; this guarantees that the relation between both eigenvectors in a pair is reciprocal, $|\bar{\bar{k}}\rangle = |k\rangle$. Observing that the eigenvectors form an orthogonal basis, we find the matrix elements

$$\langle k|U|l^*\rangle = \xi_k \delta_{k\bar{l}} = (\langle k^*|U^*|l\rangle)^* = \langle l|U^{\mathrm{T}}|k^*\rangle. \tag{4.20}$$

With help of these matrix elements we can now evaluate the drift and diffusion coefficients. In second-order perturbation theory,

$$\delta x_l = \langle l|\delta X|l\rangle + \sum_k{}' \frac{\langle l|\delta X|k\rangle\langle k|\delta X|l\rangle}{x_l - x_k}, \tag{4.21}$$

where the prime restricts the sum to $k \neq l$ while

$$\delta X = iUHU^* - iXH^* + UHU^*H^* - \tfrac{1}{2}UH^2U^* - \tfrac{1}{2}XH^{*2} \tag{4.22}$$

is the increment of X to leading order in τ. The Gaussian averages are now carried out according to the rules

$$\langle k|AHB|l\rangle\langle m|CHD|n\rangle = \tau\langle k|AD|n\rangle\langle m|CB|l\rangle, \tag{4.23}$$

$$\langle k|AHB|l\rangle\langle m|CH^*D|n\rangle = \tau\langle k|AC^{\mathrm{T}}|m^*\rangle\langle n^*|D^{\mathrm{T}}B|l\rangle. \tag{4.24}$$

In particular, $\overline{H^2} = N\tau$, $\overline{UHU^*H^*} = \tau UU^\dagger = \tau$, and

$$\begin{aligned}
&\overline{\langle l|UHU^* - XH^*|k\rangle\langle k|UHU^* - XH^*|l\rangle} \\
&\quad = 2\tau\langle l|X|l\rangle\langle k|X|k\rangle - \tau\langle l|U^T|k^*\rangle\langle l^*|U^*|k\rangle \\
&\qquad - \tau\langle k|U^T|l^*\rangle\langle k^*|U^*|l\rangle \\
&\quad = 2\tau x_l x_k - \tau\delta_{l\bar{k}}(x_l + x_{\bar{l}}),
\end{aligned} \tag{4.25}$$

where we invoked Eq. (4.20). We thus obtain

$$\overline{\delta x_l} = \tau - N\tau x_l - \tau \sum_k{}' \frac{2x_l x_k - \delta_{l\bar{k}}(x_l + x_{\bar{l}})}{x_l - x_k}. \tag{4.26}$$

Analogously, we find

$$\overline{\delta x_l \delta x_m} = \overline{\langle l|\delta X|l\rangle\langle m|\delta X|m\rangle} = -2\tau\delta_{lm}x_l^2 + 2\tau\delta_{l\bar{m}}. \tag{4.27}$$

Note that these expressions only depend on the eigenvalues. We remark that for the pinned unpaired eigenvalue $x_N = 1$, occurring if N odd, these relations deliver $\overline{\delta x_N} = \overline{(\delta x_N)^2} = 0$.

We now pass over to the quantities $\mu_l = (x_l + x_{\bar{l}})/2$, and restrict the index l such that it enumerates the pairs of eigenvalues. For even N we then find

$$\overline{\delta\mu_l} = \tau - 2\tau\mu_l - 2\tau(\mu_l^2 - 1)\sum_k{}' \frac{1}{\mu_l - \mu_k}, \tag{4.28}$$

while for odd N we have

$$\overline{\delta\mu_l} = -3\tau\mu_l - 2\tau(\mu_l^2 - 1)\sum_k{}'' \frac{1}{\mu_l - \mu_k}, \tag{4.29}$$

where the double-prime excludes the pinned eigenvalue. Furthermore,

$$\overline{\delta\mu_l \delta\mu_m} = 2\tau(1 - \mu_l^2)\delta_{lm}. \tag{4.30}$$

The stationarity condition of the associated Fokker-Planck equation (4.18) can be expressed as

$$\frac{\partial}{\partial\mu_l}\overline{\delta\mu_l}P = \frac{1}{2}\frac{\partial^2}{\partial\mu_l}\overline{(\delta\mu_l)^2}P. \tag{4.31}$$

For even $N = 2M$, this is solved by

$$P(\mu_1, \mu_2, \ldots \mu_M) \propto \prod_{k=1}^{M} \frac{1+\mu_k}{\sqrt{1-\mu_k^2}} \prod_{l<m=1}^{M} (\mu_l - \mu_m)^2, \tag{4.32a}$$

up to a normalization constant. Each of the μ_n's ($n = 1, 2, \ldots M$) is twofold degenerate. For odd $N = 2M + 1$ one eigenvalue is pinned at $+1$, and the remaining ones are twofold degenerate with distribution

$$P(\mu_1, \mu_2, \ldots \mu_M) \propto \prod_{k=1}^{M} \sqrt{1-\mu_k^2} \prod_{l<m=1}^{M} (\mu_l - \mu_m)^2. \tag{4.32b}$$

This concludes our derivation of the eigenvalue distribution of UU^* with U uniform in $\mathcal{U}(N)$. We have not found the result (4.32) in the literature, but there is a curious correspondence with the known [41, 43] eigenvalue distribution of orthogonal matrices (uniformly distributed according to the Haar measure). An $(N+1)\times(N+1)$ orthogonal matrix O with determinant -1 has one eigenvalue pinned at -1. If we exclude that eigenvalue, the remaining N eigenvalues of O have same probability distribution as the N eigenvalues of UU^*.

Brownian motion of orthogonal matrices

As an independent demonstration of this correspondence between the eigenvalue distributions of UU^* and O, we have investigated the Brownian motion of orthogonal matrices. Let O be a random $(N+1)\times(N+1)$-dimensional matrix in the orthogonal group, constrained to the sector $\mathrm{Det}\, O = -1$.

The Brownian motion is induced by $O(1+A+A^2/2)$, where (in the fixed basis) $A = -A^{\mathrm{T}}$ is a real antisymmetric matrix, with $\overline{A_{lm}^2} = \tau$. Due to the condition on the determinant, there is always one eigenvalue pinned at $x_{N+1} = -1$, while an additional eigenvalue is pinned at $x_N = 1$ if N is odd. All other eigenvalues appear in pairs x_l, $x_{\bar{l}}$, with $|\bar{l}\rangle = |l^*\rangle$ (no additional factors are required).

We calculate the increments and average:

$$\begin{aligned}
\delta x_l &= \tfrac{1}{2}\langle l|OA^2|l\rangle + \sum_{k\neq l}\frac{\langle l|OA|k\rangle\langle k|OA|l\rangle}{x_l - x_k}\\
&\Rightarrow \overline{\delta x_l} = -\tfrac{1}{2}\tau N x_l + \tau\sum_{k\neq l}\frac{x_l x_k(\delta_{k\bar{l}}-1)}{x_l - x_k}, \qquad (4.33)\\
\delta x_l \delta x_k &= \langle l|OA|l\rangle\langle k|OA|k\rangle\\
&\Rightarrow \overline{\delta x_l \delta x_k} = \tau x_l x_k(\delta_{l\bar{k}} - \delta_{lk}) = \tau(\delta_{l\bar{k}} - x_l^2\delta_{lk}). \qquad (4.34)
\end{aligned}$$

(Note that $\langle l|A|l\rangle$ does not vanish if $|l\rangle$ is complex, as is generally the case for the unpinned eigenvalues.)

As before, in passing over to μ_l we restrict indices to enumerate different pairs. For N even, we find [considering that the restricted sum

has $(N-2)/2$ terms]

$$\begin{aligned}\overline{\delta\mu_l} &= \tfrac{1}{2}\tau - \tfrac{1}{2}\tau N\mu_l - \tau \sum_{k\neq l,N+1} \frac{\mu_l\mu_k - 1}{\mu_l - \mu_k} \\ &= \tfrac{1}{2}\tau - \tau\mu_l - \tau(\mu_l^2 - 1) \sum_{k\neq l,N+1} \frac{1}{\mu_l - \mu_k},\end{aligned} \tag{4.35}$$

while if N is odd [where the restricted sum has $(N-3)/2$ terms],

$$\begin{aligned}\overline{\delta\mu_l} &= -\tfrac{1}{2}\tau N\mu_l - \tau \sum_{k\neq l,N,N+1} \frac{\mu_l\mu_k - 1}{\mu_l - \mu_k} \\ &= -\tfrac{3}{2}\tau\mu_l - \tau(\mu_l^2 - 1) \sum_{k\neq l,N,N+1} \frac{1}{\mu_l - \mu_k}.\end{aligned} \tag{4.36}$$

Furthermore,

$$\overline{\delta\mu_l\delta\mu_k} = \tau(1-\mu_l^2)\delta_{lk}. \tag{4.37}$$

Comparison with Eqs. (4.28)–(4.30) shows that these are the same average increments, if we rescale τ by a factor 2. The eigenvalues of UU^* and O therefore execute the same Brownian motion process, with the same stationary solution (4.32).

Symmetry class BDI

In class BDI we have $X = U\lambda U^\dagger U^*\lambda U^{\mathrm{T}}$, with U uniform in $\mathcal{U}(N)$ and λ a fixed diagonal matrix with entries ± 1 that sum up to Q. Since here the matrix X is symmetric, $X = X^{\mathrm{T}}$, it is now diagonalized by an orthogonal transformation; thus, the eigenvectors $|k\rangle = |k^*\rangle$ are real. As in class D, eigenvalues appear in complex-conjugate pairs, apart from eigenvalues pinned at 1. We observe that Ω mediates between the associated eigenvector, $|\bar{k}\rangle = \xi_k\Omega|k\rangle = \xi_k^*\Omega^*|k\rangle$. In order to treat the partners symmetrically we have to require that that $|\bar{k}\rangle$ is also real, so ξ_k compensates any complex overall factor. It then follows that $\langle k|\Omega\Omega^*|k\rangle = \xi_k^2 = \lambda_k$, and thus the coefficients ξ_k are related to the eigenvalues as in class D.

To identify the pinned eigenvalues note that $\Omega = \Omega^\dagger = \Omega^{-1}$ is both Hermitian and unitary, and thus has eigenvalues ± 1. Let $\Omega_\pm$ be the eigenspace for each set of eigenvalues, and $\Omega_\pm^*$ the analogous eigenspace for Ω^*, which is spanned by the complex-conjugated vectors. We denote $\xi = \operatorname{sign} Q$. The space $[\mathrm{span}(\Omega_{-\xi}, \Omega_{-\xi}^*)]^\perp$ is then of dimension $q = |Q|$

(barring accidental degeneracies), and all of the vectors in this space obey $X|k\rangle = |k\rangle$. Thus X has $q = |Q|$ eigenvalues pinned at 1. For each pinned eigenvalue, insisting that $|\bar{k}\rangle = |k\rangle$ implies $\Omega|k\rangle = \Omega^*|k\rangle = \xi|k\rangle$, $\xi = \operatorname{sign} Q = \pm 1$ (consistent with the property that these states lie in the joint subspace of Ω_ξ and Ω^*_ξ).

With these additional properties in hand, the evaluation of drift and diffusion coefficients can proceed along the same steps as before. With the specified form of X, the incremental step of U carries over to an increment

$$\begin{aligned}\delta X = {} & iU[H,\lambda]U^\dagger\Omega^* - i\Omega U^*[H^*,\lambda]U^{\mathrm{T}} \\ & + \tau Q(\Omega^* + \Omega) + 2\tau(1 - X) - 2N\tau X,\end{aligned} \tag{4.38}$$

where we already averaged terms of second order in H; in particular, terms such as $\overline{UH\lambda HU^\dagger U^*\lambda U^{\mathrm{T}}} = \tau Q\Omega^*$ produce the topological invariant Q. The associated eigenvalue increment averages to

$$\begin{aligned}\overline{\delta x_l} = {} & -2N\tau x_l + \tau Q\langle l|\Omega^* + \Omega|l\rangle + 2\tau(1 - x_l) - {\sum_k}'(x_l - x_k)^{-1}\times \\ & \times\overline{\langle l|U[H,\lambda]U^\dagger\Omega^* - \Omega U^*[H^*,\lambda]U^{\mathrm{T}}|k\rangle\langle k|U[H,\lambda]U^\dagger\Omega^* - \Omega U^*[H^*,\lambda]U^{\mathrm{T}}|l\rangle} \\ = {} & -2N\tau x_l + 2\tau q\delta_{l\bar{l}} + 2\tau(1 - x_l) \\ & -4\tau{\sum_k}'\frac{x_l x_k - \delta_{l\bar{l}}\delta_{k\bar{k}} - \delta_{k\bar{l}}(x_l + x_{\bar{l}})/2 + x_l x_k\delta_{lk}}{x_l - x_k},\end{aligned} \tag{4.39}$$

where the δ_{lk} term can be dropped because of the constraint $k \neq l$ on the sum. Note how Q changes to $q = |Q|$ because of the sign of the matrix element involving pinned eigenvalues.

Again we find that eigenvalues at unity remain pinned. For the other eigenvalues, we separate out from the sum the q eigenvalues that are pinned, and sum over the $M = (N - q)/2$ pairs of unpinned eigenvalues,

$$\begin{aligned}\overline{\delta x_l} = {} & -2N\tau x_l + 2\tau(1 - x_l) - 2\tau\frac{2 - (x_l + x_{\bar{l}})}{x_l - x_{\bar{l}}} \\ & - 4\tau q\frac{x_l}{x_l - 1} - 4\tau x_l{\sum_k}''\frac{x_k + x_{\bar{k}} - 2x_{\bar{l}}}{x_l + x_{\bar{l}} - x_k - x_{\bar{k}}},\end{aligned} \tag{4.40}$$

where the double-prime again indicates the exclusion of the pinned eigenvalues. Furthermore,

$$\overline{\delta x_l\delta x_m} = 8\tau(\delta_{l\bar{m}} - \delta_{lm}x_l^2). \tag{4.41}$$

For the quantities $\mu_l = (x_l + x_{\bar{l}})/2$, this gives

$$\overline{\delta\mu_l} = -2q\tau(\mu_l + 1) + 2\tau(1 - 3\mu_l) - 4\tau{\sum_k}'' \frac{\mu_l^2 - 1}{\mu_l - \mu_k}, \tag{4.42}$$

$$\overline{\delta\mu_l \delta\mu_m} = 8\tau(1 - \mu_l^2)\delta_{lm}. \tag{4.43}$$

The stationarity condition (4.31) is now fulfilled for

$$P(\mu_1, \mu_2, \ldots \mu_M) \propto \prod_{k=1}^{M} (1 - \mu_k)^{(q-1)/2} \prod_{l<m=1}^{M} |\mu_l - \mu_m|, \tag{4.44}$$

which gives the joint probability distribution of the twofold degenerate, unpinned eigenvalues μ_n ($n = 1, 2, \ldots M$).

Eigenvalue density

The probability distributions (4.32) and (4.44) are both of the form

$$P(\mu_1, \mu_2, \ldots \mu_M) \propto \prod_{k=1}^{M} (1 + \mu_k)^a (1 - \mu_k)^b \prod_{l<m=1}^{M} |\mu_l - \mu_m|^\beta, \tag{4.45}$$

with $\beta = 2$, $a = 1/2$, $b = |Q| - 1/2$ in class D and $\beta = 1$, $a = 0$, $b = |Q|/2 - 1/2$ in class BDI. These are called Jacobi distributions, because the eigenvalue density $\rho(\mu)$ can be written in terms of Jacobi polynomials [41].

For small N it is quicker to calculate the eigenvalues density by integrating out all μ_n's except a single one. Keep in mind that $|Q|$ of the μ_n's are pinned at unity, and that the $N - |Q| = 2M$ unpinned μ_n's are twofold degenerate. (The products in Eq. (4.45) run only over these M unpinned pairs.) The eigenvalue density $\rho(\mu) = \langle \sum_{n=1}^{N} \delta(\mu - \mu_n) \rangle$ is then given by

$$\begin{aligned} \rho(\mu) &= |Q|\delta(\mu - 1) + 2Mp(\mu), \\ p(\mu) &= \int_{-1}^{1} d\mu_1 \int_{-1}^{1} d\mu_2 \\ &\quad \cdots \int_{-1}^{1} d\mu_M \, \delta(\mu - \mu_1) P(\mu_1, \mu_2, \ldots \mu_M). \end{aligned} \tag{4.46}$$

The delta functions satisfy $\int_{-1}^{1} \delta(\mu \pm 1) d\mu = 1$. The average conductance follows from the eigenvalue density according to Eq. (4.9),

$$\langle G \rangle = T^2 G_0 \int_{-1}^{1} d\mu\, \rho(\mu) [1 + (1-T)^2 - 2(1-T)\mu]^{-1}. \tag{4.47}$$

This gives the small-N results in Eq. (4.11) and Fig. 4.2.

The large-N limit (4.14) is obtained from an integral equation for the eigenvalue density in the Jacobi ensemble [5, 44],

$$\begin{aligned} M \int_{-1}^{1} d\mu\, p(\mu') \ln|\mu - \mu'| &= -\tfrac{1}{2}(1 - 2/\beta) \ln p(\mu) \\ &\quad - \frac{a}{\beta} \ln(1+\mu) - \frac{b}{\beta} \ln(1-\mu) + C + \mathcal{O}(1/M). \end{aligned} \tag{4.48}$$

The constant C is determined by the normalization

$$\int_{-1}^{1} d\mu\, p(\mu) = 1. \tag{4.49}$$

The solution is

$$\begin{aligned} M p(\mu) &= \frac{\tilde{M}}{\pi \sqrt{1-\mu^2}} - \frac{a}{\beta} \delta(\mu+1) - \frac{b}{\beta} \delta(\mu-1) \\ &\quad + \tfrac{1}{4}(1 - 2/\beta)[\delta(\mu+1) + \delta(\mu-1)] + \mathcal{O}(1/M), \end{aligned} \tag{4.50}$$

$$\tilde{M} = M + (a+b)/\beta - \tfrac{1}{2}(1 - 2/\beta). \tag{4.51}$$

Upon substitution of the values for a, b, β in the two symmetry classes, and transforming back from p to ρ, we find

$$\rho(\mu) = \frac{N}{\pi} \frac{1}{\sqrt{1-\mu^2}} + \tfrac{1}{2}\delta(\mu-1) - \tfrac{1}{2}\delta(\mu+1) + \mathcal{O}(1/M), \tag{4.52}$$

independent of Q and for both symmetry classes D and BDI. The corresponding result for the conductance is Eq. (4.14), to order $1/N$ if the limit $N \to \infty$ is taken at fixed Q.

Large-voltage limit

For completeness we also give the derivation of the large-voltage limit (4.10) of the average conductance. We need to evaluate

$$\langle \tilde{G} \rangle = T^2 G_0 \int_0^{2\pi} d\phi\, \tilde{\rho}(\phi) \left| 1 - (1-T) e^{i\phi} \right|^{-2}, \tag{4.53}$$

with $\tilde{\rho}(\phi) = \langle \sum_n \delta(\phi - \phi_n) \rangle$ the density on the unit circle of the eigenvalues $e^{i\phi_n}$ of a unitary matrix $\tilde{\Omega}$.

In class D the matrix $\tilde{\Omega} \equiv U$ is uniformly distributed in $\mathcal{U}(N)$. This is the circular unitary ensemble (CUE, $\beta = 2$). In class BDI the chiral symmetry enforces that $\tilde{\Omega}$ is unitary symmetric, $\tilde{\Omega} = UU^{\mathrm{T}}$ with U uniform in $\mathcal{U}(N)$. This is the circular orthogonal ensemble (COE, $\beta = 1$). Unlike the probability distributions we needed for the zero-voltage limit, these two distributions are in the literature [41],

$$P(\phi_1, \phi_2, \ldots \phi_N) \propto \prod_{k<l=1}^{N} |e^{i\phi_k} - e^{i\phi_l}|^\beta. \tag{4.54}$$

The corresponding density

$$\tilde{\rho}(\phi) = N/2\pi, \quad 0 < \phi \leq 2\pi, \tag{4.55}$$

is uniform irrespective of the value of β and without any finite-N corrections. Substitution into Eq. (4.53) gives the result (4.10).

Bibliography

[1] G. Bergmann, Phys. Rep. **107**, 1 (1984).

[2] P. A. Lee and T. V. Ramakrishnan, Rev. Mod. Phys. **57**, 287 (1985).

[3] P. W. Brouwer and C. W. J. Beenakker, Phys. Rev. B **52**, 3868 (1995).

[4] A. Altland and M. R. Zirnbauer, Phys. Rev. Lett. **76**, 3420 (1996).

[5] C. W. J. Beenakker, Rev. Mod. Phys. **69**, 731 (1997).

[6] R. M. Lutchyn, J. D. Sau, and S. Das Sarma, Phys. Rev. Lett. **105**, 077001 (2010).

[7] Y. Oreg, G. Refael, and F. von Oppen, Phys. Rev. Lett. **105**, 177002 (2010).

[8] Two reviews of the search for Majorana fermions in superconductors are: J. Alicea, Rep. Prog. Phys. **75**, 076501 (2012); C. W. J. Beenakker, Annu. Rev. Con. Mat. Phys. **4**, 113 (2013).

[9] K. T. Law, P. A. Lee, and T. K. Ng, Phys. Rev. Lett. **103**, 237001 (2009).

[10] V. Mourik, K. Zuo, S. M. Frolov, S. R. Plissard, E. P. A. M. Bakkers, and L. P. Kouwenhoven, Science **336**, 1003 (2012).

[11] M. T. Deng, C. L. Yu, G. Y. Huang, M. Larsson, P. Caroff, and H. Q. Xu, Nano Lett. **12**, 6414 (2012).

[12] A. Das, Y. Ronen, Y. Most, Y. Oreg, M. Heiblum, and H. Shtrikman, Nature Physics **8**, 887 (2012).

[13] R. M. Wilson, Physics Today **65** (6), 14 (2012).

[14] K. Flensberg, Phys. Rev. B **82**, 180516(R) (2010).

[15] G. Kells, D. Meidan, and P. W. Brouwer, Phys. Rev. B **85**, 060507(R) (2012).

[16] S. Tewari, T. D. Stanescu, J. D. Sau, and S. Das Sarma, Phys. Rev. B **86**, 024504 (2012).

[17] F. Pientka, G. Kells, A. Romito, P. W. Brouwer, and F. von Oppen, Phys. Rev. Lett. **109**, 227006 (2012).

[18] J. Liu, A. C. Potter, K. T. Law, and P. A. Lee, Phys. Rev. Lett. **109**, 267002 (2012).

[19] K. Slevin, J.-L. Pichard, and P. A. Mello, J. Phys. I France **6**, 529 (1996).

[20] A. Altland and M. R. Zirnbauer, Phys. Rev. B **55**, 1142 (1997).

[21] S. Rodríguez-Pérez, G. C. Duarte-Filho, and A. M. S. Macêdo, Phys. Rev. B **82**, 115453 (2010).

[22] D. A. Ivanov, J. Math. Phys. **43**, 126 (2002).

[23] P. A. Ioselevich, P. M. Ostrovsky, and M. V. Feigel'man, Phys. Rev. B **86**, 035441 (2012).

[24] D. Bagrets and A. Altland, Phys. Rev. Lett. **109**, 227005 (2012).

[25] S. Ryu, A. Schnyder, A. Furusaki, and A. Ludwig, New J. Phys. **12**, 065010 (2010).

[26] S. Tewari and J. D. Sau, Phys. Rev. Lett. **109**, 150408 (2012).

[27] Chiral symmetry of the Hamiltonian is expressed by $H \mapsto -H$ upon exchange $e \leftrightarrow h$ of the electron and hole degrees of freedom. It is broken by spin-orbit coupling of transverse momentum, unlike the more fundamental particle-hole symmetry $H \mapsto -H^*$.

[28] C. W. J. Beenakker, J. P. Dahlhaus, M. Wimmer, and A. R. Akhmerov, Phys. Rev. B **83**, 085413 (2011).

[29] M. Diez, J. P. Dahlhaus, M. Wimmer, and C. W. J. Beenakker, Phys. Rev. B **86**, 094501 (2012).

[30] B. Béri, Phys. Rev. B **79**, 245315 (2009). The Béri degeneracy of the Andreev reflection eigenvalues $\rho_m \neq 0, 1$ is a consequence of particle-hole symmetry, which is an anti-unitary symmetry that squares to $+1$. This distinguishes it from the more familiar Kramers degeneracy, resulting from an anti-unitary symmetry that squares to -1. For a self-contained proof of Béri degeneracy, see App. B of arXiv:1101.5795.

[31] R. S. Whitney and Ph. Jacquod, Phys. Rev. Lett. **103**, 247002 (2009).

[32] Th. Engl, J. Kuipers, and K. Richter, Phys. Rev. B **83**, 205414 (2011).

[33] A. R. Akhmerov, J. P. Dahlhaus, F. Hassler, M. Wimmer, and C. W. J. Beenakker, Phys. Rev. Lett. **106**, 057001 (2011)

[34] For the parallel magnetic fields in Figs. 4.3 and 4.4 we find that $Q = \frac{1}{2}(1 - \mathrm{Det}\, r)$ switches from 0 to 1 at $E_Z = 8.1\, E_{so}$ and then back to 0 at $E_Z = 11.3\, E_{so}$, with a re-entrant $Q = 0$ interval $9.2\, E_{so} < E_Z < 9.7\, E_{so}$.

[35] The parameters for the simulations shown in Figs. 4.3 and 4.4 are, in panel a): $x_{\mathrm{barrier}} = 23\, l_{so}$, $\delta L_{\mathrm{barrier}} = 4a = 0.4\, l_{so}$, $U_{\mathrm{disorder}} = 12.5\, E_{so}$, $U_{\mathrm{barrier}} = 15\, E_{so}$, $G_{\mathrm{disorder}} = 2.7\, e^2/h$, $G_{\mathrm{barrier}} = 1.8\, e^2/h$; in panel b): $x_{\mathrm{barrier}} = 3\, l_{so}$, $\delta L_{\mathrm{barrier}} = a = 0.1\, l_{so}$, $U_{\mathrm{disorder}} = 20\, E_{so}$, $U_{\mathrm{barrier}} = 50\, E_{so}$, $G_{\mathrm{disorder}} = 2.9\, e^2/h$, $G_{\mathrm{barrier}} = 3.2\, e^2/h$.

[36] Fig. 4.3 shows that the $Q = 1$ peak becomes narrower than the $Q = 0$ peak when the length of the disordered region between tunnel barrier and NS interface is reduced. This is consistent with the findings of Ref. 17 for the effect of disorder on the Majorana resonance.

[37] The appearance and disappearance of the zero-voltage conductance peak in Fig. 4.4 is associated with a merging and splitting of two peaks at $\pm V_0$. We understand this as a collision of two poles of the scattering matrix at complex energy $i\varepsilon \pm V_0$, as described by D. I. Pikulin and Yu. V. Nazarov, JETP Lett. **94**, 693 (2011).

[38] The parameters for the simulations shown in Fig. 4.5 are: $W = 0.3\, l_{so}$, $x_{\mathrm{barrier}} = 2.7\, l_{so}$, $\delta L_{\mathrm{barrier}} = a = 0.01\, l_{so}$, $E_F = 1000\, E_{so}$, $\Delta_0 = 100\, E_{so}$, $U_{\mathrm{disorder}} = 4000\, E_{so}$, $U_{\mathrm{barrier}} = 7000\, E_{so}$, corresponding to $N = 8$, $G_{\mathrm{disorder}} = 1.3\, e^2/h$, $G_{\mathrm{barrier}} = 1.5\, e^2/h$.

[39] M. Wimmer, A. R. Akhmerov, J. P. Dahlhaus, and C. W. J. Beenakker, New J. Phys. **13**, 053016 (2011).

[40] The parameters for the simulations shown in Fig. 4.7 are: $W = 0.3\,l_{\mathrm{so}}$, $x_{\mathrm{barrier}} = 1.1\,l_{\mathrm{so}}$, $\delta L_{\mathrm{barrier}} = a = 0.01\,l_{\mathrm{so}}$, $E_{\mathrm{F}} = 200\,E_{\mathrm{so}}$, $\Delta_0 = 100\,E_{\mathrm{so}}$, $E_{\mathrm{Z}} = 60\,E_{\mathrm{so}}$, $U_{\mathrm{disorder}} = 500\,E_{\mathrm{so}}$, $U_{\mathrm{barrier}} = 2000\,E_{\mathrm{so}}$, corresponding to $N = 2$, $G_{\mathrm{disorder}} = 1.5\,e^2/h$, $G_{\mathrm{barrier}} = 0.85\,e^2/h$.

[41] P. J. Forrester, *Log-Gases and Random Matrices* (Princeton University Press, 2010).

[42] F. J. Dyson, J. Math. Phys. **3**, 1191 (1962).

[43] V. L. Girko, Ukr. Mat. Zh. **37**, 568 (1985) [English translation: Ukr. Math. J. **37**, 457 (1985)].

[44] F. J. Dyson, J. Math. Phys. **13**, 90 (1972).

Chapter 5

Phenomenology and dynamics of Majorana Josephson junction

5.1 Introduction

Recently, the proposals of solid-state realizations of Majorana fermions came into focus of attention. While the first proposal [1] concerned non-Abelian excitations in 5/2 FQHE in semiconductor heterostructures, most proposals [2, 3] exploited exotic superconductors where Majorana fermions correspond to zero-energy states of an effective BdG Hamiltonian. The Majorana states are instrumental for realization of topological quantum computation [4]. More recent contributions [5] utilize the proximity effect from a conventional superconductor, either in nanowires in a strong magnetic field and with strong spin-orbit interaction [6–8], or in topological insulators [9, 10]. This brings the Majoranas close to experimental realization, and underlines the importance of reliable experimental signatures of their presence. Among the signatures are half-integer conductance quantization [11] and 4π Josephson effect in superconductor-superconductor (SS) junctions [12, 7, 13].

No 4π periodicity is to be seen in the stationary ground state of the junction It can only be observed [14, 15] in dynamics induced, for instance, by a d.c. voltage bias. Unambiguous signature of this 4π periodicity is the current noise peak at half of the Josephson frequency $\omega_j = 2eV/\hbar$ [14].The avoided crossing of Andreev states is intrinsic for

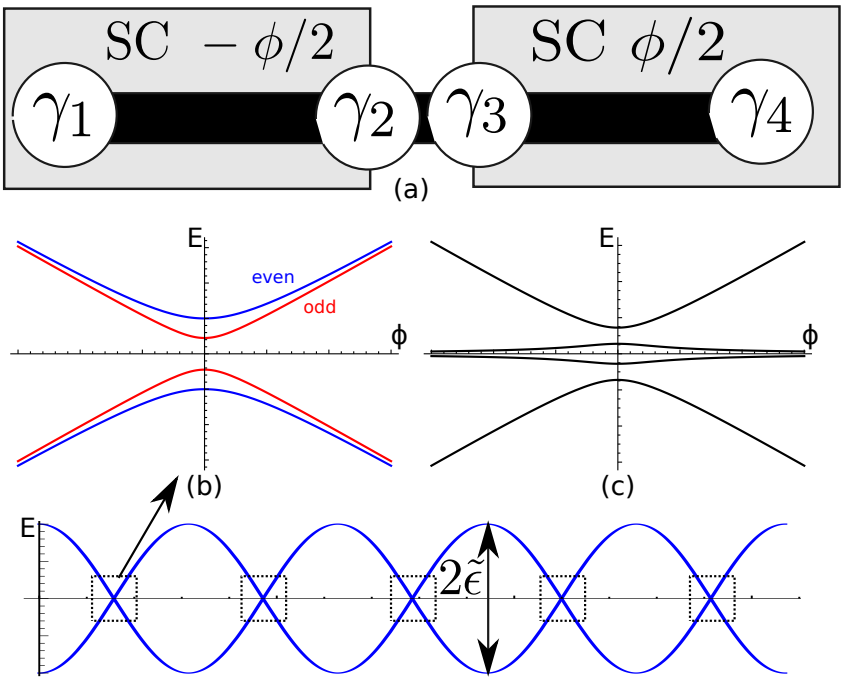

Figure 5.1. a. A Majorana Josephson junction is formed by mounting a nanowire (black) on two superconducting leads (grey) resulting in four Majoranas γ_{1-4}. b. The energies of the many-body junction states versus phase near an avoided crossing point. c. Corresponding Andreev levels. d. The energies of the junction states versus phase at a bigger scale. Far from the avoided crossing points, the energies of even and odd states are indistinguishably close. This corresponds to two zero-energy Andreev levels.

finite systems and restores the 2π periodicity of the junction ground state [16, 2, 12]. This has been recently confirmed by detailed calculations of the Andreev spectrum of the nanowire-based SS junctions [17].

In this chapter, we put forward a generic phenomenological model of a Majorana Josephson junction and demonstrate that the dynamics in the junction are substantially richer than thought. In particular, the sharp peaks in noise spectrum of a voltage-biased junction are not generally confined to any definite fraction of ω_j: one can talk of $any - \pi$ Josephson effect in this context. Experimental observation of these singularities would give a robust proof of the existence of Majoranas and open up the

possibilities for quantum manipulation of these states. Our treatment of dynamics encompasses the Landau-Zener tunneling at the avoided crossings, decoherence, relaxation, and quasiparticle poisoning.

5.2 Setup and the phenomenological Hamiltonian

We exemplify with a nanowire setup (Fig. 5.1) although the same phenomenology extends to topological insulators. A nanowire mounted on a single superconducting lead develops a topologically non-trivial state in a parameter range of magnetic fields and gate voltages [7]. Two Majorana states emerge at the wire ends. Majorana Josephson junction is formed by mounting the wire on two leads biased with superconducting phase difference ϕ. Two extra Majorana states $\gamma_{2,3}$ emerge at the junction, in addition to the end states $\gamma_{1,4}$. The overlap between γ_2 and γ_3 is strong but does depend on phase and vanishes at a certain ϕ_0. If one disregards the end states [12, 7, 13], the resulting energies are 4π periodic in ϕ and the resulting states are of indefinite parity. We exemplify this dependence with $E(\phi) = \pm\tilde{\epsilon}\sin(\frac{\phi-\phi_0}{2})$, $\tilde{\epsilon}$ being a typical coupling energy of $\gamma_{2,3}$. To fix the parity, it is paramount to bring the end states to the picture. We developed [16] a scattering matrix theory where the 2π periodicity is proven from the topological properties of the scattering matrix. In a nutshell, the crossing of Andreev levels is avoided. We need a practical Hamiltonian to describe the details of the situation in the vicinity of ϕ_0. That can be rigorously derived from the scattering approach, yet we opt here for a simple heuristic deviation in terms of overlaps of Majorana states.

These overlaps are exponentially small for long wires, $\propto \exp(-L/2\xi)$, L being the wire length, the localization length ξ being of the order of the spin-orbit length L_{so}. For InAs wires [18], $L_{so} = 0.2\mu m$, and L would not exceed $2\mu m$ since inevitable disorder forbids topological state for longer wires. This sets the biggest exponential suppression to $\simeq 10^{-2}$. Owing to the exponential suppression, the direct overlap t_{14} between the end states is much smaller than the overlaps between the end and the junction states, and can be disregarded. This brings us to the following Hamiltonian:

$$\hat{H} = i\tilde{\epsilon}(\phi - \phi_0)\hat{\gamma}_2\hat{\gamma}_3 + i(t_{12}\hat{\gamma}_2 + t_{13}\hat{\gamma}_3)\hat{\gamma}_1 + i(t_{42}\hat{\gamma}_2 + t_{43}\hat{\gamma}_3)\hat{\gamma}_4. \quad (5.1)$$

that is valid in the vicinity of the crossing point and provides a generic phenomenological model of a Majorana Josephson junction. Here, the overlaps t are real, and $\hat{\gamma}_{1-4}$ are self-conjugated anticommuting Majorana operators [19]. We present a detailed derivation of the Hamiltonian (5.1) in [20].

It is instructive to give the eigenenergies of the full many-body states of the Hamiltonian, rather than the associated Andreev levels. The energies of these states are sums over the energies of the Andreev levels with taking the filling of the levels into account. The Hamiltonian conserves the parity of the particle number and therefore gives rise to eigenstates with either odd or even number of particles. There are two eigenvalues of opposite sign for each parity,

$$E_{\pm,\mathrm{o,e}} = \pm\sqrt{G_{\mathrm{o,e}}^2 + \frac{\tilde{\epsilon}^2}{4}(\phi-\phi_0)^2}, \tag{5.2}$$

where

$$G_{o,e} = \tfrac{1}{2}\sqrt{(t_{12}\pm t_{43})^2 + (t_{13}\mp t_{42})^2} \tag{5.3}$$

and $\pm$ sign is chosen such that $G_e > G_o$. Their phase dependence (Fig. 5.1b)gives a familiar glimpse of avoided level-crossing hyperbolas, $G_{\mathrm{o,e}}$ being the minimum energy splittings of odd/even states, respectively (when the difference between even and odd cases is insignificant, we will denote both values G). The two positive energies of the associated Andreev levels are given by $E_{1,2} = |E_{\mathrm{e}}| \pm |E_{\mathrm{o}}|$ (Fig.5.1c). This characteristic form is conformed by the numerical calculations based on microscopic models [16, 17] proving the validity of the Hamiltonian (5.1). The absence of the direct overlap t_{14} leads to a special property: the phase-dependent term describing the overlap of $\hat{\gamma}_2$, $\hat{\gamma}_3$ anticommutes with the rest of the terms. This guarantees the energies to be even in phase and to merge far from $\phi = \phi_0$, these properties would be absent for a most general four-Majorana Hamiltonian.

5.3 Dynamics of the voltage-biased system

Let us notice that the junction in either odd or even state is nothing but a qubit that is similar to other superconducting qubits that commonly

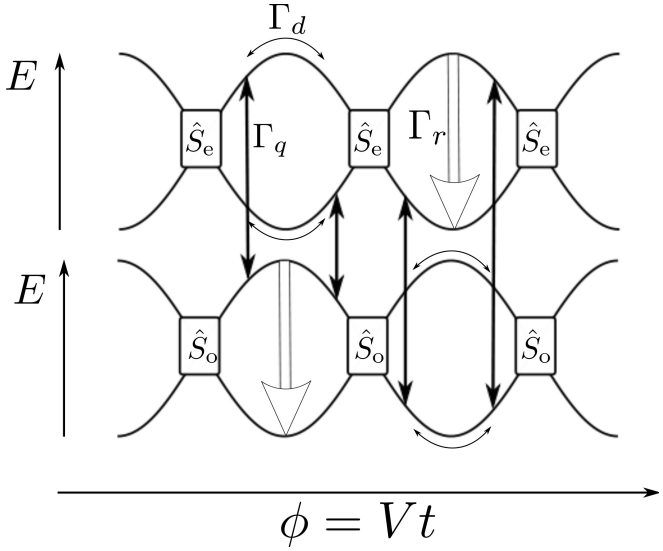

Figure 5.2. Processes affecting the junction dynamics. In between the parity-dependent Landau-Zener scatterings (described by 2×2 matrices $\hat{S}_{\mathrm{o,e}}$) the junction is subject to dephasing (with a rate Γ_d), relaxation (Γ_r) and quasiparticle poisoning (Γ_q).

exploit avoided level crossing [21–23]. One can employ quantum manipulation of the resulting Majorana states by changing the superconducting phase in time. For instance, following [21], one can prepare the qubit in the ground state reasonably far from the crossing point $\phi = \phi_1$, and give a pulse that brings the junction to $\phi = \phi_0$. This will cause Rabi oscillations with frequency $2G/\hbar$ that can be detected by measuring the probabilities to find the qubit in the ground or excited state after the pulse as functions of pulse duration.

Here we restrict ourselves to the case of immediate experimental relevance where the junction is biased by a d.c. voltage V so that the phase ϕ is swept linearly with time, $\dot{\phi} = 2eV/\hbar$. In a usual Josephson junction where the energy levels are 2π periodic, such bias results in coherent oscillations of the supercurrent $I(\phi) = 2e/\hbar \partial E(\phi)/\partial\phi$ with Josephson frequency $\omega_j = 2eV/\hbar$ [25]. The idea behind the 4π Josephson effect [26] is an apparent 4π periodicity of energy levels in the limit of vanishing G, this suggests the oscillations at a half of Josephson frequency, $I(t) = \pm I_\mathrm{m} \cos(\omega_j t/2)$, $I_\mathrm{m} \equiv e\tilde{\epsilon}/\hbar$. Albeit these oscillations cannot be coherent owing to random switching between the two branches $\pm$ of

the energy spectrum. The signature of 4π periodicity is rather a sharp peak in the spectral density of the current *noise* [14], with the width of order of switching rate, and integrated intensity being given by $I_{\mathrm{m}}^2/2$, the average square of the current. For this simplified picture to hold, one should require sufficiently small voltages, $V \ll \tilde{\epsilon}$. Failure to satisfy this condition results in proliferation to higher energy levels and finally to continuous spectrum, this increasing the peak width to the values of the order of Δ and thus rendering noise peaks undetectable. [14, 17]

In this chapter, we address the noise in Majorana Josephson junctions at smaller voltages. Evidently, the avoided level crossing results in usual Josephson effect in the limit $V \to 0$. The complex and interesting crossover between 2π and 4π regimes involves Landau-Zener (LZ) tunnelling upon crossing a point $\phi = \phi_0 + 2\pi n$ in the vicinity of the point. The parity obviously does not change, and for each parity we have a classic setup of LZ tunnelling [24] between two levels. The values of the qubit wave function before and after LZ scattering are related by a 2×2 unitary matrix:

$$\hat{S}_{o,e} = \begin{pmatrix} \sqrt{1 - P_{o,e}} & -e^{i\chi}\sqrt{P_{o,e}} \\ e^{-i\chi}\sqrt{P_{o,e}} & \sqrt{1 - P_{o,e}} \end{pmatrix}, \tag{5.4}$$

where the probability of LZ tunnelling is given by

$$P_{o,e} = \exp\left(-\frac{4\pi}{eV}\frac{G_{o,e}^2}{\tilde{\epsilon}}\right). \tag{5.5}$$

This suggests an importance of a voltage scale $eV_0 \equiv 4\pi G^2/\tilde{\epsilon} \ll \tilde{\epsilon}$ at which the probabilities are of the order of 1 and the crossover between 2π and 4π regimes is expected. We stress that the probabilities are generally different for odd and even states that permits the identification of these states that are hardly distinguishable otherwise.

The quantum dynamics are affected by the processes of relaxation, dephasing and quasiparticle poisoning (Fig.5.2) that occur throughout the time-line with no peculiarities near the crossing points. We assume low temperature $k_B T \ll \tilde{\epsilon}$, so that the relaxation is always from higher to lower energy state with the rate $\Gamma_r(\phi)$. The decoherence suppresses the non-diagonal elements of the density matrix (with the rate $\Gamma_d(\phi)$) not affecting the diagonal ones. We assume the fluctuation of the phase ϕ to be the main source of the decoherence, in this case $\Gamma_d(\phi) \propto I^2(\phi)$.

The quasiparticle transfer processes account for a parity change. They may be due to stray quasiparticles in the bulk superconductor that come to the junction with the energies of the order of the superconducting energy gap $\Delta > \tilde{\epsilon}$ and lose this energy either adding or annihilating a quasiparticle in Andreev levels under consideration. Due to significant initial quasiparticle energy, the probabilities to find the junction in either upper or lower state after a quasiparticle transfer, are the same. The quasiparticle rate Γ_q does not depend on the phase ϕ.

This results in the straightforward but lengthy equation for the density matrices $\hat{\rho}_{o,d}$ to be found in [20]. We solve this equation with continuity conditions $\hat{\rho}_{o,d}(t_{ac}+0) = \hat{S}_{o,d}\hat{\rho}_{o,d}(t_{ac}-0)\hat{S}_{o,d}^{-1}$, t_{ac} corresponding to time moments of the crossings, and compute the correlator of current operators

$$S(\omega) = \int_{-\infty}^{\infty} dt_1 \int_0^{\frac{2\pi}{\omega_j}} dt_2 e^{i\omega(t_1-t_2)} \langle\langle I(t_1)I(t_2)\rangle\rangle. \tag{5.6}$$

that gives the spectral density of the current noise. We concentrate on two limiting cases of fast (Fig. 5.3) and slow (Fig. 5.4)decoherence. In both cases, we assume slow relaxation and poisoning, $\omega_j \gg \Gamma_r, \Gamma_q$.

5.3.1 Fast decoherence

"Fast" implies the quantum coherence is lost during a period of the Josephson oscillations, $\Gamma_d \gg \omega_j$, and the equation for density matrix reduces to a master equation. Fig. 5.3a shows the spectral density for equal LZ probability for even and odd states, $G_e \approx G_o$. The voltage growth from the lowermost to upper curve resulting in increased P_{LZ}. At low voltage ($P_{LZ} \ll 0$, the noise peaks at ω_j as well as at its multiples, the latter manifesting non-sinusoidal $I(\phi)$. This proves a usual periodicity. At higher voltage where $P_{LZ} \approx 1$ we see a single peak at $\omega_j/2$ manifesting 4π periodicity. In both limiting cases, the peak widths $\simeq \Gamma_{r,qp}$. Important feature is the absence of any distinguishable peaks at intermediate P_{LZ}. The reason is the LZ tunneling causing incoherent switching at almost any crossing point. The peaks acquire width $\simeq \omega_j \gg \Gamma_{r,qp}$ and correspondingly reduce their height to the background level.

In Fig. 5.3b the LZ probabilities are very different at the crossover corresponding to $G_e/G_o = 4$. Now one can distinguish the peaks at both $\omega_j/2$ and ω_j in the crossover region, though they are reduced in

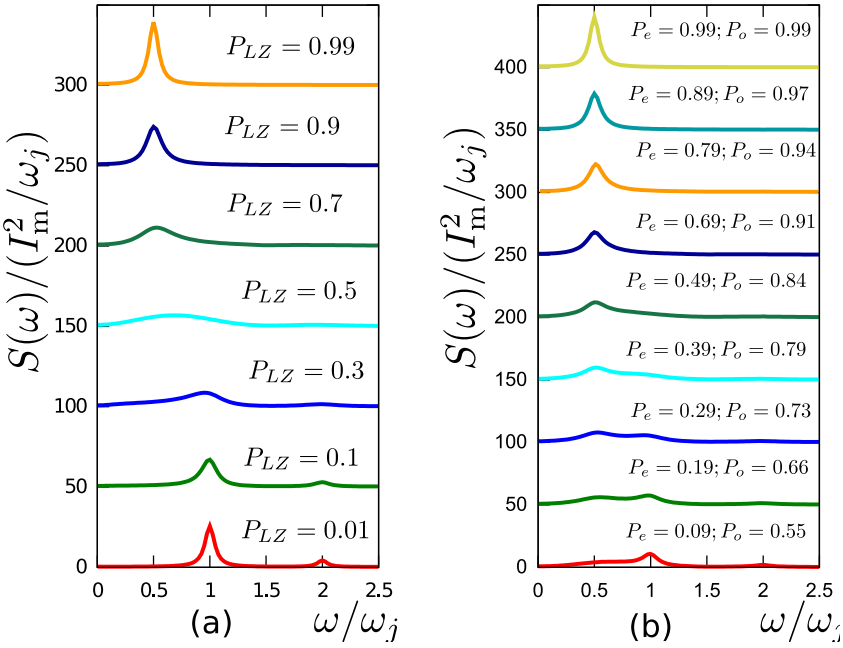

Figure 5.3. The spectral intensity $S(\omega)$ of the current noise for a set of V corresponding to LZ probabilities shown, in the limit of fast decoherence. a. Indistinguishable parities $P_e = P_o = P_{LZ}$; b. $P_e \neq P_o$ ($G_e = 4G_o$). Distinct peaks at multiples of ω_j at $P \ll 1$ transmute into a single peak at $\omega_j/2$ at $P \approx 1$. ($\Gamma_r = \Gamma_q = 0.02\omega_j$ for all plots).

height in comparison with the limiting cases. The explanation is the parity separation in time domain. Since $\Gamma_q \ll \omega_j$, the parity persist over many periods between the random switches. While the junction is in even parity state, $P_{LZ} \approx 1$, and during this time interval the noise at $\omega_j/2$ is generated. While the junction is in odd parity state, almost no LZ tunnelling takes place, and the noise is generated at Josephson frequency. The experimental observation of two peaks would thus prove the parity effect. One can also think of a more challenging observation where the noise can be resolved fast, that is, at a time-scale $< \Gamma_q^{-1}$. Such noise measurement will monitor the parity of the junction in real time.

5.3.2 Slow decoherence

The results in the opposite limit of slow decoherence $\Gamma_d \ll \omega_j$ are decisively more complex and intriguing (Fig. 5.4). In this limit, the dynamics are truly quantum over many periods. An analytical analysis gives the positions of the noise peaks as well as the integrated noise intensities around each peak [20]. Most striking feature is an oscillatory dependence of the peak intensities and positions on voltage. This is a manifestation of quantum interference between the subsequent LZ tunnelling events not suppressed by decoherence. Similar interference patterns have been predicted and observed for superconducting qubits in [27, 23]. We have found that a voltage-biased Majorana Josephson junction presents the simplest and most striking framework for this interference effect.

The quantum phase θ accumulated between the subsequent crossing points is estimated as

$$\theta = \int\limits_{\text{period}} dt \frac{\Delta E(\phi(t))}{\hbar} = \frac{8\tilde{\epsilon}}{\hbar\omega_j}, \tag{5.7}$$

where $\Delta E(\phi)$ is the energy difference between levels of the same parity. The phase is big on the scale $eV/\tilde{\epsilon}$, its increment by 2π gives an estimate of the oscillation period in voltage $\Delta V = (\pi/8)V(eV/\tilde{\epsilon}) \ll V$.

Importantly, the frequency positions of the additional noise peaks (Fig. 5.4a), those the main Josephson peaks at multiples of ω_j, are not at any integer fractions of ω_j. In the context, we can dub this any-π Josephson effect. It stems from a quasi-energy splitting in a periodically driven qubit. At $V \gg V_0$, additional peaks converge at $(2n+1)\omega_j/2$

oscillation around this frequency. The spread of these oscillations $\Delta\omega$ does not vanish with increasing V: rather, it increases following $\Delta\omega \simeq (2e/\hbar)\sqrt{VV_0}$. This proves that any-$\pi$ Josephson effect can be observed at voltages $V \gg V_0$ far beyond the crossover region. The width of the peaks is determined by Γ_d. From this, we estimate the minimum decoherence rate permitting the resolution of the peaks: $\Gamma_d \simeq (e/\hbar)\sqrt{VV_0}$. For the sake of simple drawing, we assumed indistinguishable parities such that $P_\mathrm{o} = P_\mathrm{e}$. If $P_\mathrm{o} \neq P_\mathrm{e}$, the additional peaks split once again corresponding to the two parities. [20]

At $V \ll V_0$, the noise intensity is mainly concentrated at a main peak at ω_j. In the opposite limit, the intensity concentrates at the peaks converging to $\omega_j/2$ retaining oscillating features even at high voltage. (Fig.5.4b,c)

5.4 Conclusion

To summarize, we have derived a generic phenomenological Hamiltonian to describe a Majorana Josephson junction with avoided Andreev level crossing, and investigated its quantum dynamics at constant voltage bias with emphasis on noise signatures of different, depending on the regime periodicity. This is the only robust transport signature of the Majorana Josephson junction. While in the fast decoherence regime the signatures follow an expected pattern, the interference of the subsequent LZ tunnelling events results in a complex any-π Josephson effect pattern in slow decoherence regime. The experimental observation of the effects predicted will provide unambiguous signature of Majorana states in Josephson junction and open up the perspectives of quantum manipulation and parity measurements in such junctions. One of the paths to observe the unusual periodicity is through measurement of Shapiro steps in voltage or current [28, 29] biased setups.

5.5 Appendix

5.5.1 Derivation of the phenomenological Hamiltonian

Here we present the derivation of the phenomenological Hamiltonian used in our article. We would like to keep this derivation as general as possible not relying on any concrete microscopic details. In this case, the

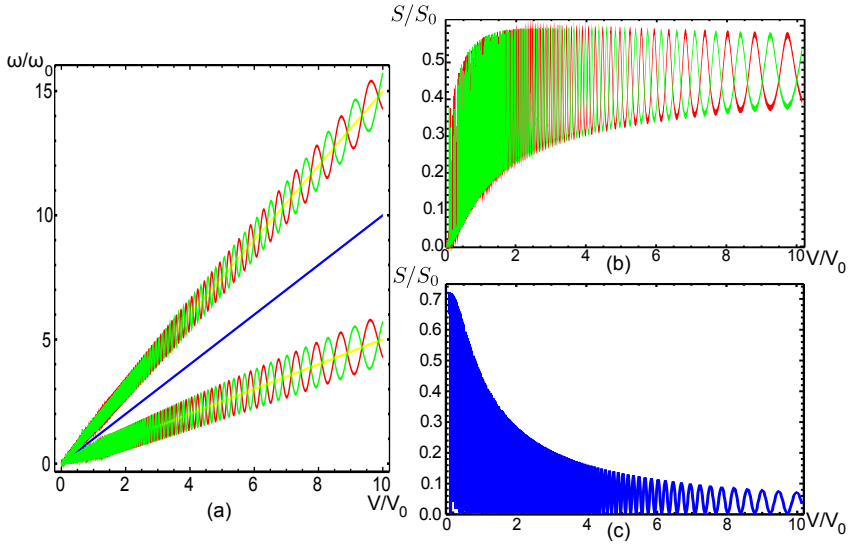

Figure 5.4. The slow decoherence limit. We chose $\tilde{\epsilon}/eV_0 = 30$ for all plots. (a). Frequency positions of the noise peaks versus V ($\omega_0 = (2e/\hbar)V_0$). The main ones are at $n\omega_j$ while the positions of additional peaks oscillate converging at $(n+1/2)\omega_j$. Only $n = 0, 1$ are shown. (b) Integrated noise intensity (in units of $S_0 \equiv I_m^2/2$) of the first two additional peaks. (c) The same for the $n = 1$ main peak.

method of choice is scattering theory. We take an arbitrary nanostructure connected to two superconducting leads and make a cut separating the structure onto two parts adjacent to corresponding leads. The scattering from the leads to/from the cut is characterized by corresponding energy-dependent scattering matrices $S_{1,2}$. Those are matrices in the space of the modes of the transversal quantization in the cut augmented with Nambu structure that we will be represented with Pauli matrices $\tau_{x,y,z}$. Owing to gauge invariance, the dependence of the scattering matrices on the superconducting phase ϕ of the corresponding lead is given by unitary transformation

$$S_{1,2}(\phi_{1,2}) = e^{i\frac{\phi_{1,2}}{2}\tau_y} S_{1,2}(0) e^{-i\frac{\phi_{1,2}}{2}\tau_y}. \tag{5.8}$$

The energies of Andreev bound states are then determined [30] from the equation

$$\det(1 - S_1 S_2) = 0, \tag{5.9}$$

that has solutions for a set of energies, those depending on the superconducting phase difference $\phi \equiv \phi_2 - \phi_1$ between the leads.

General topological properties of superconducting scattering matrices have been studied in [16]. In general case, only the intrinsic symmetry of the Bogolyubov-de Gennes representation presents a restriction on the matrices, $S(\varepsilon) = S^*(-\varepsilon)$. The presence of the topologically protected states at zero energy has been related to a special class of topologically non-trivial (TNT) matrices that have eigenvalues ± 1 at $\varepsilon = 0$. In [16], we have also presented solid topological arguments that prove that the pure TNT matrices cannot be realized in finite junctions. Rather, a matrix representative for Majorana states is topologically trivial yet is close to a TNT matrix at energies exceeding a small energy scale Γ. Following standard procedure due to Wigner, we implemented the decomposition of such matrices in terms of poles in complex energy plane. The simplest situation is achieved if a single pole at $\varepsilon = -i\Gamma$ is taken into account,

$$S = \left(1 - (1 - e^{i\alpha})|\Psi\rangle\langle\Psi|\right) S_0 \tag{5.10}$$

where S_0 is a TNT scattering matrix that can be expanded in energy around $\varepsilon = 0$ at energy scales $\gg \Gamma$, $e^{i\alpha} \equiv \frac{\varepsilon - i\Gamma}{\varepsilon + i\Gamma}$, $|\Psi\rangle$ being a normalized vector in the channel-Nambu space. Owing to BdG symmetry, this vector can be chosen real. The order of the factors in (5.10) is rather

arbitrary: one can shift the pole factor to the right modifying $|\Psi\rangle$ accordingly.

A physical picture behind the scattering matrix (5.10)is a pair of quasi-localized Majorana states. One of the states is localized close to the cut while another is buried in the setup somewhere in the superconducting lead. If we set a normal lead at another side of the cut, Γ is associated with escape time of this buried state to the lead, that can be quite low for a setup with well-protected topological properties. For the wire setup used for illustrations in the main text, the buried state corresponds to a Majorana at the far end of the wire. Any situation with a pair of Majoranas at a superconducting lead can be modelled in this way. If more Majoranas are buried in the structure, they would manifest themselves with more low-energy poles. We thus restrict ourselves to the simplest situation with a single relevant pair.

These considerations permit to model any Majorana Josephson junction with two single-pole scattering matrices,

$$S_1 = S_{10}\left(1-(1-e^{i\alpha_1})|\Psi_1\rangle\langle\Psi_1|\right); \tag{5.11}$$

$$S_2 = \left(1-(1-e^{i\alpha_2})|\Psi_2\rangle\langle\Psi_2|\right)S_{20}, \tag{5.12}$$

where $e^{i\alpha_j} = \frac{\varepsilon - i\Gamma_j}{\varepsilon + i\Gamma_j}$, $j = 1, 2$. We will show now that this model is equivalent to the phenomenological Hamiltonian used in the article.

To start with, let us note that Eq. 5.9 is equivalent to an eigenvector problem

$$\left(S_1^{-1} - S_2\right)|\Psi\rangle = 0, \tag{5.13}$$

for yet unknown $|\Psi\rangle$. We substitute $S_{1,2}$ in the form (5.12) to arrive at

$$(S_{10}^{-1} - S_{20})|\Psi\rangle + A|\Psi_1\rangle + B|\Psi_2\rangle = 0; \tag{5.14}$$

$$A = (e^{-i\alpha_1} - 1)\langle\Psi_1|S_{10}^{-1}|\Psi\rangle, \tag{5.15}$$

$$B = -(e^{i\alpha_2} - 1)\langle\Psi_2|S_{20}|\Psi\rangle. \tag{5.16}$$

We express $|\Psi\rangle$ from the first equation and substitute this to the second and third equations to obtain two consistency equations on A, B,

$$A = -(e^{-i\alpha_1} - 1)\langle\Psi_1|S_{10}^{-1}\frac{}{S_{10}^{-1} - S_{20}}|\left(A|\Psi_1\rangle + B|\Psi_2\rangle\right), \tag{5.17}$$

$$B = (e^{i\alpha_2} - 1)\langle\Psi_2|S_{20}\frac{}{S_{10}^{-1} - S_{20}}|\left(A|\Psi_1\rangle + B|\Psi_2\rangle\right). \tag{5.18}$$

To simplify the notations, we introduce a Hermitian matrix $h \equiv \frac{i}{2}\frac{S_{10}^{-1}+S_{20}}{S_{10}^{-1}-S_{20}}$ that depends on the TNT matrices only thus not involving the buried states. The consistency equations can be rewritten in terms of matrix elements of h, $h_{ij} \equiv \langle \Psi_i | h | \Psi_j \rangle$.

$$\varepsilon \begin{pmatrix} A \\ B \end{pmatrix} = -2 \begin{pmatrix} \Gamma_1 h_{11} & \Gamma_1 h_{12} \\ \Gamma_2 h_{21} & \Gamma_2 h_{22} \end{pmatrix} \begin{pmatrix} A \\ B \end{pmatrix}. \tag{5.19}$$

One can cast the equations to Hermitian form by rescaling $A \to A/\sqrt{\Gamma_2}$, $B \to B/\sqrt{\Gamma_1}$,

$$\varepsilon \begin{pmatrix} A \\ B \end{pmatrix} = -2 \begin{pmatrix} \Gamma_1 h_{11} & \sqrt{\Gamma_1\Gamma_2} h_{12} \\ \sqrt{\Gamma_1\Gamma_2} h_{21} & \Gamma_2 h_{22} \end{pmatrix} \begin{pmatrix} A \\ B \end{pmatrix}. \tag{5.20}$$

This would make a nice Hamiltonian if we can disregard the energy dependence of the matrix h at low energies. In fact, we cannot and have to take this one into account. To envisage the structure, let us comprehend the energy spectrum in the absence of the buried Majorana states, that is, disregarding the pole structure of $S_{1,2}$. In this case, the topological arguments [16] guarantee the double-degenerate state at zero energy at a certain value ϕ_0 of the phase difference. This implies that the equation for the spectrum,

$$(S_{10}^{-1} - S_{20})|\Xi\rangle = 0, \tag{5.21}$$

or its equivalent,

$$h^{-1}|\Xi\rangle = 0, \tag{5.22}$$

has a solution at zero energy at $\phi = \phi_0$ for two real eigenvectors $|\Xi_{1,2}\rangle$. By virtue of BdG condition, the matrix h^{-1} in real basis satisfies $h^{-1}(\epsilon) = -h^{-1}(-\epsilon)$ and can therefore be expanded in $\phi - \phi_0$,ε as follows

$$h^{-1} = \sum_{i=1,2} D_{ij}|\Xi_i\rangle\langle\Xi_j| + 2i\tilde{g}(\phi-\phi_0)(|\Xi_1\rangle\langle\Xi_2| - |\Xi_2\rangle\langle\Xi_1|) + (h^{(0)})^{-1}. \tag{5.23}$$

Here, D_{ij} is a symmetric positively defined 2×2 matrix, and $(h^{(0)})^{-1}$ is a non-singular part of h^{-1} on the space orthogonal to the vectors $|\Xi_{1,2}\rangle$. For this part, we can set $\epsilon = 0$, this makes it asymmetric. As to the singular part, for further manipulations it is convenient to rewrite it in the following equivalent form,

$$(h^{-1})_{\text{sing}} = \sum_{i=1,2} E_{ij}|\Xi_i\rangle\langle\Xi_j|;\ E \equiv C \begin{pmatrix} \epsilon & -2ig \\ 2ig & \epsilon \end{pmatrix} C \tag{5.24}$$

with $C^2 = D$.

The expression (5.24) should be substituted into (5.20). It is proficient to bring the result of the substitution to a Hamiltonian form for 4×4 matrices. To find this form, let us notice first that an eigenvalue equation for any block-matrix Hamiltonian,

$$\epsilon \begin{pmatrix} \psi_+ \\ \psi_- \end{pmatrix} = \begin{pmatrix} H_{++} & H_{+-} \\ H_{-+} & H_{--} \end{pmatrix} \begin{pmatrix} \psi_+ \\ \psi_- \end{pmatrix}$$

can be always represented as

$$\left(\epsilon - H_{++} - H_{+-} \frac{1}{\epsilon - H_{--}} H_{-+} \right) \psi_+ = 0$$

If we compare this with the result of the substitution of (5.24) into (5.20), we understand that it is reproduced with 2×2 blocks

$$H_{++} = -i2\sqrt{\Gamma_1\Gamma_2} h_{12}^{(0)} \begin{pmatrix} 0 & -1 \\ 1 & 0 \end{pmatrix}, \quad H_{--} = -i2g(\phi - \phi_0) \begin{pmatrix} 0 & 1 \\ -1 & 0 \end{pmatrix},$$

$$H_{+-} = H_{-+}^\dagger = i \begin{pmatrix} \sqrt{\Gamma_1} & 0 \\ 0 & \sqrt{\Gamma_2} \end{pmatrix} GC;$$

where the matrix G is made of inner products of the eigenvectors $|\Psi_i\rangle$ and $|\Xi_i\rangle$, $G_{ij} = \langle \Psi_i | \Xi_j \rangle$.

The resulting 4×4 BdG antisymmetric Hamiltonian is readily second-quantized with a 4-vector γ of Majorana creation-annihilation operators,

$$\hat{H} = \frac{1}{2} \gamma^T H \gamma.$$

Comparing this with the numeration of Majorana operators in the main text, we see that the vector is ordered as $\gamma^T = (\gamma_1, \gamma_4, \gamma_2, \gamma_3)$.

We observe that $H_{++} \propto \sqrt{\Gamma_1\Gamma_2}$ and therefore can be neglected in comparison with $H_{+-,-+} \simeq \sqrt{\Gamma_{1,2}}$. Setting $H_{++} = 0$, we finally come to the Hamiltonian (1) used in the main text.

The explicit expressions for the parameters used in the main text in terms of the scattering theory quantities thus read:

$$\tilde{\epsilon} = 2g, \tag{5.25}$$

$$\begin{pmatrix} t_{12} & t_{13} \\ t_{42} & t_{43} \end{pmatrix} = \begin{pmatrix} \sqrt{\Gamma_1} & 0 \\ 0 & \sqrt{\Gamma_2} \end{pmatrix} GC. \tag{5.26}$$

5.5.2 Periodic continuation of the phenomenological Hamiltonian

Far from the avoided crossing point ($|\phi - \phi_0| \gg G/\tilde{\epsilon} \ll 2\pi$), the energies merge together, so that the lowest Andreev level is close to zero, $E_2 \simeq G^2/\tilde{\epsilon} \ll G \ll \tilde{\epsilon}$. At further increase of $|\phi - \phi_0|$, the energies deviate from their linear asymptotes near the crossing points to become 2π periodic (Fig. 1d, main text). We approximate their dependence with

$$E_o = E_e = \pm\tilde{\epsilon}\left|\sin\left(\frac{\phi - \phi_0}{2}\right)\right|. \tag{5.27}$$

It may seem that the Hamiltonian may be extended to the full range of the phases simply by replacing $\phi - \phi_0$ with $2\sin((\phi - \phi_0)/2))$. However, this would result in a 4π-periodic Hamiltonian, this being at odds with the natural 2π periodicity.

To resolve this apparent discrepancy, we note that the choice of Majorana operators in Eq. 1 of the main text that describes the lowest energy states, is not unique: one can substitute instead of γ_{1-4} any linear combinations of Majorana operators of a bigger set that obey the commutation relations. The members of this bigger set would correspond to higher energy states not considered. The choice of four Majorana operators $\hat{\gamma}_{1-4}$ made does not depend on phase in the vicinity of the avoided crossing point and does depend at a bigger scale. The choice in fact is a 4π periodic one. To give an example of a 2π-periodic Hamiltonian, let us substitute γ_3 in the form of two Majorana operators that do not depend on the superconducting phase,

$$\hat{\gamma}_3 = \cos((\phi - \phi_0)/2)\hat{\gamma}_3' + \sin((\phi - \phi_0)/2)\hat{\gamma}_3'' \tag{5.28}$$

With this, we can rewrite a seemingly 4π periodic term in the form

$$\tilde{\epsilon}\sin((\phi - \phi_0)/2)\hat{\gamma}_2\hat{\gamma}_3 \to \frac{\tilde{\epsilon}}{2}\left((1 - \cos(\phi - \phi_0))\hat{\gamma}_3' + \sin(\phi - \phi_0)\hat{\gamma}_3''\right) \tag{5.29}$$

which makes the 2π periodicity explicit. In further considerations, we will work in a basis of the energy eigenstates that is explicitly 2π periodic. This makes irrelevant the details of Majorana representation outlined here.

5.5.3 Equation for density matrix

Let us give here the evolution equations on density matrix that are straightforward but too bulky to fit into the main text.

Beyond the vicinities of the crossing points $\phi = \phi_0 + 2\pi n$, n being an integer, we can disregard the terms proportional to $G_{\mathrm{o,e}}$. We work in local eigenenergy basis. To denote the elements of the density matrix, we use the subscripts e and o for even and odd parity sectors, respectively, and u and l for upper or lower states in each parity sector. We collect all the incoherent processes: relaxation, dephasing and quasiparticle poisoning. We introduce energy splitting $E(\phi(t)) = 2\tilde{\epsilon}\left|\sin\left(\frac{\phi-\phi_0}{2}\right)\right|$. With this, the equations read:

$$\frac{d\rho_{eu,eu}}{dt} = -\Gamma_r\rho_{eu,eu} - \Gamma_q\rho_{eu,eu} + \tfrac{1}{2}\Gamma_q\left(\rho_{ou,ou} + \rho_{ol,ol}\right) \tag{5.30}$$

$$\frac{d\rho_{el,el}}{dt} = \Gamma_r\rho_{eu,eu} - \Gamma_q\rho_{eu,eu} + \tfrac{1}{2}\Gamma_q\left(\rho_{ou,ou} + \rho_{ol,ol}\right) \tag{5.31}$$

$$\frac{d\rho_{eu,el}}{dt} = \left(-iE(\phi(t)) - \Gamma_d - \Gamma_q - \tfrac{1}{2}\Gamma_r\right)\rho_{eu,el}, \tag{5.32}$$

$$\frac{d\rho_{el,eu}}{dt} = \left(iE(\phi(t)) - \Gamma_d - \Gamma_q - \tfrac{1}{2}\Gamma_r\right)\rho_{el,eu}, \tag{5.33}$$

$$\frac{d\rho_{ou,ou}}{dt} = -\Gamma_r\rho_{ou,ou} - \Gamma_q\rho_{ou,ou} + \tfrac{1}{2}\Gamma_q\left(\rho_{eu,eu} + \rho_{el,el}\right) \tag{5.34}$$

$$\frac{d\rho_{ol,ol}}{dt} = \rho_{ou,ou}\Gamma_r - \rho_{ou,ou}\Gamma_q + \tfrac{1}{2}\Gamma_q\left(\rho_{eu,eu} + \rho_{el,el}\right) \tag{5.35}$$

$$\frac{d\rho_{ou,ol}}{dt} = \left(-iE(\phi(t)) - \Gamma_d - \Gamma_q - \tfrac{1}{2}\Gamma_r\right)\rho_{ou,ol} \tag{5.36}$$

$$\frac{d\rho_{ol,ou}}{dt} = \left(iE(\phi(t)) - \Gamma_d - \Gamma_q - \tfrac{1}{2}\Gamma_r\right)\rho_{ol,ou}. \tag{5.37}$$

To specify the ϕ dependence of the decoherence rate, we assume that the decoherence takes place mainly due to the non-ideal bias conditions that give rise to the fluctuations of ϕ. Those cause the fluctuations of the energy splitting $\delta E = (\partial E/\partial\phi)\delta\phi$ and are converted to the fluctuations of quantum phase thereby. In this case, $\Gamma_d \propto (\partial E/\partial\phi)^2$ and can be thus chosen to be of the form $\Gamma_d(\phi) = \Gamma_d \cos^2((\phi-\phi_0)/2)$.

In the vicinities of the crossing points we may neglect the incoherent terms. For each parity, the Hamiltonian from Eq. 1 of the main text can

be written as a 2×2 matrix

$$\hat{H} = \begin{bmatrix} G_{\mathrm{o,e}} & \tilde{\epsilon}(\phi - \phi_0) \\ -\tilde{\epsilon}(\phi - \phi_0) & -G_{\mathrm{o,e}} \end{bmatrix}$$

Integrating this over time and transforming to the eigenenergy basis reproduces the boundary condition on the density matrix given in the main text, for density matrices $\rho_b(\rho_a)$ before (after) passing the crossing point,

$$\rho_a = \hat{S}\rho_b\hat{S}^{-1}; \tag{5.38}$$

where the scattering matrix of LZ tunnelling is given by Eq. 4 of the main text and $\chi = \frac{\pi}{4} + \mathrm{Arg}\left[\Gamma(1 - i\frac{G^2}{e\dot{V}\tilde{\epsilon}})\right] + \frac{G^2}{e\dot{V}\tilde{\epsilon}}(\ln\frac{G^2}{e\dot{V}\tilde{\epsilon}} - 1)$ (Γ here is the gamma function)

5.5.4 Fast decoherence limit and master equation

Let us first consider the case of the fast decoherence when the quantum coherence quenches at the time scale smaller than the period of Josephson oscillations, $\Gamma_d \gg \omega_j$. This permits us to take into account only the diagonal elements of density matrix, the probabilities, describe their evolution with a master equation. We denote the probabilities with $p_{\alpha,\beta}$, where $\alpha = e, o$ at even or odd sectors and $\beta = u, l$ for upper or lower state in the sector. With all the processes in Fig.2 from the main text taken into account, the master equation for time intervals between the crossings reads:

$$\frac{dp_{eu}}{dt} = -(\Gamma_r + \Gamma_q)p_{eu} + \Gamma_q\frac{p_{ou} + p_{ol}}{2}, \tag{5.39}$$

$$\frac{dp_{el}}{dt} = \Gamma_r p_{eu} - \Gamma_q p_{el} + \Gamma_q\frac{p_{ou} + p_{ol}}{2}, \tag{5.40}$$

$$\frac{dp_{ou}}{dt} = -(\Gamma_r + \Gamma_q)p_{ou} + \Gamma_q\frac{p_{eu} + p_{el}}{2}, \tag{5.41}$$

$$\frac{dp_{ol}}{dt} = \Gamma_r p_{ou} - \Gamma_q p_{ol} + \Gamma_q\frac{p_{eu} + p_{el}}{2}. \tag{5.42}$$

This has to be supplemented by LZ boundary conditions at the crossing points for the probabilities before and after the passing. For the odd sector, we have

$$p^{\mathrm{a}}_{ol} = p^{\mathrm{b}}_{ol} + P_{\mathrm{o}}\left(p^{\mathrm{b}}_{ou} - p^{\mathrm{b}}_{ol}\right);\ p^{\mathrm{a}}_{ou} = p^{\mathrm{b}}_{ou} + P_{\mathrm{o}}\left(p^{\mathrm{b}}_{ol} - p^{\mathrm{b}}_{ou}\right). \tag{5.43}$$

Similar equation holds for the probabilities in the even sector.

Let us label the four possible states ou, ol, eu, el with a single index j Solution of these equation in the long time limit approaches $p^{(0)}(t)_j$, that is periodic in time with the Josephson period. To compute the correlator of the currents, we also need the propagator of the evolution equation $U_{ij}(t_2, t_1)$. It is defined at $t_2 > t_1$ as the solution of the equation at the time moment t_2, $p_i(t_2)$, with initial condition $p_k(t_1) = \delta_{kj}$.

The current is a function of a state given by

$$I_i(t) = I_{\rm m}\mathrm{sgn}(\phi - \phi_0)\cos((\phi - \phi_0)/2)\,(\delta_{i,ou} + \delta_{i,eu} - \delta_{i,ol} - \delta_{i,el}) \quad (5.44)$$

with $I_{\rm m} = (2e/\hbar)(\tilde{\varepsilon}/2)$, $\phi = \phi_0 + \omega_j t$. The correlator is expressed as

$$\langle\langle I(t_1)I(t_2)\rangle\rangle = \sum_{ij} I_i(t_1)I_j(t_2)(U_{ij}(t_1, t_2) - p_i^0(t_1))p_j^{(0)}(t_2), \quad (5.45)$$

at $t_1 > t_2$, and is obtained by permutation of the time arguments otherwise.

We solve the equation, the propagator and find the correlator numerically. The results for the current noise spectral density are presented in Fig. 3 of the main text.

5.5.5 Details of slow decoherence limit

Interesting analytical results can be obtained in the opposite limit of slow decoherence such that $\Gamma_{d,r,q} \ll \omega_j$ if in addition we assume that $\max\left(P_{LZ}, \Gamma_q/\omega_j\right) \gg \Gamma_r/\omega_j$ (the latter condition even in the absence of Γ_q is satisfied at $V > V_0/\ln(\Gamma_r/\omega_j$ and thus certainly holds in the crossover regime). Under these assumptions, the relaxation can not set a preferential state. All possible states of the junction are present with equal probability, and long time limit density matrices do not depend on time and approach $\hat{\rho}_o = \hat{\rho}_e = \frac{1}{4}\hat{1}$. In this case, we can neglect $\Gamma_{d,r,q}$ implement the pure quantum dynamics to compute the current-current correlator at time separation $|t_1 - t_2| \ll \Gamma_{d,r,q}^{-1}$. While not enough to resolve fine features of the noise spectral density such as the line-shapes of the noise peaks, this suffices to evaluate the integrated noise intensities in the vicinity of each peak.

The positions of the peaks are not bound to the multiples or integer fractions of the Josephson frequency. To understand this in general, let us note that the independent solutions $|\Psi_j\rangle$ of the Schrödinger equation

that is in our case periodic with the Josephson period $T_j \equiv 2\pi/\omega_j$, are Bloch-like functions of time satisfying

$$|\Psi_k(t+T_j)\rangle = \exp(i\lambda_k)|\Psi_k(t)\rangle \tag{5.46}$$

and having Fourier components at discrete frequencies $\omega_j(n+\lambda_k/2\pi)$. The correlators thus can have Fourier components at all discrete frequencies satisfying $\omega_j(n+(\lambda_k-\lambda_l)/2\pi)$.

To analyze the quantum dynamics in the case under consideration it is proficient to apply a unitary transform that cancels the evolution of the wave function during the "free motion" between the crossing points. The phase difference χ accumulated in the course of the free motion (Eq. 7 of the main text) is then ascribed to the LZ scattering matrix in certain parity sector so it becomes

$$\hat{S} = \begin{pmatrix} \sqrt{1-P}e^{i\theta/2} & -e^{i\chi}\sqrt{P} \\ e^{-i\chi}\sqrt{P} & \sqrt{1-P}e^{-i\theta/2} \end{pmatrix}, \tag{5.47}$$

Since this matrix describes the evolution of the wave function over the period, its eigenvalues give $exp(-i\lambda)$ and

$$\cos(\lambda) = \sqrt{1-P}\cos(\theta/2). \tag{5.48}$$

Let us define $\gamma \equiv \arccos(\sqrt{1-P}\cos(\theta/2))/\pi$, $0 < \gamma < 1$, and recall that we have two parity sectors and correspondingly two parameters $\gamma_{o,e}$. With this, the noise spectral density is digested in the form that makes the peak positions explicit:

$$\begin{aligned} S(\omega) = \sum_{n>0} S_n \tfrac{1}{2}\left(\delta(\omega-n\omega_j)+\delta(\omega+n\omega_j)\right) + \\ \sum_{n\geq 0} S_n^{+,o}\tfrac{1}{2}\left(\delta(\omega-(\gamma_o+n)\omega_j)+\delta(\omega+(\gamma_o+n)\omega_j)\right) + \\ \sum_{n>0,\pm} S_n^{-,o}\tfrac{1}{2}\left(\delta(\omega-(-\gamma_o+n)\omega_j)+\delta(\omega+(-\gamma_o+n)\omega_j)\right) + \\ \sum_{n\geq 0} S_n^{+,e}\tfrac{1}{2}\left(\delta(\omega-(\gamma_e+n)\omega_j)+\delta(\omega+(\gamma_e+n)\omega_j)\right) + \\ \sum_{n>0,\pm} S_n^{-,e}\tfrac{1}{2}\left(\delta(\omega-(-\gamma_e+n)\omega_j)+\delta(\omega+(-\gamma_e+n)\omega_j)\right). \end{aligned}$$

The integrated intensities S_n of the main peaks are contributed by both parity sectors, while the additional peaks $S_n^{\pm,o/e}$ are in general resolved in parity with respect to the positions and height. It is worth noting that the definition of noise density in use is "quantum", so that the

noise at positive and negative frequencies does not have to be the same indicating the difference between emission and absorption of quanta with energy $\hbar\omega$. However, this is not the case in the present framework: the calculation explicitly gives the spectral density that is even in frequency.

To compute the intensities, we need to evaluate the correlator in Eq. 4 of the main text. We note that in the representation used

$$\hat{I}(t) = I_{\rm m}\cos(\omega_j t/2)\hat{\sigma}_z; \tag{5.49}$$

(crossing points corresponding to $t = nT_j$), and the evolution matrix $\hat{U}(t_2, t_1)$ that gives the wave function at t_2 from the initial condition at t_1 is simply given by

$$\hat{U}(t_2, t_1) = \left(\hat{S}\right)^N, \tag{5.50}$$

N being the number of the crossing points at the interval (t_2, t_1).

For the intensities of the main peaks, this gives

$$S_n = I_m^2 \frac{16n^2}{\pi^2\left(4n^2-1\right)^2}\sum_{\rm o,e}\frac{1}{2}\left(1-\frac{P_{\rm o,e}}{\sin^2(\theta/2)+P_{\rm o,e}\cos^2(\theta/2)}\right) \tag{5.51}$$

As to the additional peaks, their intensities are given by

$$S(\Omega) = I_m^2\left[\frac{4}{\pi}\frac{\cos(\pi\Omega/\omega_j)\Omega\omega_j}{\omega_j^2-4\Omega^2}\right]^2\frac{P_{\rm o,e}}{\sin^2(\theta/2)+P_{\rm o,e}\cos^2(\theta/2)} \tag{5.52}$$

where Ω is the (parity-dependent) frequency position of the additional peak, P is the LZ probability at the corresponding parity.

Making use of the above relations, we plot in Fig. 4 of the main text the positions and intensities of the three lowest peaks assuming $P_{\rm o} = P_{\rm e}$, that hinders parity resolution.

To illustrate the slow decoherence limit in more detail, we present here two extra figures. Fig. 5.5 illustrates the noise intensities of the two peaks converging to $\Omega = (3/2)\omega_j$ and of the second main peak at $\Omega = 2\omega_j$. In both cases, the relative intensity is substantial in the crossover region $V \simeq V_0$ and slowly falls off upon increasing V. Fig. 5.6 represents the generic case of parity separation. The LZ probabilities here are taken to be distinctly different in the crossover region corresponding to $G_e = 4G_o$. We see that a so-to-say 4π periodic peak at $\omega_j/2$ in fact consists of the four distinct peaks of different intensity slowly converging to $1/4$ of the full intensity in the limit $V \gg V_0$.

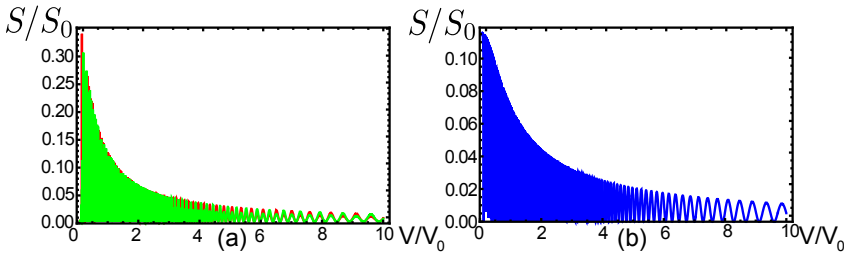

Figure 5.5. Intensities of the high-frequency noise peaks. The parameters are the same as in Fig. 4 of the main text. Left: two additional peaks with frequencies converging to $(3/2)\omega_j$ at $V \gg V_0$.Right: main peak at $2\omega_j$.

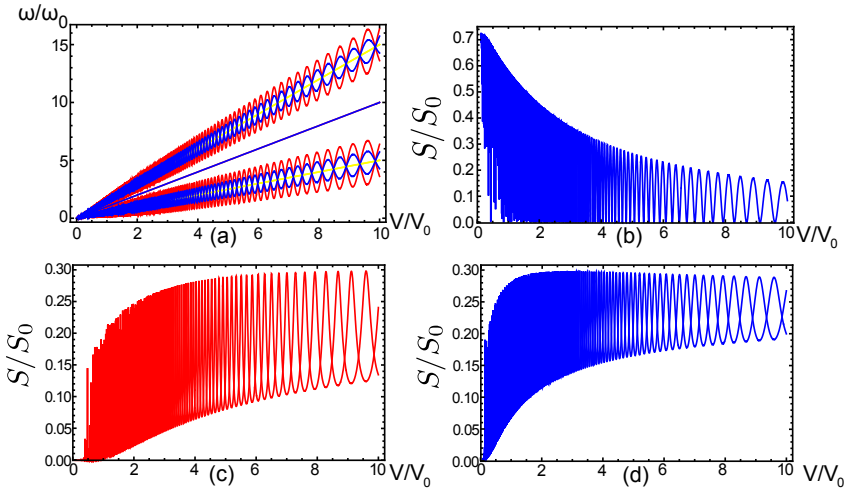

Figure 5.6. The generic case of parity separation. Here, $V_0 = 4\pi G_o^2/\tilde{\epsilon}$, $\omega_0 = 2eV_0/\hbar$, $\tilde{\epsilon}/\omega_0 = 30$, $S_0 \equiv I_m^2/2$. a. Peak positions. Four distinct noise peaks converge to half-integer multiples of ω_j upon increasing voltage. b. Spectral intensity of the main peak at ω_j. It is contributed by both parities. c. The same for the first two even parity peaks. d. The same for the two odd parity peaks.

Bibliography

[1] G. Moore and N. Read, Nucl. Phys. B **360** 362 (1991).

[2] A. Y. Kitaev, Phys.-Usp. **44**, 131 (2001).

[3] D. A. Ivanov, Phys. Rev. Lett. **86**, 268 (2001).

[4] A. Y. Kitaev, Ann. Phys. **303**, 2 (2003).

[5] See C.W.J. Beenakker, Annu. Rev. Con. Mat. Phys. **4**, 113 (2013) for a review.

[6] J. D. Sau, R. M. Lutchyn, S. Tewari, and S. Das Sarma, Phys. Rev. Lett. **104**, 040502 (2010).

[7] R. M. Lutchyn, J. D. Sau, and S. Das Sarma, Phys. Rev. Lett. **105**, 077001 (2010).

[8] Y. Oreg, G. Refael, and F. von Oppen, Phys. Rev. Lett. **105**, 177002 (2010).

[9] L. Fu and C. L. Kane, Phys. Rev. Lett. **100**, 096407 (2008).

[10] A. R. Akhmerov, J. Nilsson, and C. W. J. Beenakker, Phys. Rev. Lett. **102**, 216404 (2009).

[11] M. Wimmer, A. R. Akhmerov, J. P. Dahlhaus, and C. W. J. Beenakker, New J. Phys. **13** 053016 (2011).

[12] L. Fu and C. L. Kane, Phys. Rev. B **79**, 161408(R) (2009).

[13] J. Alicea, Y. Oreg, G. Refael, F. von Oppen, and M. P. A. Fisher, Nature Physics **7**, 412 (2011).

[14] D. M. Badiane, M. Houzet, and J. S. Meyer, Phys. Rev. Lett. **107**, 177002 (2011).

[15] L. Jiang, D. Pekker, J. Alicea, G. Refael1, Y. Oreg, and F. von Oppen, Phys. Rev. Lett. **107**, 236401 (2011).

[16] D. I. Pikulin and Yu. V. Nazarov, JETP Lett. **94**, 9, 752 (2011).

[17] P. San-Jose, E. Prada, and R. Aguado, Phys. Rev. Lett. **108**, 257001 (2012).

[18] L. P. Kouwenhoven, private communication.

[19] E. Majorana, Nuovo Cimento **14**, 170 (1937).

[20] See appendix.

[21] Y. Nakamura, Yu. A. Pashkin, and J. S. Tsai, Nature **398**, 786 (1999).

[22] A. Zazunov, V.S. Shumeiko, E.N. Bratus', J. Lantz, and G. Wendin, Phys. Rev. Lett. **90**, 087003 (2003).

[23] L. Y. Gorelik, S. I. Kulinich, R. I. Shekhter, and M. Jonson, Phys. Rev. B **69**, 094516 (2004)

[24] L. Landau, Phys. Z. USSR, **2**, 46 (1932); C. Zener, Proc. Roy. Soc. Lond. A **137** (6): 696 (1932).

[25] B. D. Josephson, Rev. Mod. Phys. **36**, 216 (1964);

[26] L. Fu and C. L. Kane, Phys. Rev. B **79**, 161408(R) (2009).

[27] W. D. Oliver, Y. Yu, J. C. Lee, K. K. Berggren, L. S. Levitov, and T. P. Orlando, Science **310**, 1653 (2005); J. Tuorila, M. Silveri, M. Sillanpää, E. Thuneberg, Y. Makhlin, and P. Hakonen, Phys. Rev. Lett. **105**, 257003 (2010).

[28] L. P. Rokhinson, X. Liu, and J. K. Furdyna, Nature Physics **8**, 795 (2012).

[29] F. Domínguez, F. Hassler, and G. Platero, Phys. Rev. B **86**, 140503(R) (2012).

[30] C. W. J. Beenakker, Rev. Mod. Phys. **69**, 731 (1997).

Chapter 6

Fermion-parity anomaly of the critical supercurrent in the quantum spin-Hall effect

6.1 Introduction

The quantum Hall effect and quantum spin-Hall effect both refer to a two-dimensional semiconductor with an insulating bulk and a conducting edge, and both exhibit a quantized electrical conductance between two metal electrodes. If the electrodes are superconducting, a current can flow in equilibrium, induced by a magnetic flux without any applied voltage. In the quantum Hall effect, the edge states are chiral (propagating in a single direction only) and two opposite edges are needed to carry a supercurrent [1–3]. Graphene is an ideal system to study this interplay of the Josephson effect and the quantum Hall effect in a strong magnetic field [4–6].

The interplay of the Josephson effect and the quantum spin-Hall effect, in zero magnetic field, has not yet been demonstrated experimentally but promises to be strikingly different [7]. The quantum spin-Hall insulator has helical edge states (propagating in both directions) that can carry a supercurrent along a single edge. The edge state couples a pair of Majorana zero-modes, allowing for the transmission of unpaired electrons with h/e rather than $h/2e$ periodic dependence on the magnetic flux [8, 9].

An h/e flux periodicity corresponds to a 4π-periodicity in terms of

the superconducting phase difference ϕ, which means that the current-phase relationship has two branches $I_\pm(\phi)$ and the system switches from one branch to the other when ϕ is advanced by 2π at fixed total number $\mathcal{N}$ of electrons in the system. This is referred to as a fermion-parity anomaly, because the two branches have different parity $\sigma = \pm$ of the number of electrons in the superconducting ground state [8].

Josephson junctions come in two types [10], depending on whether the separation L of the superconducting electrodes is small or large compared to the coherence length $\xi = \hbar v/\Delta$, or equivalently, whether the superconducting gap Δ is small or large compared to the Thouless energy $E_{\rm T} = \hbar v/L$. Existing literature [7–9, 11–18] has focused on the short-junction regime $L \ll \xi$. The supercurrent is then determined entirely by the phase dependence of a small number of Andreev levels in the gap, just one per transverse mode. The phase dependence of the continuous spectrum above the gap can be neglected. As the ratio L/ξ increases, the Andreev levels proliferate and also the continuous spectrum starts to contribute to the supercurrent. Since σ is switched by changing the occupation of a single level, one might wonder whether a significant parity dependence remains in the long-junction regime.

Remarkably enough, the parity dependence becomes even stronger. While in a short junction the two branches $I_+(\phi) = -I_-(\phi)$ differ only in sign, we find that in a long junction they differ both in sign and in magnitude. In particular, the largest current that can flow without dissipation is twice as large for I_- than it is for I_+. The difference is illustrated in Fig. 6.1, in the zero-temperature limit. The basic physics can be explained in simple terms, as we will do first, and then we will present a complete theory for finite temperature and for arbitrary ratio L/ξ.

6.2 Short-junction limit

We set the stage by summarizing the findings of Fu and Kane [7] in the short-junction regime. The spectrum of the Bogoliubov-De Gennes Hamiltonian $H_{\rm BdG}$ is a $\pm\varepsilon$ symmetric combination of a discrete spectrum for $|\varepsilon| < \Delta$ and a continuous spectrum for $|\varepsilon| > \Delta$. Since backscattering along the quantum spin-Hall edge is forbidden by time-reversal symmetry [19], this is a ballistic single-channel Josephson junction. In the limit $L/\xi \to 0$ the discrete spectrum consists of a pair of levels at

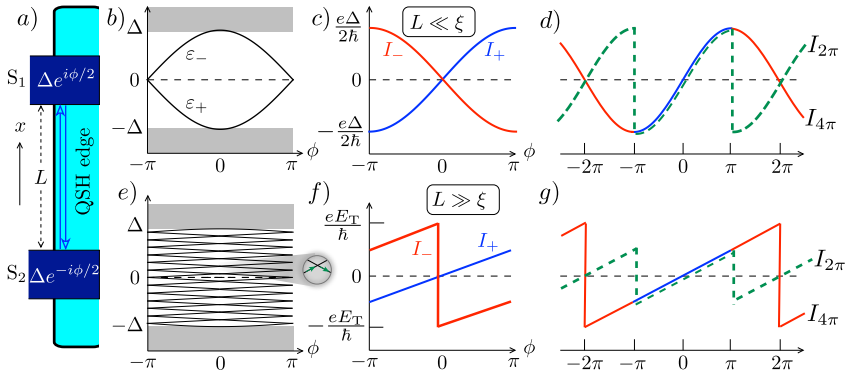

Figure 6.1. Phase-dependent excitation spectrum of a Josephson junction along a quantum spin-Hall (QSH) edge (left panels) and corresponding zero-temperature supercurrent (right panels). The supercurrent $I_{4\pi}$ is 4π-periodic, with two branches I_+ (blue solid), I_- (red solid) distinguished by the ground-state fermion parity and with a parity switch at $\phi = \pm\pi$. The top row shows the short-junction limit of Ref. 7, the bottom row the long-junction limit calculated here. (The jump in I_- at $\phi = 0$ occurs because of the change in slope indicated by the green arrows in the magnified central part of the spectrum.) The 2π-periodic supercurrent $I_{2\pi}$ without parity constraints is also shown (green dashed). The critical current is the same for $I_{4\pi}$ and $I_{2\pi}$ in the short junction, but different by a factor of two in the long junction.

$\varepsilon_\pm = \mp\Delta|\cos(\phi/2)|$, while the continuous spectrum is ϕ-independent [20]. Quite generally, an eigenvalue $\varepsilon(\phi)$ of $H_{\rm BdG}$ contributes to the supercurrent an amount

$$I(\phi) = \frac{ge}{\hbar}\frac{d}{d\phi}\varepsilon(\phi), \tag{6.1}$$

with g a factor that counts spin and other degeneracies [21]. There is no spin degeneracy at the quantum spin-Hall edge (since spin is tied to the direction of motion), so $g = 1$ and the level $\varepsilon_\pm$ contributes a supercurrent [7]

$$I_\pm(\phi) = \pm\frac{e\Delta}{2\hbar}\sin(\phi/2), \quad |\phi| < \pi. \tag{6.2}$$

To discuss the fermion-parity anomaly we assume, for definiteness, that the total number $\mathcal{N}$ of electrons in the system is even. (A different choice amounts to a 2π phase shift, or equivalently, an interchange of I_+ and I_-.) The ground-state fermion parity σ is even for $\phi = 0$ and switches to odd when ϕ crosses π. Since $\mathcal{N}$ is fixed, this topological

phase transition must be accompanied by a switch between even and odd number of quasiparticle excitations. At zero temperature only the two levels $\varepsilon_\pm$ closest to the Fermi level ($\varepsilon = 0$) play a role, and the parity switch of σ means that a quasiparticle is transferred from $\varepsilon_+ < 0$ to $\varepsilon_- > 0$. It cannot relax back from ε_- to ε_+ at fixed parity of $\mathcal{N}$.

The resulting current-phase relationship can be represented by a switch between 2π-periodic branches $I_\pm(\phi)$ (reduced zone scheme), or equivalently as a 4π-periodic function $I_{4\pi}(\phi)$ (extended zone scheme). Both representations are shown in Fig. 6.1, upper panels. We also include the 2π-periodic current $I_{2\pi}$ that results if the system can relax to its lowest energy state without constraints on the parity of $\mathcal{N}$.

6.3 Long-junction limit

An elementary discussion of the long-junction regime (to be made rigorous in just a moment) goes as follows. For $L \gg \xi$ we may assume [22–24] a local linear relation between the current density I and the phase gradient $\phi/L \ll 1/\xi$, of the form $I = \text{constant} \times ev\phi/L$. The linear increase of I_- is interrupted at $\phi = 0$ by a discontinuity $\Delta I_- = 2ev/L$. Half of it results from the jump in the slope of the lowest occupied positive energy level $\varepsilon = (\pi - |\phi|)\hbar v/2L$ (green arrows in Fig. 6.1e). The jump in the slope of the highest occupied negative energy level contributes the other half. In the extended zone scheme, the resulting supercurrent $I_{4\pi}$ is a 4π-periodic sawtooth with a slope $\Delta I_-/4\pi = eE_{\rm T}/2\pi\hbar$.

The corresponding parity-dependent supercurrents in the reduced zone scheme are

$$I_+ = \frac{eE_{\rm T}}{2\pi\hbar}\phi, \quad I_- = \frac{eE_{\rm T}}{2\pi\hbar}(\phi - 2\pi\,\mathrm{sign}\,\phi), \quad |\phi| < \pi. \tag{6.3}$$

The 4π-periodic supercurrent $I_{4\pi}$ switches from I_+ to I_- at $\phi = \pi$, while $I_{2\pi}$ remains in the branch I_+ by compensating the switch in ground-state fermion parity σ by a switch in the parity of the electron number $\mathcal{N}$. These are the curves plotted in Fig. 6.1 (lower panels).

Looking at the upper panels, one might have expected the sinusoidal current-phase relationship of $I_{4\pi}$ for a short junction to evolve into a triangular profile for a long junction, remaining symmetric around $\phi = \pi$. This would produce a cusp at the topological phase transition, which is avoided by the sawtooth profile — at the expense of a discontinuity at $\phi = 2\pi$.

The maximal supercurrent is reached near $\phi = 2\pi$ for $I_{4\pi}$ (with parity constraint) and near $\phi = \pi$ for $I_{2\pi}$ (without parity constraint). There is a factor of two difference in magnitude of these critical currents in a long junction,

$$I_{4\pi,\mathrm{c}} = eE_{\mathrm{T}}/\hbar, \quad I_{2\pi,\mathrm{c}} = eE_{\mathrm{T}}/2\hbar. \tag{6.4}$$

In contrast, for a short junction both are the same (equal to $e\Delta/2\hbar$).

6.4 Current through the scattering matrix

To determine the crossover from the short-junction limit (6.2) to the long-junction limit (6.3), including the temperature dependence, we adapt the scattering theory of the Josephson effect [25] to include the fermion parity constraints. Input is the scattering matrix s_0 of electrons in the normal region and the Andreev reflection matrix r_{A} at the normal-superconductor interfaces. These take a particularly simple 2×2 form at the quantum spin-Hall edge, but our general formulas are applicable also to *multi-channel* topological superconductors.

The parity-dependent partition function is [12–14, 26]

$$\begin{aligned} Z_\pm &= \tfrac{1}{2}\left(\prod_{\varepsilon>0} e^{\beta\varepsilon/2}\right)\left(\prod_{\varepsilon>0}(1+e^{-\beta\varepsilon}) \pm \prod_{\varepsilon>0}(1-e^{-\beta\varepsilon})\right) \\ &= \tfrac{1}{2}Z_0\left(1 \pm \prod_{\varepsilon>0}\tanh(\beta\varepsilon/2)\right), \end{aligned} \tag{6.5}$$

with $\beta = 1/k_{\mathrm{B}}T$ and $Z_0 = \prod_{\varepsilon>0} 2\cosh(\beta\varepsilon/2)$ the partition function without parity constraints. From the expression for $Z_\pm$ one can see that the $\pm$ selects terms that contain an even $(+)$ or an odd $(-)$ number of quasiparticle excitation factors $e^{-\beta\varepsilon}$, as is dictated by the ground-state fermion parity. The partition function Z gives the free energy F and hence the supercurrent I [27],

$$I_\pm = \frac{2e}{\hbar}\frac{dF_\pm}{d\phi}, \quad F_\pm = -\beta^{-1}\ln Z_\pm, \tag{6.6}$$

$$I_{2\pi} \equiv I_0 = \frac{2e}{\hbar}\frac{dF_0}{d\phi}, \quad F_0 = -\beta^{-1}\ln Z_0. \tag{6.7}$$

The density of states $\rho(\varepsilon)$ contains both the discrete spectrum for $|\varepsilon| < \Delta$ (a sum of delta functions at the Andreev levels) and the continuous spectrum for $|\varepsilon| > \Delta$, including also a contribution ρ_{S} from the

superconducting electrodes. Scattering theory gives the expression [25]

$$\rho(\varepsilon) = \mathrm{Im}\,\frac{d}{d\varepsilon}\nu(\varepsilon + i0^+) + \rho_{\mathrm{S}}(\varepsilon), \tag{6.8}$$

$$\nu(\varepsilon) = -\pi^{-1}\ln\mathrm{Det}\,X(\varepsilon), \quad X = (1-M)M^{-1/2}, \tag{6.9}$$

$$M(\varepsilon) = r_{\mathrm{A}}^*(-\varepsilon)s_0^*(-\varepsilon)r_{\mathrm{A}}(\varepsilon)s_0(\varepsilon). \tag{6.10}$$

The factor $M^{-1/2}$ in the definition of X, as well as the term ρ_{S}, give a ϕ-independent additive contribution to F_0 without any effect on I_0, but we need to retain these terms here because they do enter into the parity constraint for $I_\pm$.

In the absence of parity constraints, Ref. 28 gives the free energy

$$F_0 = -\beta^{-1}\textstyle\sum_{p=0}^{\infty}\ln\mathrm{Det}\,X(i\omega_p), \tag{6.11}$$

as a sum over fermionic Matsubara frequencies $\omega_p = (2p+1)\pi/\beta$. A similar calculation [29] gives the parity-dependence in the form

$$F_\sigma = F_0 - \beta^{-1}\ln\tfrac{1}{2}\Bigg[1 + \sigma e^{J_{\mathrm{S}}}\sqrt{\mathrm{Det}\,X(0)} \times \exp\Bigg(\sum_{p=1}^{\infty}(-1)^p\ln\mathrm{Det}\,X(i\Omega_p/2)\Bigg)\Bigg], \tag{6.12}$$

$$\sigma = \mathrm{sign}\left[\mathrm{Pf}\,(r_{\mathrm{A}}s_0 - s_0^{\mathrm{T}}r_{\mathrm{A}}^{\mathrm{T}})(\mathrm{Det}\,is_0)^{-1/2}\right]_{\varepsilon=0}, \tag{6.13}$$

with bosonic Matsubara frequencies $\Omega_p = 2p\pi/\beta$. The ground-state fermion parity σ is given in terms of the Pfaffian of the anti-symmetrized scattering matrix, evaluated at the Fermi energy. The sign ambiguity in the square root is resolved by fixing $\sigma = 1$ at $\phi = 0$.

Eq. (6.12) contains a contribution from the superconducting electrodes,

$$J_{\mathrm{S}} = \int_{\Delta}^{\infty} d\varepsilon\,\rho_{\mathrm{S}}(\varepsilon)\ln\tanh(\beta\varepsilon/2), \tag{6.14}$$

which only plays a role at temperatures $T \gtrsim \Delta/k_{\mathrm{B}}$. The factor $e^{J_{\mathrm{S}}}$ can therefore be replaced by unity in the long-junction regime, when $k_{\mathrm{B}}T \lesssim E_{\mathrm{T}} \ll \Delta$.

We now specify these general formulas for the quantum spin-Hall edge, with Hamiltonian [30]

$$H_{\mathrm{BdG}} = \begin{pmatrix} vp\sigma_z + U(x) & \Delta^*(x)\sigma_y \\ \Delta(x)\sigma_y & vp\sigma_z - U(x) \end{pmatrix}. \tag{6.15}$$

The edge runs along the x-axis, $p = -i\hbar\partial_x$ is the momentum operator, and the electrostatic potential is $U(x)$ (measured relative to the Fermi level). The pair potential $\Delta(x)$ vanishes in the normal region $|x| < L/2$. In the two superconducting regions we set $\Delta(x) = \Delta e^{\pm i\phi/2}$, with a step at $x = \pm L/2$. This socalled "rigid boundary condition" is justified for a single channel coupled to a bulk superconducting reservoir [10].

A mode-matching calculation gives the scattering matrices

$$s_0 = \begin{pmatrix} 0 & e^{i\chi} \\ e^{i\chi} & 0 \end{pmatrix}, \quad \chi(\varepsilon) = \chi_0 + \varepsilon/E_{\rm T}, \tag{6.16}$$

$$r_{\rm A} = \begin{pmatrix} \alpha e^{i\phi/2} & 0 \\ 0 & -\alpha e^{-i\phi/2} \end{pmatrix}, \quad \alpha(\varepsilon) = \sqrt{1 - \frac{\varepsilon^2}{\Delta^2}} + \frac{i\varepsilon}{\Delta},$$

$$\mathrm{Det}\, X(\varepsilon) = 2\cos\phi + \alpha^2 e^{2i\varepsilon/E_{\rm T}} + \alpha^{-2} e^{-2i\varepsilon/E_{\rm T}}. \tag{6.17}$$

We discuss the various terms in these expressions. The electron scattering matrix s_0 is purely off-diagonal, because of the absence of backscattering along the quantum spin-Hall edge. The transmission phase χ depends linearly on energy because of the linear dispersion. Electrostatic potential fluctuations contribute only to the energy-independent offset $\chi_0 = -(\hbar v)^{-1} \int_0^L U\, dx$, which drops out in Eq. (6.9). The Andreev reflection matrix $r_{\rm A}$ (from electron to hole) is unitary below the gap. Above the gap there is also propagation into the superconductor, so $r_{\rm A}$ is sub-unitary. The same expression (6.16) for $r_{\rm A}$ applies at all energies, evaluated at $\varepsilon + i0^+$ to avoid the branch cut of the square root. Notice that for $\phi = 0$ the Andreev reflection amplitudes from S_1 and S_2 differ by a minus sign, because of the opposite spin of counterprogating electrons in a helical edge state.

6.5 Results and discussion

Putting all pieces together [29] we obtain the parity-dependent supercurrent for arbitrary ratio $\Delta/E_{\rm T}$. In the short-junction limit $\Delta/E_{\rm T} \to 0$ we recover the known result (6.2), when the energy dependence of the scattering matrix and the phase sensitivity of the continuous spectrum can both be ignored. In the opposite long-junction limit $\Delta/E_{\rm T} \to \infty$ we

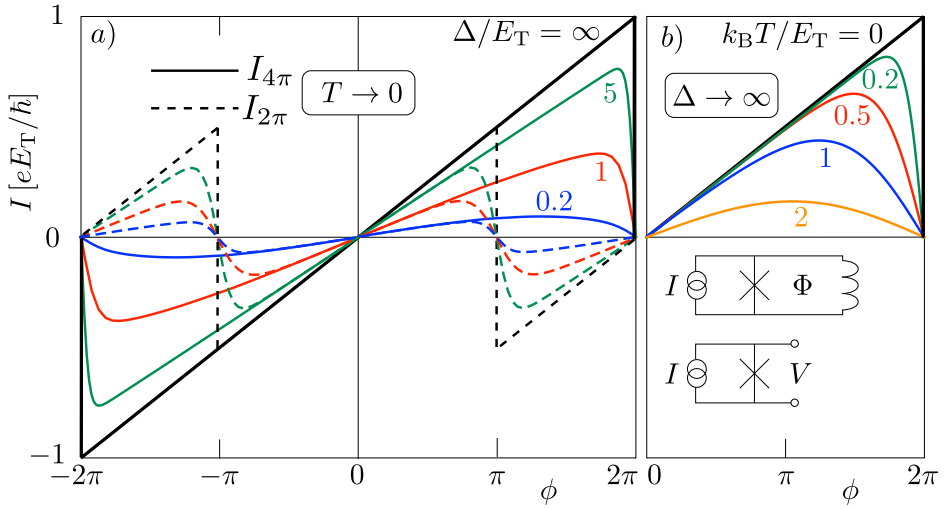

Figure 6.2. Phase dependence of the parity-constrained supercurrent $I_{4\pi}$ (solid curves, in units of $eE_{\rm T}/\hbar \propto 1/L$), calculated by a numerical evaluation of the Matsubara sums. The left panel shows the crossover from the short-junction to the long-junction regime in the zero-temperature limit (full interval $-2\pi < \phi < 2\pi$). The right panel shows the temperature dependence in the long-junction limit (reduced interval $0 < \phi < 2\pi$). The left panel also shows the supercurrent $I_{2\pi}$ without parity constraints (dashed curves). The insets in the right panel show current-biased superconducting circuits that measure the I-V and I-Φ relationships of a Josephson junction.

find

$$I_{4\pi} = I_0 - \frac{2e}{\hbar\beta}\frac{d}{d\phi}\ln\left[\tfrac{1}{2}+\cos(\phi/2)e^{\mathcal{S}-\pi/2\beta E_{\rm T}}\right], \tag{6.18}$$

$$\mathcal{S} = \sum_{p=1}^{\infty}(-1)^p \ln\left(1+2e^{-\Omega_p/E_{\rm T}}\cos\phi + e^{-2\Omega_p/E_{\rm T}}\right), \tag{6.19}$$

$$I_{2\pi} \equiv I_0 = \frac{2e}{\hbar\beta}\sin\phi\sum_{p=0}^{\infty}\left[\cos\phi+\cosh(2\omega_p/E_{\rm T})\right]^{-1}. \tag{6.20}$$

The plot of the results in Fig. 6.2 shows that the crossover from a sine to a sawtooth shape occurs early: already for $\Delta = E_{\rm T}$ (so for $L = \xi$) the maximum of the current-phase relationship is close to $\phi = 2\pi$. The sawtooth shape is preserved with increasing temperature for $k_{\rm B}T \lesssim \frac{1}{2}E_{\rm T}$.

These are encouraging results for the experimental accessibility of the long-junction regime. The quantum spin-Hall effect has been ob-

served in HgTe/CdTe quantum wells [31], and more recently in InAs/GaSb quantum wells [32] — where also Andreev reflection from superconducting Nb electrodes was demonstrated [33]. For a typical Fermi velocity of $v \simeq 10^5\,\mathrm{m/s}$ in a semiconductor and superconducting gap $\Delta \simeq 1\,\mathrm{meV}$ in bulk Nb, the coherence length is $\xi = 70\,\mathrm{nm}$, so the Josephson junction length $L = 0.5\,\mu\mathrm{m}$ from Ref. 33 is deep in the long-junction regime. Since the long-junction regime is already entered for $L \approx \xi$, this would apply even if the effective superconducting gap is well below the bulk value of Nb. The corresponding Thouless energy is $E_\mathrm{T}/k_\mathrm{B} = 1.5\,\mathrm{K}$, so at $T = 100\,\mathrm{mK}$ one should be close to the low-temperature limit.

In the ongoing search for the 4π-periodic Josephson effect the first results have been reported [34] for the AC effect (fractional Shapiro steps [9, 15–18]). A DC measurement of the current-flux (I-Φ, $\phi = 2e\Phi/\hbar$) relationship, on time scales large compared to the time $\tau_\mathrm{qp} \simeq \mu\mathrm{s}$ for unpaired quasiparticles to tunnel into the system [35], will measure the 2π-periodic $I_{2\pi}$ rather than $I_{4\pi}$. Such a phase-sensitive measurement (Fig. 6.2, upper inset) would produce the critical current $I_{2\pi,\mathrm{c}}$ without any signature of the parity anomaly. In contrast, a phase-*insensitive* measurement of the critical current through the current-voltage (I-V) characteristic (lower inset) will produce $I_{4\pi,\mathrm{c}}$ even on time scales $\gg \tau_\mathrm{qp}$, because the phase of a resistively shunted (overdamped) circuit can adjust to a change in $\mathcal{N}$ on time scales much smaller than τ_qp. A change in the parity of $\mathcal{N}$ will be compensated by a 2π phase shift, without a change in critical current [29]. In a short junction $I_{2\pi,\mathrm{c}}$ and $I_{4\pi,\mathrm{c}}$ are the same, so this does not help, but in a long junction they differ by up to a factor of two.

6.6 Conclusion

We have presented a theory for the 4π-periodic Josephson effect on scales large compared to the superconducting coherence length. A multitude of subgap states, as well as a continuum of states above the gap, contribute to the supercurrent for $L \gg \xi$, but still the parity anomaly responsible for the 4π-periodicity persists. In fact, we have found that in a long junction the anomaly manifests itself also in a phase-insensitive way, through a doubling of the critical current. This opens up new possibilities for the detection of this topological effect at the quantum spin-Hall edge [31–33], and possibly also in semiconductor nanowires

[34, 36–38].

6.7 Appendix

6.8 Details of the calculation of the free energy

6.8.1 Transformation from the real to the imaginary energy axis

According to Eq. (6.5) the free energy $F_\sigma = -\beta^{-1} \ln Z_\sigma$, with $\sigma = \pm 1$ the ground-state fermion parity, is given by

$$F_\sigma = F_0 - \beta^{-1} \ln \tfrac{1}{2} \left[1 + \sigma \exp\left(\sum_{\varepsilon>0} \ln \tanh(\beta\varepsilon/2) \right) \right], \tag{6.21}$$

$$F_0 = -\beta^{-1} \sum_{\varepsilon>0} \ln[2\cosh(\beta\varepsilon/2)]. \tag{6.22}$$

Here F_0 is the free energy in the absence of parity constraints. The infinite product over ε is defined in terms of the density of states ρ by

$$\prod_{\varepsilon>0} f(\varepsilon) = \exp\left[\int_0^\infty d\varepsilon\, \rho(\varepsilon) \ln f(\varepsilon) \right]. \tag{6.23}$$

Integrals of the type (6.23) can be done efficiently by contour integration, made possible by the fact that the scattering matrices are analytic in the upper half of the complex energy plane. This was worked out in Ref. 28 for F_0, and here we adapt that method to include the parity constraint in F_σ.

The function ν in the density of states (6.8) satisfies $\nu(\varepsilon) = \nu^*(-\varepsilon)$, expressing the electron-hole symmetry. If $f(\varepsilon)$ is an even function of ε, we may therefore convert the sum $\sum_{\varepsilon>0} f(\varepsilon)$ over positive energies (including both the discrete and the continuous spectrum) into an integral along the entire real energy axis of $f d\nu/d\varepsilon$, or $\nu df/d\varepsilon$ after a partial integration. Closing the contour in the upper half of the complex energy plane picks up the poles of $df/d\varepsilon$, which for the free energy are the Matsubara frequencies on the imaginary axis.

In Ref. 28 this transformation was carried out for F_0, leading to

$$\begin{aligned}\sum_{\varepsilon>0} \ln[2\cosh(\beta\varepsilon/2)] &= \int_0^\infty d\varepsilon\, \rho(\varepsilon) \ln[2\cosh(\beta\varepsilon/2)] \\ &= \frac{1}{2i}\int_{-\infty}^{\infty} d\varepsilon\, \frac{d\nu(\varepsilon+i0^+)}{d\varepsilon} \ln[2\cosh(\beta\varepsilon/2)] \\ &= -\frac{\beta}{4i}\int_{-\infty}^{\infty} d\varepsilon\, \nu(\varepsilon+i0^+)\tanh(\beta\varepsilon/2) \\ &= -\pi\sum_{p=0}^{\infty} \nu(i\omega_p), \end{aligned} \tag{6.24}$$

with $\omega_p = (2p+1)\pi/\beta$ the fermionic Matsubara frequency. For F_σ the Matsubara sum contains bosonic Matsubara frequencies $\Omega_p = 2p\pi/\beta$,

$$\begin{aligned}\sum_{\varepsilon>0} \ln\tanh(\beta\varepsilon/2) &= \frac{1}{2i}\int_{-\infty}^{\infty} d\varepsilon\, \frac{d\nu(\varepsilon+i0^+)}{d\varepsilon} \\ &\qquad \times \ln|\tanh(\beta\varepsilon/2)| \\ &= -\frac{\beta}{2i}\fint_{-\infty}^{\infty} d\varepsilon\, \nu(\varepsilon+i0^+)\frac{1}{\sinh\beta\varepsilon} \\ &= -\pi\sum_{p=1}^{\infty}(-1)^p \nu(i\Omega_p/2) - \tfrac{1}{2}\pi\nu(0). \end{aligned} \tag{6.25}$$

The notation $\fint$ indicates the Cauchy principal value of the integral (which picks up half of the pole at $\varepsilon = 0$). We have made use of the identity

$$\int dx\, \frac{df}{dx} \ln|x| = -\fint dx\, f(x)\frac{1}{x}. \tag{6.26}$$

For the free energy this gives

$$F_0 = -\beta^{-1}\sum_{p=0}^{\infty} \ln\mathrm{Det}\, X(i\omega_p), \tag{6.27}$$

$$F_\sigma = F_0 - \beta^{-1}\ln\tfrac{1}{2}\left[1 + \sigma e^{J_S}\sqrt{\mathrm{Det}\, X(0)}\exp\left(\sum_{p=1}^{\infty}(-1)^p \ln\mathrm{Det}\, X(i\Omega_p/2)\right)\right], \tag{6.28}$$

where we have substituted $\nu = -\pi^{-1}\ln\mathrm{Det}\, X$ from Eq. (6.9) and also included the factor e^{J_S} from the ϕ-independent density of states in the superconducting electrodes.

6.8.2 Regularization

The transformation of the integral (6.25) over real energies into a sum over imaginary frequencies requires that $\nu(i\omega)$ goes to zero faster than $1/\omega$ for $\omega \to \infty$. To ensure this, we decompose $\nu = \nu_\infty + \delta\nu$, with ν_∞ the large-ω limit of $\nu(i\omega)$. It is convenient to specify $\nu_\infty(0) = 0$. The integral over ν_∞ is done along the real energy axis, where it converges, and then the remaining integral over $\delta\nu$ becomes a converging sum over Matsubara frequencies.

More specifically, for the quantum spin-Hall edge we take

$$\nu_\infty(\varepsilon) = -\pi^{-1} \ln\bigl[(1 - 4\varepsilon^2/\Delta^2) e^{-2i\varepsilon/E_{\rm T}}\bigr], \tag{6.29}$$

in view of Eq. (6.17). The integral over ν_∞ can be evaluated in closed form,

$$\begin{aligned} J_\infty &\equiv -\frac{\beta}{2i} \fint_{-\infty}^{\infty} d\varepsilon\, \nu_\infty(\varepsilon + i0^+) \frac{1}{\sinh \beta\varepsilon} \\ &= -\frac{1}{\pi\beta E_{\rm T}} \int_{-\infty}^{\infty} dx\, \frac{x}{\sinh x} - \int_{\beta\Delta/2}^{\infty} dx\, \frac{1}{\sinh x} \\ &= -\frac{\pi}{2\beta E_{\rm T}} + \ln\tanh(\beta\Delta/4). \end{aligned} \tag{6.30}$$

The remaining integral over $\delta\nu = \nu - \nu_\infty$ then becomes a convergent sum over Matsubara frequencies,

$$-\frac{\beta}{2i} \fint_{-\infty}^{\infty} d\varepsilon\, \frac{\delta\nu(\varepsilon + i0^+)}{\sinh \beta\varepsilon} = \mathcal{S} - \tfrac{1}{2}\pi\nu(0), \tag{6.31}$$

$$\mathcal{S} = -\pi \sum_{p=1}^{\infty} (-1)^p \bigl[\nu(i\Omega_p/2) - \nu_\infty(i\Omega_p/2)\bigr]. \tag{6.32}$$

This gives the regularized version of Eq. (6.28),

$$F_\sigma = F_0 - \beta^{-1} \ln \tfrac{1}{2}\bigl(1 + \sigma e^{\mathcal{S}+J_\infty+J_{\rm S}} \sqrt{\det X(0)}\,\bigr). \tag{6.33}$$

6.9 Scattering formulas for the ground-state fermion parity

The ground-state fermion parity $\sigma(\phi)$ switches between even and odd whenever a pair of Andreev levels crosses the Fermi energy. Given

$\sigma(0) = 1$, in principle one can just count the number of level crossings between phase difference 0 and ϕ to determine σ. In a multichannel Josephson junction there can be many level crossings and a single crossing might be easily missed. It would be advantageous to have a direct method of determining σ at any ϕ, without having to track the number of sign changes back to $\phi = 0$. Kitaev's Hamiltonian expression [8] for the ground-state fermion parity is one such method, requiring information on the entire excitation spectrum. Here we construct an alternative scattering approach that requires only Fermi-level information.

We present two variations of our approach: the first assumes spatial separation of normal scattering and Andreev reflection, relating σ to the normal-state scattering matrix s_0. Alternatively, if there is no such spatial separation, we can relate σ to the transfer matrices $M_{\rm L}$, $M_{\rm R}$ at the left and right end of the Josephson junction.

It is instructive to place these results in the general context of topological states of matter [39]. The ground-state fermion parity σ is the $\mathbb{Z}_2$ topological quantum number of a system of dimensionality $d = 0$ in symmetry class D (when s_0 has no symmetry restrictions) or BDI (when $s_0 = s_0^{\rm T}$). The dimensionality zero refers to the fact that this is a closed system. We may consider opening up the system, promoting it to $d = 1$, by replacing one of the two superconducting contacts by a normal metal with N transverse modes. The topological quantum number $\mathcal{Q}$ then counts the number of Majorana zero-modes at the normal-superconducting interface. It is given by the determinant of the reflection matrix (for class D, with $\mathcal{Q} \in \mathbb{Z}_2$) [40] or by its trace (for class BDI, with $\mathcal{Q} \in \mathbb{Z}$) [41].

6.9.1 Relation between σ and the normal-state scattering matrix

The free energy (6.28) of the SNS junction incorporates the ground-state fermion parity dependence through the quantity $\sigma\sqrt{\mathrm{Det}\, X(0)}$. We seek to express this quantity in terms of the normal-state scattering matrix $s_0(0)$, assuming a spatial separation of normal scattering in N and ideal Andreev reflection at the NS interfaces.

We start from the definition of $X = (1 - M)M^{-1/2}$ and use that

$M(0) = U^*U$ with unitary $U = r_A(0)s_0(0)$. Since $\mathrm{Det}\, M = 1$, we have

$$\begin{aligned}\mathrm{Det}\, X &= \mathrm{Det}\,(1 - U^*U) = \mathrm{Det}\,(1 - U^*U)^{\mathrm{T}} \\ &= \frac{\mathrm{Det}\,(U - U^{\mathrm{T}})}{\mathrm{Det}\, U} = \frac{[\mathrm{Pf}(U - U^{\mathrm{T}})]^2}{\mathrm{Det}\, U}. \end{aligned} \tag{6.34}$$

The determinant of U is independent of ϕ,

$$\mathrm{Det}\, U = \mathrm{Det}\,[r_A(0)s_0(0)] = \mathrm{Det}\,[is_0(0)]. \tag{6.35}$$

We may now identify

$$\begin{aligned}\sigma\sqrt{\mathrm{Det}\, X(0)} &= \frac{\mathrm{Pf}\,(U^{\mathrm{T}} - U)}{\sqrt{\mathrm{Det}\, U}} \\ \Rightarrow \sigma &= \mathrm{sign}\left[\frac{\mathrm{Pf}\,(r_A s_0 - s_0^{\mathrm{T}} r_A^{\mathrm{T}})}{\sqrt{\mathrm{Det}\, is_0}}\right]_{\varepsilon=0}. \end{aligned} \tag{6.36}$$

The two branches of the square root function introduce a sign ambiguity, which is resolved as follows. The square root of $\mathrm{Det}\, X \geq 0$ is taken on the principal branch, while the branch of the square root of $\mathrm{Det}\, is_0$ is fixed by setting $\sigma = 1$ at $\phi = 0$. Once this sign is fixed, the phase dependence of the topological quantum number $\sigma(\phi)$ is determined by Eq. (6.36) entirely in terms of Fermi-level properties.

6.9.2 Relation between σ and the transfer matrix

We will now extend the scattering formulation of the ground-state fermion parity to a system where we cannot make the spatial separation of normal scattering (described by s_0) and ideal Andreev reflection (described by r_A). This is possible if we work with transfer matrices instead of scattering matrices.

It is convenient to choose a gauge where the phase difference ϕ across the Josephson junction is accounted for by the delta function vector potential $\vec{A} = (\phi\hbar/2e)\delta(x)\hat{x}$, centered at a point $x = 0$ inside the Josephson junction. The $2N \times 2N$ transfer matrices $M_L(\varepsilon)$ and $M_R(\varepsilon)$ relate electron and hole wave amplitudes to the left of $x = 0$,

$$\Psi_{L,h} = M_L \Psi_{L,e}, \tag{6.37}$$

and to the right of $x = 0$,

$$\Psi_{R,h} = M_R \Psi_{R,e}. \tag{6.38}$$

The first N components Ψ_+ of each vector $\Psi = (\Psi_+, \Psi_-)$ refer to right-moving states and the last N components Ψ_- to left-moving states. The Pauli matrix Σ_z acts on these components,

$$\Sigma_z \begin{pmatrix} \Psi_+ \\ \Psi_- \end{pmatrix} = \begin{pmatrix} 1 & 0 \\ 0 & -1 \end{pmatrix} \begin{pmatrix} \Psi_+ \\ \Psi_- \end{pmatrix} = \begin{pmatrix} \Psi_+ \\ -\Psi_- \end{pmatrix}. \tag{6.39}$$

The wave amplitudes $\Psi_{\rm L}$ and $\Psi_{\rm R}$ are matched at $x = 0$,

$$\Psi_{\rm R,e} = e^{i\phi/2}\Psi_{\rm L,e}, \;\; \Psi_{\rm R,h} = e^{-i\phi/2}\Psi_{\rm L,h}. \tag{6.40}$$

The combination of these equations gives

$$e^{i\phi/2}M_{\rm R}\Psi_{\rm L,e} = e^{-i\phi/2}M_{\rm L}\Psi_{\rm L,e}, \tag{6.41}$$

so the condition for a bound state in the junction is

$$\mathrm{Det}\left[e^{i\phi/2}M_{\rm R} - e^{-i\phi/2}M_{\rm L}\right] = 0. \tag{6.42}$$

If we take $M_{\rm L}$ and $M_{\rm R}$ at the Fermi energy $\varepsilon = 0$, this equation gives the values of ϕ at which a pair of Andreev levels crosses the Fermi level and the ground-state fermion parity switches between even and odd.

Because of the excitation gap in the bulk superconductor, there can be no particle current flowing through the Josephson junction for energies $\varepsilon < \Delta$. This requires

$$\Psi_{\rm e}^\dagger \Sigma_z \Psi_{\rm e} + \Psi_{\rm h}^\dagger \Sigma_z \Psi_{\rm h} = 0, \tag{6.43}$$

both to the left and to the right of $x = 0$. The corresponding unitarity constraint on the transfer matrices $M_{\rm L}$ and $M_{\rm R}$ is

$$M^\dagger \Sigma_z M + \Sigma_z = 0 \Rightarrow M^{-1} = -\Sigma_z M^\dagger \Sigma_z. \tag{6.44}$$

At the Fermi level $\varepsilon = 0$ we have the additional constraint of particle-hole symmetry, $M^{-1}(0) = M^*(0)$, which together with the unitarity constraint implies that $M(0)\Sigma_z$ is an antisymmetric matrix,

$$[M(0)\Sigma_z]^{\rm T} = -M(0)\Sigma_z. \tag{6.45}$$

In what follows we restrict ourselves to $\varepsilon = 0$ and omit the energy argument.

Since $|\mathrm{Det}\, M| = 1$, we may define the real angle α (modulo 2π) by

$$\mathrm{Det}\,(M_{\mathrm{L}} M_{\mathrm{R}}) = e^{-i\alpha - 2i\nu\pi}, \;\; 0 \leq \alpha < 2\pi, \;\; \nu \in \mathbb{Z}. \tag{6.46}$$

The function

$$\zeta^2(\phi) = e^{i\alpha/2 + i\nu\pi}\, \mathrm{Det}\, \left(e^{i\phi/2} M_{\mathrm{R}} \Sigma_z - e^{-i\phi/2} M_{\mathrm{L}} \Sigma_z \right) \tag{6.47}$$

is *real* for all ϕ and vanishes when the ground-state fermion parity switches. Since it is the determinant of an antisymmetric matrix, it can be written as the square of a Pfaffian,

$$\zeta(\phi) = e^{i\alpha/4 + i\nu\pi/2}\, \mathrm{Pf}\, \left(e^{i\phi/2} M_{\mathrm{R}} \Sigma_z - e^{-i\phi/2} M_{\mathrm{L}} \Sigma_z \right). \tag{6.48}$$

We choose $\nu \in \{0, 1, 2, 3\}$ such that $\zeta(0)$ is real and positive. The function $\zeta(\phi)$ then will remain real for all ϕ, switching sign when the ground-state fermion parity switches. We can thus identify the topological quantum number with

$$\sigma = \mathrm{sign}\, \left[e^{i\alpha/4 + i\nu\pi/2} \mathrm{Pf}\, \left(e^{i\phi/2} M_{\mathrm{R}} \Sigma_z - e^{-i\phi/2} M_{\mathrm{L}} \Sigma_z \right) \right]. \tag{6.49}$$

6.9.3 Multichannel applications

In the main text we apply our scattering formulation to the quantum spin-Hall edge, which has $N = 1$ channels (counting spin) and $\mathcal{Q} = 1$ Majorana zero-modes (at each NS interface). More generally, the formulas given apply directly to any $N \geq 1$, with the requirement that $N - \mathcal{Q}$ is an even integer. This is a technical requirement, to avoid the difficulty that for $N - \mathcal{Q}$ odd one of the N channels has identically zero Andreev reflection probability at the Fermi level [41]. Here we show how this restriction can be removed, first in terms of the scattering matrix, then in terms of the transfer matrix.

Scattering matrix formulation

We assume a spatial separation of normal-state scattering (described by s_0) and Andreev reflection (described by r_{A}). For $N - \mathcal{Q}$ odd one channel is fully decoupled from the NS interface, so we cannot include it in r_{A}. We are free to choose basis states such that the decoupled channel has the index N (for the left interface) and $2N$ (for the right interface). Our

goal is to determine the reduced unitary scattering matrix $\tilde{s}_0$ that relates the incoming and outgoing electrons in the remaining channels. This is obtained from the relation $\psi^{\text{out}} = s_0\psi^{\text{in}}$ by algebraic elimination of the decoupled components $\psi_N^{\text{out}} = \psi_N^{\text{in}}$ and $\psi_{2N}^{\text{out}} = \psi_{2N}^{\text{in}}$. We thus arrive at

$$\tilde{s}_0 = P^{\mathrm{T}} s_0 [1 - (1 - PP^{\mathrm{T}}) s_0]^{-1} P, \tag{6.50}$$

with the $2N \times (2N-2)$-dimensional matrix

$$P_{nm} = \begin{cases} \delta_{n,m} & \text{if } 1 \le n \le N-1 \\ \delta_{n,m+1} & \text{if } N+1 \le n \le 2N-1 \\ 0 & \text{if } n \in \{N, 2N\} \end{cases}. \tag{6.51}$$

The combination $1 - PP^{\mathrm{T}}$ projects onto the decoupled channels. The remaining channels are Andreev reflected with unit probability, as described by the $2(N-1) \times 2(N-1)$-dimensional unitary matrix r_{A}. All formulas carry through, with the replacement of s_0 by $\tilde{s}_0$.

With appropriately chosen P, this construction extends to cases with multiple decoupled channels, including situations where their number differs at the two interfaces.

Transfer matrix formulation

We again choose a particular set of basis states for incoming and outgoing modes at the left and right interface, such that the decoupled channel has index N and $2N$, respectively. An electron in this channel is reflected as an electron and a hole is reflected as a hole. Therefore these channels do not appear in the $2(N-1) \times 2(N-1)$ electron-to-hole transfer matrices $\tilde{M}_{\mathrm{L}}$ and $\tilde{M}_{\mathrm{R}}$. These relate

$$\tilde{\Psi}_{\mathrm{L,h}} = \tilde{M}_{\mathrm{L}} \tilde{\Psi}_{\mathrm{L,e}}, \quad \tilde{\Psi}_{\mathrm{R,h}} = \tilde{M}_{\mathrm{R}} \tilde{\Psi}_{\mathrm{R,e}}, \tag{6.52}$$

where $\tilde{\Psi}$ differs from Ψ because it does not include the decoupled channel.

When we match wave functions at $x = 0$ we have to take into account that the basis states need not coincide: the basis that decouples the channel from the left interface can be different from the basis that decouples it from the right interface. The matching condition (6.40) thus

contains a pair of $N \times N$ unitary matrices $u_{\text{match}}, v_{\text{match}}$ to change the basis of left-moving and right-moving states,

$$\begin{aligned} \Psi_{\text{R,e}} &= e^{i\phi/2} \begin{pmatrix} u_{\text{match}} & 0 \\ 0 & v_{\text{match}} \end{pmatrix} \Psi_{\text{L,e}}, \\ \Psi_{\text{R,h}} &= e^{-i\phi/2} \begin{pmatrix} u^*_{\text{match}} & 0 \\ 0 & v^*_{\text{match}} \end{pmatrix} \Psi_{\text{L,h}}. \end{aligned} \tag{6.53}$$

The matching matrices $u_{\text{match}}, v_{\text{match}}$ correspond to a $2N \times 2N$ unitary scattering matrix s_{match} that has only transmission blocks,

$$s_{\text{match}} = \begin{pmatrix} 0 & u_{\text{match}} \\ v^\dagger_{\text{match}} & 0 \end{pmatrix}. \tag{6.54}$$

We apply the projection (6.50) to s_{match} to obtain a $2(N-1) \times 2(N-1)$ unitary scattering matrix $\tilde{s}_{\text{match}}$ that does not contain the decoupled channels. We then transform back from scattering matrix $\tilde{s}_{\text{match}}$ to transfer matrix $\tilde{m}_{\text{match}}$, which relates

$$\tilde{\Psi}_{\text{R,e}} = e^{i\phi/2} \tilde{m}_{\text{match}} \Psi_{\text{L,e}}, \quad \tilde{\Psi}_{\text{R,h}} = e^{-i\phi/2} \tilde{m}^*_{\text{match}} \Psi_{\text{L,h}}. \tag{6.55}$$

Unitarity of $\tilde{s}_{\text{match}}$ implies for $\tilde{m}_{\text{match}}$ the condition

$$\tilde{m}^{-1}_{\text{match}} = \Sigma_z \tilde{m}^\dagger_{\text{match}} \Sigma_z. \tag{6.56}$$

Combining Eqs. (6.52) and (6.55) we arrive at

$$e^{i\phi/2} \tilde{M}_{\text{R}} \tilde{m}_{\text{match}} \tilde{\Psi}_{\text{L,e}} = e^{-i\phi/2} \tilde{m}^*_{\text{match}} \tilde{M}_{\text{L}} \tilde{\Psi}_{\text{L,e}}, \tag{6.57}$$

and the corresponding condition for a bound state,

$$\text{Det} \left[e^{i\phi/2} \tilde{M}_{\text{R}} \tilde{m}_{\text{match}} - e^{-i\phi/2} \tilde{m}^*_{\text{match}} \tilde{M}_{\text{L}} \right] = 0. \tag{6.58}$$

We rewrite this using Eq. (6.56) as the determinant of an *antisymmetric* matrix,

$$\text{Det} \left[e^{i\phi/2} \tilde{M}_{\text{R}} \Sigma_z - e^{-i\phi/2} \tilde{m}^*_{\text{match}} \tilde{M}_{\text{L}} \Sigma_z \tilde{m}^\dagger_{\text{match}} \right] = 0. \tag{6.59}$$

We then proceed as in Eqs. (6.46)–(6.49), with M_{R} replaced by $\tilde{M}_{\text{R}}$ and M_{L} replaced by $\tilde{m}^*_{\text{match}} \tilde{M}_{\text{L}} \Sigma_z \tilde{m}^\dagger_{\text{match}} \Sigma_z$.

6.10 Evaluation of the supercurrent along QSHE edge

We apply Eq. (6.33) to the quantum spin-Hall edge. According to Eq. (6.17), we have

$$\nu(i\omega) = -\frac{1}{\pi}\ln\big[2\cos\phi + \zeta_+(\omega) + \zeta_-(\omega)\big], \tag{6.60}$$

$$\zeta_\pm(\omega) = e^{\pm 2\omega/E_{\rm T}}\big(\sqrt{1+\omega^2/\Delta^2} \pm \omega/\Delta\big)^2. \tag{6.61}$$

The Matsubara sum (6.32), with ν_∞ given by Eq. (6.29), takes the form

$$\mathcal{S} = \sum_{p=1}^{\infty}(-1)^p \ln\left[\frac{2\cos\phi + \zeta_+(\Omega_p/2) + \zeta_-(\Omega_p/2)}{(1+\Omega_p^2/\Delta^2)e^{\Omega_p/E_{\rm T}}}\right] \tag{6.62}$$

The function J_∞ is given by Eq. (6.30) and

$$\sigma\sqrt{\mathrm{Det}\, X(0)} = 2\cos(\phi/2), \tag{6.63}$$

in view of Eqs. (6.16) and (6.36).

The superconducting electrodes couple to the quantum spin-Hall edge via a single transverse mode, over a total length $L_{\rm S}$. The corresponding density of states is

$$\rho_{\rm S}(\varepsilon) = \frac{2}{\pi E_{\rm S}}\frac{|\varepsilon|}{\sqrt{\varepsilon^2-\Delta^2}}, \quad |\varepsilon| > \Delta. \tag{6.64}$$

We have defined $E_{\rm S} = \hbar v_{\rm F}/L_{\rm S}$. The superconducting electrodes affect the parity-dependent free energy (6.33) through the factor $e^{J_{\rm S}}$, with

$$\begin{aligned} J_{\rm S} &= \int_\Delta^\infty d\varepsilon\, \rho_{\rm S}(\varepsilon)\ln\tanh(\beta\varepsilon/2) \\ &= -\frac{2\beta}{\pi E_{\rm S}}\int_\Delta^\infty d\varepsilon\, \frac{\sqrt{\varepsilon^2-\Delta^2}}{\sinh\beta\varepsilon}. \end{aligned} \tag{6.65}$$

Collecting results, we arrive at the parity-dependent supercurrent

$$I_\sigma = I_0 - \frac{2e}{\hbar\beta}\frac{d}{d\phi}\ln\tfrac{1}{2}\big[1+\sigma|\cos(\phi/2)|e^{\mathcal{S}+J_\infty+J_{\rm S}}\big], \tag{6.66}$$

$$\sigma = \mathrm{sign}\,[\cos(\phi/2)], \tag{6.67}$$

with I_0 the 2π-periodic supercurrent in the absence of parity constraints,

$$I_0 = \frac{4e}{\hbar\beta}\sin\phi\sum_{p=0}^{\infty}[2\cos\phi+\zeta_+(\omega_p)+\zeta_-(\omega_p)]^{-1}. \tag{6.68}$$

In the long-junction regime $\Delta \gg E_{\rm T}, k_{\rm B}T$ these results reduce to the equations (6.18)–(6.20) given in the main text.

6.10.1 Short-junction limit

As a check on the consistency of the whole formalism, we take the short-junction limit $E_{\rm T}\to\infty$ of the parity-dependent supercurrent (6.66) and see if we recover the results of Fu and Kane [7]. We choose the phase interval $|\phi|<\pi$ and abbreviate

$$u \equiv \tfrac{1}{2}\cos(\phi/2)\beta\Delta. \tag{6.69}$$

The Matsubara sums (6.62) and (6.68) can be evaluated in closed form in the short-junction limit,

$$\begin{aligned}\lim_{E_{\rm T}\to\infty}\mathcal{S} &= \sum_{p=1}^{\infty}(-1)^p\ln\left(\frac{2\cos\phi+2+\Omega_p^2/\Delta^2}{1+\Omega_p^2/\Delta^2}\right)\\ &= \ln\left(\frac{\tanh u}{2\cos(\phi/2)\tanh(\beta\Delta/4)}\right),\end{aligned} \tag{6.70}$$

$$\begin{aligned}\lim_{E_{\rm T}\to\infty} I_0 &= \frac{4e}{\hbar\beta}\sin\phi\sum_{p=0}^{\infty}[2\cos\phi+2+4\omega_p^2/\Delta^2]^{-1}\\ &= \frac{e\Delta}{2\hbar}\sin(\phi/2)\tanh u.\end{aligned} \tag{6.71}$$

In the same limit $J_\infty = \ln\tanh(\beta\Delta/4)$; upon substitution into Eq. (6.66) we arrive at

$$\begin{aligned}I_\pm &= I_0 - \frac{2e}{\hbar\beta}\frac{d}{d\phi}\ln\left(\tfrac{1}{2}\pm\tfrac{1}{2}e^{J_{\rm S}}\tanh u\right)\\ &= -\frac{2e}{\hbar\beta}\frac{d}{d\phi}\ln\left(\cosh u\pm e^{J_{\rm S}}\sinh u\right).\end{aligned} \tag{6.72}$$

In the zero-temperature limit $J_{\rm S}\to 0$ and we recover the result of Ref. 7,

$$\lim_{T\to 0} I_\pm = \mp\frac{2e}{\hbar\beta}\frac{du}{d\phi} = \pm\frac{e\Delta}{2\hbar}\sin(\phi/2). \tag{6.73}$$

The parity dependence at finite temperature can be quantified by the difference $\delta I = \frac{1}{2}(I_+ - I_-)$, for which we find the compact expression

$$\delta I = -\frac{4e}{\hbar\beta}\frac{\tau}{1-\tau^2}\frac{1}{\sinh 2u}\frac{du}{d\phi}, \quad \tau = e^{J_S}\tanh u, \tag{6.74}$$

in agreement with Ref. 13.

6.10.2 Zero-temperature limit in the long-junction regime

Another check on the formalism is provided by the combined zero-temperature and long-junction limits. We again choose the interval $|\phi| < \pi$. The Matsubara sums (6.62) and (6.68) are given in the long-junction limit by

$$\lim_{\Delta\to\infty}\mathcal{S} = \sum_{p=1}^{\infty}(-1)^p \ln\bigl(1 + 2e^{-\Omega_p/E_T}\cos\phi + e^{-2\Omega_p/E_T}\bigr), \tag{6.75}$$

$$\lim_{\Delta\to\infty} I_0 = \frac{2e}{\hbar\beta}\sin\phi\sum_{p=0}^{\infty}\bigl[\cos\phi + \cosh(2\omega_p/E_T)\bigr]^{-1}. \tag{6.76}$$

In the zero-temperature limit the sums may be converted into integrals, with the results

$$\mathcal{S} \to -\ln|2\cos(\phi/2)|, \quad I_0 \to \frac{eE_T}{2\pi\hbar}\phi. \tag{6.77}$$

The two terms J_∞ and J_S both vanish at $T = 0$. Substitution into Eq. (6.66) gives $I_+ = I_0$, in agreement with Eq. (6.3), while I_- remains undetermined. The zero-temperature limit of I_- depends on on higher order terms in the low-temperature expansion of $\mathcal{S}$ that we have not been able to calculate analytically. A numerical calculation (using the Padé approximant built into the `NSum[...,AlternatingSigns]` routine of MATHEMATICA) gives

$$\lim_{T\to 0}\lim_{\Delta\to\infty}\frac{2}{\beta E_T}\ln\left(\tfrac{1}{2} - |\cos(\phi/2)|e^{\mathcal{S}+J_\infty}\right) = |\phi| - \pi, \tag{6.78}$$

resulting in a current I_- in agreement with Eq. (6.3).

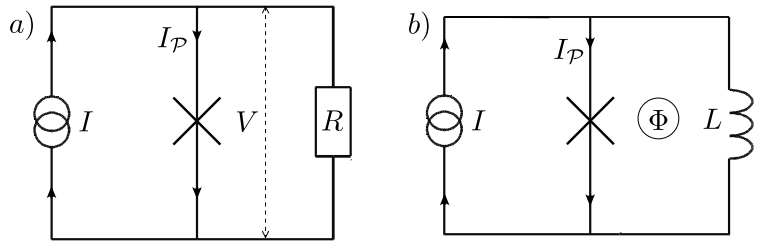

Figure 6.3. Left panel *a*: Circuit of a current-biased, resistively shunted Josephson junction, to measure the current-voltage characteristic. Right panel *b*: Circuit of an rf SQUID to measure the current-phase relationship.

6.11 Circuits to measure the critical current

As explained in the main text, the two circuits shown in Fig. 6.2 (inset) both measure the critical current of the Josephson junction, but their sensitivity to fermion-parity constraints is fundamentally different. A measurement of the current-phase relationship (upper circuit) is insensitive to parity constraints when quasiparticles can enter or leave the system on the time scale of the measurement. This gives the critical current $I_{2\pi,c}$. A measurement of the current-voltage characteristic (lower circuit) remains governed by fermion-parity constraints as long as the quasiparticle tunnelling time τ_{qp} is large compared to the phase relaxation time τ_J of the resistively shunted Josephson junction. This then gives $I_{4\pi,c}$. Here we analyze these two circuits in some more detail.

In the zero-temperature, long-junction limit, we have the 4π-periodic sawtooth current-phase relationship shown in Fig. 6.1 (lower panel). This plot is for an even number of electrons in the system, $\mathcal{P} \equiv (-1)^{\mathcal{N}} = 1$, while for odd parity $\mathcal{P} = -1$ the sawtooth is displaced horizontally by 2π. Both cases are contained in the formula

$$I_{\mathcal{P}}(\phi) = \frac{I_{4\pi,c}}{2\pi} \mathrm{mod}_{4\pi}(\phi + \mathcal{P}\pi + \pi) - I_{4\pi,c}. \tag{6.79}$$

The modulo function is defined by $\mathrm{mod}_{4\pi}(\phi) = \phi - 4\pi n$, with $n \in \mathbb{Z}$ such that $\mathrm{mod}_{4\pi}(\phi) \in [0, 4\pi)$.

We start by considering the current-biased circuit of Fig. 6.3a. A voltage $V = (\hbar/2e)d\phi/dt$ drops over a resistor R in parallel with the Josephson junction, of capacitance C. The two characteristic time scales

of the circuit are the RC time and the phase relaxation time

$$\tau_J = \frac{h}{2e}\frac{1}{RI_{4\pi,c}} = \frac{R_Q}{2R}\frac{\hbar}{E_T}, \tag{6.80}$$

where $R_Q = h/e^2$ is the resistance quantum. The characteristic energy scales of the Josephson junction are the charging energy e^2/C and the Josephson energy $\hbar I_{4\pi,c}/e = E_T$.

The capacitance should be sufficiently small that the phase dynamics is overdamped, $RC \ll \tau_J$, and sufficiently large that the phase dynamics is classical, $e^2/C \ll E_T$. We also wish to ensure that the Josephson junction remains in its ground state during the phase relaxation, which requires $E_T\tau_J/\hbar \gg 1$. Together these three conditions are met if

$$(R/R_Q)^2\tau_J \ll RC \ll \tau_J, \tag{6.81}$$

with $R \ll R_Q$.

At a fixed parity $\mathcal{P}$, the bias current $I = I_{\mathcal{P}} + V/R$ drives the phase $\phi(t)$ according to

$$\frac{I}{I_{4\pi,c}} = \frac{\tau_J}{2\pi}\frac{d\phi}{dt} + \frac{1}{2\pi}\mathrm{mod}_{4\pi}(\phi + \mathcal{P}\pi + \pi) - 1. \tag{6.82}$$

A typical value $E_T/k_B \simeq 1\,\mathrm{K}$ gives $\hbar/E_T \simeq 10^{-11}\,\mathrm{s}$. The typical time scales for quasiparticle poisoning are in the μs to ms range [35], so even if $R \ll R_Q$ we can safely assume that $\tau_J \ll \tau_{qp}$ and use Eq. (6.82) to calculate the relaxation of the phase in between two quasiparticle tunnelling events.

The phase relaxation due to a quasiparticle tunnelling event at $t = 0$ (by which $\mathcal{P} \mapsto -\mathcal{P}$) amounts to a 2π phase slip on a time scale τ_J,

$$\phi(t) = \phi(0)e^{-t/\tau_J} + [\phi(0) + 2\pi](1 - e^{-t/\tau_J}). \tag{6.83}$$

Before and after the phase slip the junction is in a zero-voltage state, for bias currents $I \lesssim I_{4\pi,c}$. During the phase slip there is a voltage pulse of integrated area $\int V(t)dt = h/2e$. The corresponding time-averaged voltage $\bar{V} = h/2e\tau_{qp}$ is smaller by a factor $\tau_J/\tau_{qp} \ll 1$ than the voltage that develops for $I \gtrsim I_{4\pi,c}$.

This shows that the current-biased circuit of Fig. 6.3a provides a DC measurement of the parity-constrained critical current $I_{4\pi,c}$. In contrast, the circuit of Fig. 6.3b is not sensitive to parity constraints. This rf SQUID

is phase-biased for sufficiently small inductance $L \ll h/eI_{4\pi,c}$. Quasiparticle tunnelling events have only a small effect on the phase, which remains fixed by the enclosed flux $\Phi = (\hbar/2e)\phi \approx LI$.

At low temperatures the parity of the number of electrons $\mathcal{N}$ in the system will equilibrate at the ground-state fermion parity σ, which implies that $\mathcal{N}$ is even ($\mathcal{P} = 1$) for $\mathrm{mod}_{4\pi}(\phi + \pi) < 2\pi$ and odd ($\mathcal{P} = -1$) for $\mathrm{mod}_{4\pi}(\phi + \pi) > 2\pi$. In either case the supercurrent $\mathcal{I}_{\mathcal{P}}$ given by Eq. (6.79) cannot become larger than $I_{4\pi,c}/2 = I_{2\pi,c}$ — which is the critical current without parity constraints.

Bibliography

[1] M. Ma and A. Yu. Zyuzin, Europhys. Lett. **21**, 941 (1993).

[2] J. A. M. van Ostaay, A. R. Akhmerov, and C. W. J. Beenakker, Phys. Rev. B **83**, 195441 (2011).

[3] M. Stone and Y. Lin, Phys. Rev. B **83**, 224501 (2011).

[4] P. Rickhaus, M. Weiss, L. Marot, and C. Schönenberger, Nano Lett. **12**, 1942 (2012).

[5] M. Popinciuc, V. E. Calado, X. L. Liu, A. R. Akhmerov, T. M. Klapwijk, and L. M. K. Vandersypen, Phys. Rev. B **85**, 205404 (2012).

[6] K. Komatsu, C. Li, S. Autier-Laurent, H. Bouchiat, and S. Guéron, Phys. Rev. B **86**, 115412 (2012).

[7] L. Fu and C. L. Kane, Phys. Rev. B **79**, 161408(R) (2009).

[8] A. Yu. Kitaev, Phys. Usp. **44** (suppl.), 131 (2001).

[9] H.-J. Kwon, K. Sengupta, and V. M. Yakovenko, Braz. J. Phys. **33**, 653 (2003); Eur. Phys. J. B **37**, 349 (2004).

[10] A. A. Golubov, M. Y. Kupriyanov, and E. Ilichev, Rev. Mod. Phys. **76**, 411 (2004).

[11] R. M. Lutchyn, J. D. Sau, and S. Das Sarma, Phys. Rev. Lett. **105**, 077001 (2010).

[12] K. T. Law and P. A. Lee, Phys. Rev. B **84**, 081304 (2011).

[13] P. A. Ioselevich and M. V. Feigel'man, Phys. Rev. Lett. **106**, 077003 (2011).

[14] F. S. Nogueira and I. Eremin, J. Phys. Condens. Matter **24** 325701 (2012).

[15] D. M. Badiane, M. Houzet, and J. S. Meyer, Phys. Rev. Lett. **107**, 177002 (2011).

[16] P. San-Jose, E. Prada, and R. Aguado, Phys. Rev. Lett. **108**, 257001 (2012).

[17] F. Domínguez, F. Hassler, and G. Platero, Phys. Rev. B **86**, 140503(R) (2012).

[18] D. I. Pikulin and Yu. V. Nazarov, Phys. Rev. B **86**, 140504(R) (2012).

[19] M. König, H. Buhmann, L. W. Molenkamp, T. Hughes, C.-X. Liu, X.-L. Qi, and S.-C. Zhang, J. Phys. Soc. Jpn. **77**, 031007 (2008).

[20] C. W. J. Beenakker and H. van Houten, Phys. Rev. Lett. **66**, 3056 (1991); extended version at arXiv:cond-mat/0512610.

[21] It is a pervasive misunderstanding that the factor $g = 2$ in the relation (6.1) between supercurrent and Andreev levels accounts for the charge $2e$ of the Cooper pairs, rather than counting the spin degeneracy. Because of this misunderstanding, the results for the supercurrent carried by Majorana zero-modes (which have $g = 1$) should be divided by two in Ref. 9 and many follow-up papers. The origin of the misunderstanding is discussed in more detail by N. M. Chtchelkatchev and Yu. V. Nazarov, Phys. Rev. Lett. **90**, 226806 (2003).

[22] C. Ishii, Prog. Theor. Phys. (Kyoto) **44**, 1525 (1970).

[23] J. Bardeen and J. L. Johnson, Phys. Rev. B **5**, 72 (1972).

[24] A. V. Svidzinsky, T. N. Antsygina, and E. N. Bratus, J. Low Temp. Phys. **10**, 131 (1973).

[25] C. W. J. Beenakker, Phys. Rev. Lett. **67**, 3836 (1991); extended version at arXiv:cond-mat/0406127.

[26] M. T. Tuominen, J. M. Hergenrother, T. S. Tighe, and M. Tinkham, Phys. Rev. Lett. **69**, 1997 (1992).

[27] The factor of two in the relation (6.6) between supercurrent and free energy accounts for the Cooper pair charge, with all degeneracies included in the partition function. Please see Ref. 21 to avoid any misunderstanding.

[28] P. W. Brouwer and C. W. J. Beenakker, Chaos, Solitons & Fractals **8**, 1249 (1997). Several misprints are corrected in the online version at arXiv:cond-mat/9611162.

[29] Details of the calculations are given in the Appendices.

[30] The basis chosen for the Bogoliubov-De Gennes Hamiltonian (6.15) is {spin-up electron, spin-down electron, spin-up hole, spin-down hole}. In this basis the electron and hole blocks of H_{BdG} are minus each others complex conjugate and the electron and hole scattering matrices s_{ee}, s_{hh} are related by $s^*_{hh}(-\varepsilon) = s_{ee}(\varepsilon) \equiv s_0(\varepsilon)$. Similarly, the Andreev reflection matrices s_{he}, s_{eh} from electron to hole and from hole to electron are related by $s^*_{eh}(-\varepsilon) = s_{he}(\varepsilon) \equiv r_{\mathrm{A}}(\varepsilon)$.

[31] M. König, S. Wiedmann, C. Brüne, A. Roth, H. Buhmann, L. W. Molenkamp, X.-L. Qi, and S.-C. Zhang, Science **318**, 766 (2007).

[32] I. Knez, R.-R. Du, and G. Sullivan, Phys. Rev. Lett. **107**, 136603 (2011).

[33] I. Knez, R.-R. Du, and G. Sullivan, Phys. Rev. Lett. **109**, 186603 (2012).

[34] L. P. Rokhinson, X. Liu, and J. K. Furdyna, Nature Phys. **8**, 795 (2012) .

[35] D. Rainis and D. Loss, Phys. Rev. B **85**, 174533 (2012).

[36] V. Mourik, K. Zuo, S. M. Frolov, S. R. Plissard, E. P. A. M. Bakkers, and L. P. Kouwenhoven, Science **336**, 1003 (2012).

[37] M. T. Deng, C. L. Yu, G. Y. Huang, M. Larsson, P. Caroff, and H. Q. Xu, Nano Lett. **12**, 6414 (2012).

[38] A. Das, Y. Ronen, Y. Most, Y. Oreg, M. Heiblum, and H. Shtrikman, Nature Phys. **8**, 887 (2012).

[39] S. Ryu, A. Schnyder, A. Furusaki, and A. Ludwig, New J. Phys. **12**, 065010 (2010).

[40] A. R. Akhmerov, J. P. Dahlhaus, F. Hassler, M. Wimmer, and C.W.J. Beenakker, Phys. Rev. Lett. **106**, 057001 (2011).

[41] M. Diez, J. P. Dahlhaus, M. Wimmer, and C. W. J. Beenakker, Phys. Rev. B **86**, 094501 (2012).

Chapter 7

Nernst effect beyond the relaxation-time approximation

7.1 Introduction

The Nernst effect is a magneto-thermo-electric effect, in which an electric field E_x in the x-direction results from a temperature gradient $\partial T/\partial y$ in the y-direction, in the presence of a (weak) magnetic field B in the z-direction. [1] The Nernst coefficient $\mathcal{N}_{xy} = -E_x(B\partial T/\partial y)^{-1}$ depends sensitively on anisotropies in the band structure. In particular, for a square lattice $\mathcal{N}_{xy} = -\mathcal{N}_{yx}$ is antisymmetric upon interchange of x and y — just like the Hall resistivity — but lattice distortion breaks this antisymmetry.

There has been much recent interest in the Nernst effect in the context of high-T_c superconductivity, since underdoped cuprates were found to have an unusually large Nernst coefficient in the normal state. [2] This may be due to superconducting fluctuations above T_c, [3, 4] chirality of the ground state,[5] or it may be purely a quasiparticle effect. [6] The quasiparticle Nernst effect has been studied on the basis of the linearized Boltzmann equation in the relaxation-time approximation.[7–13] This is a reliable approach if the scattering rate is isotropic, since then the neglected "scattering-in" contributions average out to zero. There is, however, considerable experimental evidence for predominantly small-angle elastic scattering in the cuprates, [14–17] possibly due to long-range potential fluctuations from dopant atoms in between the CuO_2 planes.[18, 19]

It is not surprising that existing studies rely on the relaxation-time approximation, since the full solution of the Boltzmann equation with both band and scattering anisotropies is a notoriously difficult problem. [20] In our literature search we have found magneto-electric calculations that go beyond the relaxation-time approximation,[21–24] but no magneto-thermo-electric studies. It is the purpose of this paper to provide such a calculation and to assess the reliability of the relaxation-time approximation.

We start in Sec. 7.2 with a formulation of the anisotropic transport problem, in terms of the socalled vector mean free path. [25, 26] In the relaxation-time approximation, this vector $\mathbf{\Lambda}_{\boldsymbol{k}}$ is simply given by the product $v_{\boldsymbol{k}}\tau_{\boldsymbol{k}}$ of velocity and scattering time (all quantities dependent on the point $\boldsymbol{k}$ on the Fermi surface). Going beyond this approximation, $\mathbf{\Lambda}_{\boldsymbol{k}}$ is determined by an integral equation, which we solve numerically.

We also consider, in Sec. 7.3, an improvement on the relaxation-time approximation, due to Ziman, [20, 27] which incorporates some of the scattering-in contributions into the definition of the scattering time. For isotropic Fermi surfaces Ziman's scattering time is just the familiar transport mean free time — which fully accounts for scattering anisotropies. If the dispersion relation is not isotropic this is no longer the case.

We compare the exact and approximate solutions in Sec. 7.4 and conclude in Sec. 7.5.

7.2 Formulation of the transport problem

7.2.1 Boltzmann equation

We start from the semiclassical Boltzmann transport equation for quasiparticles (charge e) in a weak magnetic field $\boldsymbol{B}$, driven out of equilibrium by a spatially uniform electric field $\boldsymbol{E}$ and temperature gradient ∇T. The excitation energy is $\varepsilon_{\boldsymbol{k}}$, relative to the Fermi energy ε_F. The band structure may be anisotropic, so that the velocity

$$v_{\boldsymbol{k}} = \hbar^{-1}\nabla_{\boldsymbol{k}}\varepsilon_{\boldsymbol{k}} \tag{7.1}$$

(with $\nabla_{\boldsymbol{k}} = \partial/\partial\boldsymbol{k}$) need not be parallel to the momentum $\hbar\boldsymbol{k}$. For simplicity, we assume there is only a single type of carriers at the Fermi level (either electrons or holes).

Upon linearization of the distribution function $f_{\boldsymbol{k}} = f_0 + g_{\boldsymbol{k}}$ around the equilibrium solution

$$f_0 = \frac{1}{1 + \exp[(\varepsilon_{\boldsymbol{k}} - \varepsilon_F)/k_B T]}, \tag{7.2}$$

the Boltzmann equation takes the form [20]

$$\boldsymbol{v}_{\boldsymbol{k}} \cdot \boldsymbol{U} - \frac{e}{\hbar}(\boldsymbol{v}_{\boldsymbol{k}} \times \boldsymbol{B}) \cdot \nabla_{\boldsymbol{k}} g_{\boldsymbol{k}} = \sum_{\boldsymbol{k}'} Q(\boldsymbol{k}, \boldsymbol{k}')(g_{\boldsymbol{k}} - g_{\boldsymbol{k}'}), \tag{7.3}$$

$$\boldsymbol{U} = \left(e\boldsymbol{E} - \frac{\varepsilon_{\boldsymbol{k}} - \varepsilon_F}{T} \nabla T \right) \left(-\frac{\partial f_0}{\partial \varepsilon_{\boldsymbol{k}}} \right). \tag{7.4}$$

The right-hand-side of Eq. (7.3) is the difference between the scattering-in term $\sum_{\boldsymbol{k}'} Q(\boldsymbol{k}, \boldsymbol{k}') g_{\boldsymbol{k}'}$ and the scattering-out term $\sum_{\boldsymbol{k}'} Q(\boldsymbol{k}', \boldsymbol{k}) g_{\boldsymbol{k}}$ (with $Q(\boldsymbol{k}', \boldsymbol{k}) = Q(\boldsymbol{k}, \boldsymbol{k}')$ because of detailed balance).

We assume elastic scattering with rate

$$Q(\boldsymbol{k}, \boldsymbol{k}') = \delta(\varepsilon_{\boldsymbol{k}} - \varepsilon_{\boldsymbol{k}'}) q(\boldsymbol{k}, \boldsymbol{k}') \tag{7.5}$$

from $\boldsymbol{k}'$ to $\boldsymbol{k}$. Detailed balance requires

$$q(\boldsymbol{k}', \boldsymbol{k}) = q(\boldsymbol{k}, \boldsymbol{k}') \tag{7.6}$$

and particle conservation requires

$$\sum_{\boldsymbol{k}} g_{\boldsymbol{k}} = 0. \tag{7.7}$$

The sum over $\boldsymbol{k}$ represents a d-dimensional momentum integral, $\sum_{\boldsymbol{k}} \to (2\pi)^{-d} \int d\boldsymbol{k}$ (in a unit volume). The spin degree of freedom is omitted.

It is convenient to define the Fermi surface average

$$\langle f(\boldsymbol{k}) \rangle_{S_F} = \frac{\oint dS_F \, f(\boldsymbol{k}) |\boldsymbol{v}_{\boldsymbol{k}}|^{-1}}{\oint dS_F \, |\boldsymbol{v}_{\boldsymbol{k}}|^{-1}}, \tag{7.8}$$

with a weight factor $|v_{\boldsymbol{k}}|^{-1}$ from the volume element $d\boldsymbol{k} = \hbar^{-1} |v_{\boldsymbol{k}}|^{-1} d\varepsilon_{\boldsymbol{k}} dS_F$. The density of states is given by

$$N(\varepsilon_F) = \hbar^{-1} (2\pi)^{-d} \oint dS_F \, |\boldsymbol{v}_{\boldsymbol{k}}|^{-1}. \tag{7.9}$$

For later use we note the identity

$$\langle f(\boldsymbol{k})(\boldsymbol{v}_{\boldsymbol{k}} \times \nabla_{\boldsymbol{k}}) g(\boldsymbol{k}) \rangle_{S_F} = -\langle g(\boldsymbol{k})(\boldsymbol{v}_{\boldsymbol{k}} \times \nabla_{\boldsymbol{k}}) f(\boldsymbol{k}) \rangle_{S_F}, \tag{7.10}$$

valid for arbitrary functions f, g of $\boldsymbol{k}$.

7.2.2 Vector mean free paths

We seek the solution of Eq. (7.3) to first order in B. Following Refs. 25, 26 we introduce the vector mean free paths $\boldsymbol{\Lambda}_{\boldsymbol{k}}$ (of order B^0) and $\delta\boldsymbol{\Lambda}_{\boldsymbol{k}}$ (of order B^1), by substituting

$$g_{\boldsymbol{k}} = \boldsymbol{U} \cdot (\boldsymbol{\Lambda}_{\boldsymbol{k}} + \delta\boldsymbol{\Lambda}_{\boldsymbol{k}}) \,. \tag{7.11}$$

Since the vector $\boldsymbol{U}$ can have an arbitrary direction it cancels from the equation for $\boldsymbol{\Lambda}_{\boldsymbol{k}}$. The equation for $\delta\boldsymbol{\Lambda}_{\boldsymbol{k}}$ has also a term $\propto (\boldsymbol{v}_{\boldsymbol{k}} \times \nabla_{\boldsymbol{k}})\boldsymbol{U}$, which vanishes because $\nabla_{\boldsymbol{k}}\boldsymbol{U} = \hbar \boldsymbol{v}_{\boldsymbol{k}} \partial \boldsymbol{U}/\partial\varepsilon_{\boldsymbol{k}}$.

The resulting equations for the vector mean free paths are

$$\sum_{\boldsymbol{k}'} Q(\boldsymbol{k},\boldsymbol{k}')(\boldsymbol{\Lambda}_{\boldsymbol{k}} - \boldsymbol{\Lambda}_{\boldsymbol{k}'}) = \boldsymbol{v}_{\boldsymbol{k}}, \tag{7.12}$$

$$\sum_{\boldsymbol{k}'} Q(\boldsymbol{k},\boldsymbol{k}')(\delta\boldsymbol{\Lambda}_{\boldsymbol{k}} - \delta\boldsymbol{\Lambda}_{\boldsymbol{k}'}) = \frac{e}{\hbar}\boldsymbol{B} \cdot (\boldsymbol{v}_{\boldsymbol{k}} \times \nabla_{\boldsymbol{k}})\boldsymbol{\Lambda}_{\boldsymbol{k}}. \tag{7.13}$$

They can be written in terms of Fermi surface averages,

$$N(\varepsilon_F)\langle q(\boldsymbol{k},\boldsymbol{k}')(\boldsymbol{\Lambda}_{\boldsymbol{k}} - \boldsymbol{\Lambda}_{\boldsymbol{k}'})\rangle_{S'_F} = \boldsymbol{v}_{\boldsymbol{k}}, \tag{7.14}$$

$$N(\varepsilon_F)\langle q(\boldsymbol{k},\boldsymbol{k}')(\delta\boldsymbol{\Lambda}_{\boldsymbol{k}} - \delta\boldsymbol{\Lambda}_{\boldsymbol{k}'})\rangle_{S'_F} = \frac{e}{\hbar}\boldsymbol{B} \cdot (\boldsymbol{v}_{\boldsymbol{k}} \times \nabla_{\boldsymbol{k}})\boldsymbol{\Lambda}_{\boldsymbol{k}}. \tag{7.15}$$

(The prime in the subscript S'_F indicates that $\boldsymbol{k}'$ is averaged over the Fermi surface, at fixed $\boldsymbol{k}$.) The solution should satisfy the normalization

$$\langle \boldsymbol{\Lambda}_{\boldsymbol{k}} \rangle_{S_F} = 0 = \langle \boldsymbol{\delta\Lambda}_{\boldsymbol{k}} \rangle_{S_F}, \tag{7.16}$$

required by particle conservation to each order in B.

The integral equations (7.12) and (7.13) can be readily solved numerically. In the limit of small-angle scattering an analytical solution is possible, by expanding the $\boldsymbol{k}'$-dependence around $\boldsymbol{k}$ to second order, [28, 29] but we have not pursued that method here.

7.2.3 Linear response coefficients

In linear response the electric current density $\boldsymbol{j}$ is related to the electric field $\boldsymbol{E}$ and temperature gradient ∇T by

$$\boldsymbol{j} = \boldsymbol{\sigma}\boldsymbol{E} - \boldsymbol{\alpha}\nabla T. \tag{7.17}$$

The conductivity tensor $\boldsymbol{\sigma}$ follows from the vector mean free paths by

$$\begin{aligned}\boldsymbol{\sigma} &= \sum_{\boldsymbol{k}} e\boldsymbol{v}_{\boldsymbol{k}} \otimes \frac{\partial g_{\boldsymbol{k}}}{\partial \boldsymbol{E}} \\ &= e^2 \sum_{\boldsymbol{k}} \left(-\frac{\partial f_0}{\partial \varepsilon_{\boldsymbol{k}}} \right) \boldsymbol{v}_{\boldsymbol{k}} \otimes (\boldsymbol{\Lambda}_{\boldsymbol{k}} + \delta\boldsymbol{\Lambda}_{\boldsymbol{k}}) \,. \end{aligned} \tag{7.18}$$

[The direct product indicates a dyadic tensor with elements $(\boldsymbol{a} \otimes \boldsymbol{b})_{ij} = a_i b_j$.]

At low temperatures, when $-\partial f_0/\partial \varepsilon_{\boldsymbol{k}} \to \delta(\varepsilon_{\boldsymbol{k}} - \varepsilon_F)$, this may also be written as a Fermi surface average,

$$\boldsymbol{\sigma} = e^2 N(\varepsilon_F) \langle \boldsymbol{v}_{\boldsymbol{k}} \otimes (\boldsymbol{\Lambda}_{\boldsymbol{k}} + \delta\boldsymbol{\Lambda}_{\boldsymbol{k}}) \rangle_{S_F}. \tag{7.19}$$

By substituting Eq. (7.14) for $\boldsymbol{v}_{\boldsymbol{k}}$ and using Eq. (7.15) together with the detailed balance condition (7.6) and the identity (7.10), one verifies the Onsager reciprocity relation

$$\sigma_{ij}(\boldsymbol{B}) = \sigma_{ji}(-\boldsymbol{B}). \tag{7.20}$$

The thermoelectric tensor $\boldsymbol{\alpha}$ is given by

$$\begin{aligned}\boldsymbol{\alpha} &= \sum_{\boldsymbol{k}} e\boldsymbol{v}_{\boldsymbol{k}} \otimes \frac{\partial g_{\boldsymbol{k}}}{\partial(-\nabla T)} \\ &= \frac{e}{T} \sum_{\boldsymbol{k}} (\varepsilon_{\boldsymbol{k}} - \varepsilon_F) \left(-\frac{\partial f_0}{\partial \varepsilon_{\boldsymbol{k}}} \right) \boldsymbol{v}_{\boldsymbol{k}} \otimes (\boldsymbol{\Lambda}_{\boldsymbol{k}} + \delta\boldsymbol{\Lambda}_{\boldsymbol{k}}) \,. \end{aligned} \tag{7.21}$$

At low temperatures this reduces to the Mott formula,

$$\boldsymbol{\alpha} = -\frac{\pi^2 k_B^2 T}{3e} \frac{d}{d\varepsilon_F} \boldsymbol{\sigma}. \tag{7.22}$$

These equations all refer to a single type of carriers at the Fermi level (electrons or holes), as would be appropriate for hole-doped cuprates. The ambipolar effects of coexisting electron and hole bands are not considered here.

7.2.4 Nernst effect

We take a two-dimensional ($d = 2$) layered geometry in the $x - y$ plane, with a magnetic field $\boldsymbol{B} = B\hat{z}$ in the z-direction. The Nernst effect relates a transverse electric field, say in the x-direction, to a longitudinal temperature gradient (in the y-direction), for zero electric current.

One distinguishes the isothermal and adiabatic Nernst effect, [1] depending on whether $\partial T/\partial x = 0$ or $j_{h,x} = 0$ is enforced (with $\boldsymbol{j}_h$ the heat current). As is appropriate for the cuprates, [30] we assume that a high phonon contribution to the thermal conductivity keeps the transverse temperature gradient $\partial T/\partial x$ negligibly small, so that the Nernst effect is measured under isothermal conditions.

The isothermal Nernst effect is expressed by

$$E_x = \theta_{xy}\left(-\frac{\partial T}{\partial y}\right), \quad \frac{\partial T}{\partial x} = 0, \quad \boldsymbol{j}_e = 0, \tag{7.23}$$

and similarly with x and y interchanged. The thermopower tensor

$$\boldsymbol{\theta} = -\boldsymbol{\sigma}^{-1}\boldsymbol{\alpha} \tag{7.24}$$

has off-diagonal elements

$$\theta_{xy} = -\frac{\sigma_{yy}\alpha_{xy} - \sigma_{xy}\alpha_{yy}}{\sigma_{xx}\sigma_{yy} - \sigma_{xy}\sigma_{yx}}, \tag{7.25a}$$

$$\theta_{yx} = -\frac{\sigma_{xx}\alpha_{yx} - \sigma_{yx}\alpha_{xx}}{\sigma_{xx}\sigma_{yy} - \sigma_{xy}\sigma_{yx}}. \tag{7.25b}$$

We will consider two-dimensional anisotropic band structures that still possess at least one axis of reflection symmetry, say the y-axis. Upon reflection the component $j_x \mapsto -j_x$ of the electric current changes sign, while E_y and $\partial T/\partial y$ remain unchanged. The perpendicular magnetic field $B \mapsto -B$ also changes sign, because it is an axial vector. It follows that $\sigma_{xy}(B) = -\sigma_{xy}(-B)$ and $\alpha_{xy}(B) = -\alpha_{xy}(-B)$ are both odd functions of B, so they vanish when $B \to 0$.

Using the Mott formula (7.22), one can then define the B-independent Nernst coefficients

$$\begin{aligned}\mathcal{N}_{xy} &= \lim_{B\to 0} \theta_{xy}/B \\ &= \frac{\pi^2 k_B^2 T}{3e} \lim_{B\to 0} \frac{1}{B\sigma_{xx}} \left(\frac{d\sigma_{xy}}{d\varepsilon_F} - \frac{\sigma_{xy}}{\sigma_{yy}}\frac{d\sigma_{yy}}{d\varepsilon_F}\right) \\ &= \frac{\pi^2 k_B^2 T}{3e} \lim_{B\to 0} \frac{1}{B}\frac{\sigma_{yy}}{\sigma_{xx}}\frac{d}{d\varepsilon_F}\frac{\sigma_{xy}}{\sigma_{yy}},\end{aligned} \tag{7.26a}$$

$$\mathcal{N}_{yx} = -\frac{\pi^2 k_B^2 T}{3e} \lim_{B\to 0} \frac{1}{B}\frac{\sigma_{xx}}{\sigma_{yy}}\frac{d}{d\varepsilon_F}\frac{\sigma_{xy}}{\sigma_{xx}}. \tag{7.26b}$$

These expressions relate the Nernst coefficients to the energy derivative of the Hall angle in the small magnetic-field limit. The cancellation in Eq. (7.26a) of any identical energy dependence of σ_{xy} and σ_{yy} is known as the Sondheimer cancellation.[6, 31] On a square lattice one has $\sigma_{xx} = \sigma_{yy}$, hence $\mathcal{N}_{xy} = -\mathcal{N}_{yx}$, but without this C_4 symmetry the two Nernst coefficients differ in absolute value.

In terms of the vector mean free paths, the Nernst coefficients are given by

$$\mathcal{N}_{xy} = \frac{\pi^2 k_B^2 T}{3eB} \frac{\langle v_{\boldsymbol{k},y} \Lambda_{\boldsymbol{k},y} \rangle_{S_F}}{\langle v_{\boldsymbol{k},x} \Lambda_{\boldsymbol{k},x} \rangle_{S_F}} \frac{d}{d\varepsilon_F} \frac{\langle v_{\boldsymbol{k},x} \delta\Lambda_{\boldsymbol{k},y} \rangle_{S_F}}{\langle v_{\boldsymbol{k},y} \Lambda_{\boldsymbol{k},y} \rangle_{S_F}}, \tag{7.27a}$$

$$\mathcal{N}_{yx} = -\frac{\pi^2 k_B^2 T}{3eB} \frac{\langle v_{\boldsymbol{k},x} \Lambda_{\boldsymbol{k},x} \rangle_{S_F}}{\langle v_{\boldsymbol{k},y} \Lambda_{\boldsymbol{k},y} \rangle_{S_F}} \frac{d}{d\varepsilon_F} \frac{\langle v_{\boldsymbol{k},y} \delta\Lambda_{\boldsymbol{k},x} \rangle_{S_F}}{\langle v_{\boldsymbol{k},x} \Lambda_{\boldsymbol{k},x} \rangle_{S_F}}, \tag{7.27b}$$

where we have used that $\boldsymbol{\Lambda}_{\boldsymbol{k}}$ is B-independent and $\delta\boldsymbol{\Lambda}_{\boldsymbol{k}}$ is $\propto B$.

7.3 Relaxation-time approximation

In the relaxation-time approximation the scattering-in term $\sum_{k'} Q(\boldsymbol{k}, \boldsymbol{k}') g_{k'}$ on the right-hand-side of the Boltzmann equation (7.3) is omitted. [20] Only the scattering-out term $g_{\boldsymbol{k}} \sum_{k'} Q(\boldsymbol{k}, \boldsymbol{k}') = g_{\boldsymbol{k}} / \tau_{\boldsymbol{k}}$ is retained, containing the momentum dependent relaxation rate

$$1/\tau_{\boldsymbol{k}} = \sum_{\boldsymbol{k}'} Q(\boldsymbol{k}, \boldsymbol{k}') = N(\varepsilon_F) \langle q(\boldsymbol{k}, \boldsymbol{k}') \rangle_{S'_F}. \tag{7.28}$$

Without the scattering-in term, the equations (7.12) and (7.13) for the vector mean free paths can be solved immediately,

$$\boldsymbol{\Lambda}_{\boldsymbol{k}} = \boldsymbol{v}_{\boldsymbol{k}} \tau_{\boldsymbol{k}}, \quad \delta\boldsymbol{\Lambda}_{\boldsymbol{k}} = \frac{e}{\hbar} \tau_{\boldsymbol{k}} \boldsymbol{B} \cdot (\boldsymbol{v}_{\boldsymbol{k}} \times \nabla_{\boldsymbol{k}}) \tau_{\boldsymbol{k}} \boldsymbol{v}_{\boldsymbol{k}}. \tag{7.29}$$

In general this solution does not satisfy the particle conservation requirement (7.16), which is the fundamental deficiency of the relaxation-time approximation.

Substitution into Eq. (7.19) gives the conductivity tensor

$$\boldsymbol{\sigma} = e^2 N(\varepsilon_F) \langle \tau_{\boldsymbol{k}} \boldsymbol{v}_{\boldsymbol{k}} \otimes (\boldsymbol{v}_{\boldsymbol{k}} + \Omega_{\boldsymbol{k}} \tau_{\boldsymbol{k}} \boldsymbol{v}_{\boldsymbol{k}}) \rangle_{S_F}, \tag{7.30}$$

with differential operator

$$\Omega_{\boldsymbol{k}} = \frac{e}{\hbar} \boldsymbol{B} \cdot (\boldsymbol{v}_{\boldsymbol{k}} \times \nabla_{\boldsymbol{k}}). \tag{7.31}$$

For a two-dimensional lattice with reflection symmetry in the y-axis, the elements of the conductivity tensor are given by

$$\sigma_{xx} = e^2 N(\varepsilon_F) \langle \tau v_x^2 \rangle_{S_F}, \quad \sigma_{yy} = e^2 N(\varepsilon_F) \langle \tau v_y^2 \rangle_{S_F}, \tag{7.32}$$

$$\sigma_{xy} = -\sigma_{yx} = e^2 N(\varepsilon_F) \frac{eB}{\hbar} \times \left\langle \tau v_x \left(v_x \frac{\partial}{\partial k_y} - v_y \frac{\partial}{\partial k_x} \right) \tau v_y \right\rangle_{S_F}. \tag{7.33}$$

(Here we don't write the subscript $\boldsymbol{k}$ to simplify the notation.) The Nernst coefficients in the relaxation-time approximation then follow from Eq. (7.26) as the energy derivative of the ratio of two Fermi surface averages,

$$\mathcal{N}_{xy} = Z_0 \frac{\sigma_{yy}}{\sigma_{xx}} \frac{d}{d\varepsilon_F} \frac{\left\langle \tau v_x \left(v_x \frac{\partial}{\partial k_y} - v_y \frac{\partial}{\partial k_x} \right) \tau v_y \right\rangle_{S_F}}{\langle \tau v_y^2 \rangle_{S_F}}, \tag{7.34a}$$

$$\mathcal{N}_{yx} = -Z_0 \frac{\sigma_{xx}}{\sigma_{yy}} \frac{d}{d\varepsilon_F} \frac{\left\langle \tau v_x \left(v_x \frac{\partial}{\partial k_y} - v_y \frac{\partial}{\partial k_x} \right) \tau v_y \right\rangle_{S_F}}{\langle \tau v_x^2 \rangle_{S_F}}, \tag{7.34b}$$

where we have defined

$$Z_0 = \frac{\pi^2 k_B^2 T}{3\hbar}. \tag{7.35}$$

One may further simplify the relaxation-time approximation by taking an isotropic relaxation time $\tau_0(\varepsilon_F)$, which is the approach taken in Refs. 9–13. Since $(\boldsymbol{v}_{\boldsymbol{k}} \times \nabla_{\boldsymbol{k}}) \tau_0(\varepsilon_F) = 0$, Eq. (7.34) then reduces to

$$\mathcal{N}_{xy} = Z_0 \frac{\sigma_{yy}}{\sigma_{xx}} \frac{d}{d\varepsilon_F} \frac{\tau_0(\varepsilon_F)}{\langle v_y^2 \rangle_{S_F}} \left\langle v_x^2 \frac{\partial v_y}{\partial k_y} - v_x v_y \frac{\partial v_y}{\partial k_x} \right\rangle_{S_F}, \tag{7.36a}$$

$$\mathcal{N}_{yx} = -Z_0 \frac{\sigma_{xx}}{\sigma_{yy}} \frac{d}{d\varepsilon_F} \frac{\tau_0(\varepsilon_F)}{\langle v_x^2 \rangle_{S_F}} \left\langle v_x^2 \frac{\partial v_y}{\partial k_y} - v_x v_y \frac{\partial v_y}{\partial k_x} \right\rangle_{S_F}. \tag{7.36b}$$

If one stays with a momentum dependent relaxation time $\tau_{\boldsymbol{k}}$, then it is possible to improve on the relaxation-time approximation by changing the definition (7.28) into Ziman's expression [20, 27]

$$1/\tau_{\boldsymbol{k}}^{\text{Ziman}} = N(\varepsilon_F) \left\langle q(\boldsymbol{k}, \boldsymbol{k}') \left(1 - \frac{\boldsymbol{v}_{\boldsymbol{k}} \cdot \boldsymbol{v}_{\boldsymbol{k}'}}{|\boldsymbol{v}_{\boldsymbol{k}}| \, |\boldsymbol{v}_{\boldsymbol{k}'}|} \right) \right\rangle_{S_F'}. \tag{7.37}$$

Ziman's improvement of the relaxation-time approximation becomes exact if the Fermi surface is isotropic, meaning that $\varepsilon_{\boldsymbol{k}}$ is only a function of $|\boldsymbol{k}|$ and $q(\boldsymbol{k}, \boldsymbol{k}')$ is only a function of $\boldsymbol{k} \cdot \boldsymbol{k}'$.

7.4 Comparison

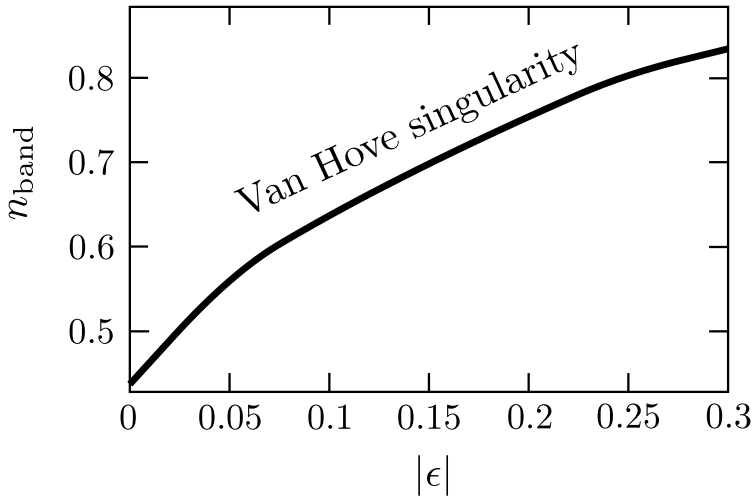

Figure 7.1. Band filling at which the dispersion relation (7.42) has a Van Hove singularity at the Fermi level, as a function of lattice distortion.

We turn to a comparison of the Nernst effect in relaxation-time approximation with the exact solution of the linearized Boltzmann equation. For this comparison we need to specify an elastic scattering rate $Q(\boldsymbol{k},\boldsymbol{k}') = \delta(\varepsilon_{\boldsymbol{k}} - \varepsilon_{\boldsymbol{k}'})q(\boldsymbol{k},\boldsymbol{k}')$ and a dispersion relation $\varepsilon_{\boldsymbol{k}}$.

For the scattering, we take a random impurity potential with range ξ. By increasing ξ relative to the Fermi wave length, we can study the transition from isotropic scattering to (small-angle) forward scattering. We model the impurity potential by a sum of Gaussians, centered at the random positions $\boldsymbol{r}_i$ of the impurities,

$$U(\boldsymbol{r}) = \sum_i U_i \exp\left(-\frac{|\boldsymbol{r}-\boldsymbol{r}_i|^2}{\xi^2}\right). \tag{7.38}$$

The amplitude U_i is uniformly distributed in $[-\delta,\delta]$. The correlator is

$$\langle U(\boldsymbol{r})U(\boldsymbol{r}')\rangle = \frac{\pi}{6}\delta^2\xi^2 n_{\mathrm{imp}} \exp\left(-\frac{|\boldsymbol{r}-\boldsymbol{r}'|^2}{2\xi^2}\right), \tag{7.39}$$

$$\Rightarrow \langle |U(\boldsymbol{k})|^2\rangle = \tfrac{1}{12}\delta^2\xi^4 n_{\mathrm{imp}} \exp\left(-\tfrac{1}{2}\xi^2|\boldsymbol{k}|^2\right), \tag{7.40}$$

where $n_{\rm imp}$ is the two-dimensional impurity density (number of impurities per area per layer). The resulting elastic scattering rate (in Born approximation) becomes

$$q(\boldsymbol{k},\boldsymbol{k}') = \gamma_0 \exp\left(-\tfrac{1}{2}\xi^2|\boldsymbol{k}-\boldsymbol{k}'|^2\right),$$
$$\gamma_0 = \frac{\pi\delta^2\xi^4 n_{\rm imp}}{6\hbar}. \tag{7.41}$$

Values of ξ/a of order unity are to be expected in the cuprates for scattering by impurities between the CuO_2 planes, when ξ is of the order of the interplane distance.

For the dispersion relation we follow a recent study of the Nernst effect in hole-doped cuprates, [10] by taking the tight-binding dispersion of a distorted square lattice with first (t_1), second (t_2), and third (t_3) nearest-neigbor hopping:

$$\begin{aligned} E(\boldsymbol{k}) = & -2t_1\big[(1+\epsilon)\cos k_x + (1-\epsilon)\cos k_y\big] \\ & -2t_3\big[(1+\epsilon)\cos 2k_x + (1-\epsilon)\cos 2k_y\big] \\ & +4t_2\cos k_x \cos k_y. \end{aligned} \tag{7.42}$$

The lattice constant is a and $\boldsymbol{k}$ is measured in units of $1/a$. The C_4 symmetry is distorted by the anisotropy parameter ϵ, preserving reflection symmetry in the x and y-axes.

We use ratios of hopping parameters $t_2/t_1 = 0.32$, $t_3/t_2 = 0.5$, and compare two values of the band filling fractions $n_{\rm band} = 1.156$ and 0.875. (Band fillings are measured relative to a half filled band.) The corresponding Fermi energies at $\epsilon = 0$ are $E_F = 0$ and $E_F \approx -0.97\,t_1$ respectively, and are adjusted as ϵ is varied to keep $n_{\rm band}$ fixed. For both these band fillings the Van Hove singularity is below the Fermi level, see Fig. 7.1, but it is closest for $n_{\rm band} = 0.875$. We therefore expect a larger Nernst effect for that band filling than for $n_{\rm band} = 1.156$.

The Nernst coefficient is plotted in units of

$$\mathcal{N}_0 = \frac{t_1 a^4 Z_0}{\hbar\gamma_0} = \frac{\pi^2 k_B^2 T}{3\hbar^2}\frac{t_1 a^4}{\gamma_0}. \tag{7.43}$$

We show only $\mathcal{N}_{xy}$, since $\mathcal{N}_{yx}$ is related by

$$\mathcal{N}_{xy}(\epsilon) = -\mathcal{N}_{yx}(-\epsilon). \tag{7.44}$$

We compare three results for the Nernst coefficient:

- the exact solution of the linearized Boltzmann equation, from Eq. (7.27);
- the momentum-dependent relaxation-time approximation, from Eq. (7.34);
- Ziman's improvement on the relaxation-time approximation, from Eq. (7.37).

We have found that there is little difference between the momentum-dependent and momentum-independent relaxation-time approximations [Eqs. (7.34) and (7.36)], so we only plot the former. Results are shown in Figs. 7.2–7.4.

Fig. 7.2 shows that the relaxation-time approximation agrees well with the exact solution for nearly isotropic scattering ($\xi \ll a$). With increasing ξ small-angle scattering begins to dominate, and the relaxation-time approximation breaks down for $\xi \gtrsim 0.4\,a$. The break down occurs earlier for positive than for negative ϵ, which can be understood by considering the anisotropic curvature of the Fermi surface.[32]

In Fig. 7.3 we see that Ziman's improved approximation remains reliable over a somewhat larger range of ξ. Still, for a modestly large $\xi = 0.75\,a$ also Ziman's approximation has broken down completely, see Fig. 7.4, giving wrong magnitude and sign of the Nernst coefficient.

7.5 Conclusion

In conclusion, we have shown that the relaxation-time approximation is not a reliable method to calculate the Nernst effect in the combined presence of band and scattering anisotropies. The deficiencies are qualitative, even the sign of the effect can come out wrong. Of course, the relaxation-time approximation remains a valuable tool to assess the effects of band anisotropy in the case of isotropic scattering.

We have based our comparison on parameters relevant for the cuprates, [10] but we have only considered one possible mechanism (single-band elastic quasiparticle scattering) for the Nernst effect in cuprate superconductors. Other mechanisms (ambipolar diffusion, inelastic scattering, superconducting fluctuations) would require separate investigations.[6] It is hoped that the general framework provided here will motivate and facilitate work in that direction.

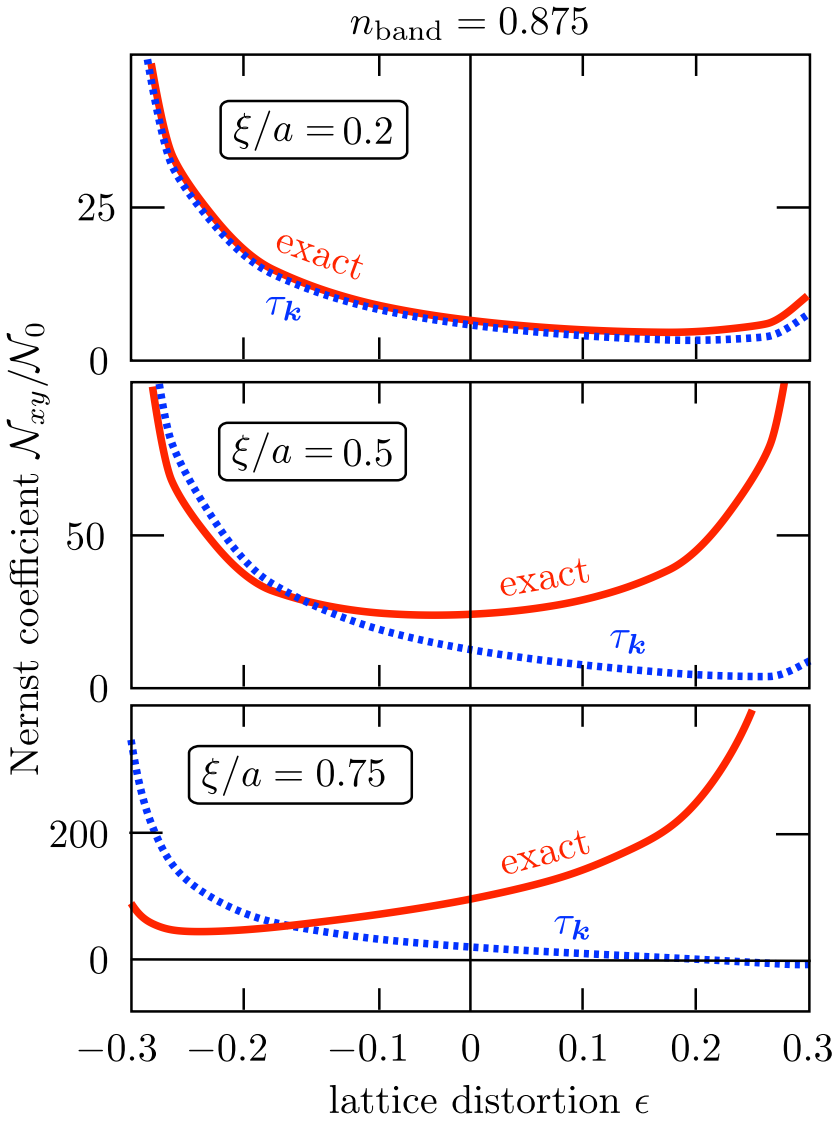

Figure 7.2. Dependence of the Nernst coefficient on the distortion ϵ of the square lattice at a fixed band filling $n_{\mathrm{band}} = 0.875$, for three different values of the range ξ of the scattering potential. The three panels show how the exact solution of the linearized Boltzmann equation (solid) starts out very close to the relaxation-time approximation (dotted) for nearly isotropic scattering, and then becomes progressively different as small-angle scattering begins to dominate.

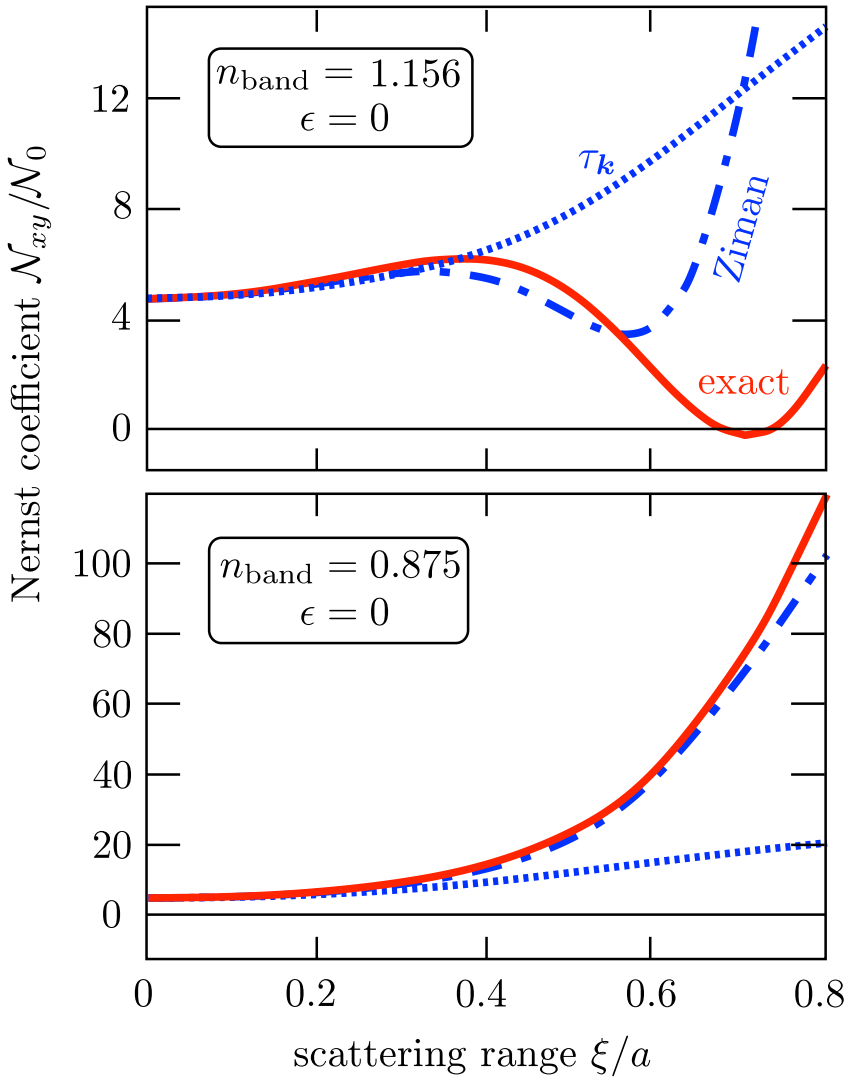

Figure 7.3. Dependence of the Nernst coefficient on the range ξ of the scattering potential, for an undistorted square lattice ($\epsilon = 0$). Two values of the band filling are shown in the upper and lower panel. The three curves in each panel correspond to: the exact solution of the linearized Boltzmann equation (solid), the relaxation-time approximation (dotted), and Ziman's improvement on the relaxation-time approximation (dash-dotted).

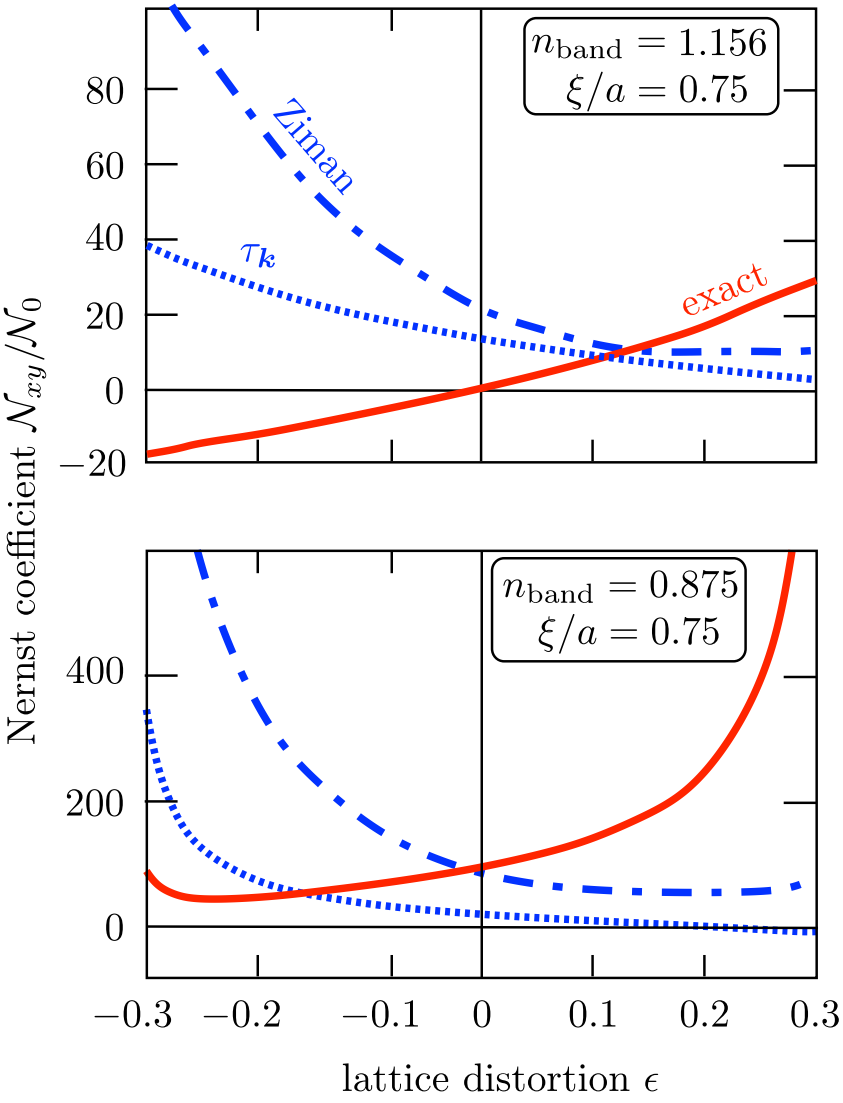

Figure 7.4. Same as Fig. 7.3, but now showing the dependence on the distortion ϵ of the square lattice for a fixed range $\xi = 0.75\,a$ of the scattering potential.

Bibliography

[1] R. T. Delves, Rep. Prog. Phys. **28**, 249 (1965).

[2] Z. A. Xu, N. P. Ong, Y. Wang, T. Kakeshita, and S. Uchida, Nature **406**, 486 (2000).

[3] M. N. Serbyn, M. A. Skvortsov, A. A. Varlamov, and V. Galitski, Phys. Rev. Lett. **102**, 067001 (2009).

[4] K. Michaeli and A. M. Finkel'stein, EPL **86**, 27007 (2009); Phys. Rev. B **80**, 115111 (2009).

[5] P. Kotetes and G. Varelogiannis, Phys. Rev. Lett. **104**, 106404 (2010).

[6] K. Behnia, J. Phys. Condens. Matter **21** 113101 (2009).

[7] S. Lambrecht and M. Ausloos, Phys. Rev. B **53**, 14 047 (1996).

[8] V. Oganesyan and I. Ussishkin, Phys. Rev. B **70**, 054503 (2004).

[9] A. Hackl and S. Sachdev, Phys. Rev. B **79**, 235124 (2009).

[10] A. Hackl and M. Vojta, Phys. Rev. B **80**, 220514(R) (2009).

[11] A. Hackl, M. Vojta, and S. Sachdev, Phys. Rev. B **81**, 045102 (2010).

[12] A. Hackl and M. Vojta, New J. Phys. **12**, 105011 (2010).

[13] C. Zhang, S. Tewari, and S. Chakravarty, Phys. Rev. B **81**, 104517 (2010).

[14] T. Valla, A. V. Fedorov, P. D. Johnson, Q. Li, G. D. Gu, and N. Koshizuka, Phys. Rev. Lett. **85**, 828 (2000).

[15] A. Kaminski, H. M. Fretwell, M. R. Norman, M. Randeria, S. Rosenkranz, U. Chatterjee, J. C. Campuzano, J. Mesot, T. Sato, T. Takahashi, T. Terashima, M. Takano, K. Kadowaki, Z. Z. Li, and H. Raffy, Phys. Rev. B **71**, 014517 (2005).

[16] J. Chang, M. Shi, S. Pailhés, M. Månsson, T. Claesson, O. Tjernberg, A. Bendounan, Y. Sassa, L. Patthey, N. Momono, M. Oda, M. Ido, S. Guerrero, C. Mudry, and J. Mesot, Phys. Rev. B **78**, 205103 (2008).

[17] A. Narduzzo, G. Albert, M. M. J. French, N. Mangkorntong, M. Nohara, H. Takagi, and N. E. Hussey, Phys. Rev. B **77**, 220502(R) (2008).

[18] E. Abrahams and C. M. Varma, Proc. Natl. Acad. Sci. USA **97**, 5714 (2000); C. M. Varma and E. Abrahams, Phys. Rev. Lett. **86**, 4652 (2001).

[19] L. Zhu, P. J. Hirschfeld, and D. J. Scalapino, Phys. Rev. B **70**, 214503 (2004).

[20] J. M. Ziman, *Principles of the Theory of Solids* (Cambridge University Press, Cambridge, 1972).

[21] M. C. Jones, Phys. kondens. Materie **9**, 98 (1969).

[22] R. Hlubina, Phys. Rev. B **64**, 132508 (2001).

[23] E. C. Carter and A. J. Schofield, Phys. Rev. B **66**, 241102(R) (2002).

[24] M. F. Smith and R. H. McKenzie, Phys. Rev. B **77**, 235123 (2008).

[25] E. H. Sondheimer, Proc. R. Soc. Lond. A **268**, 100 (1962).

[26] P. L. Taylor, Proc. R. Soc. Lond. A **275**, 200 (1963).

[27] J. M. Ziman, Adv. Phys. **10**, 1 (1961).

[28] R. Hlubina, Phys. Rev. B **62**, 11 365 (2000).

[29] J. P. Dahlhaus, C.-Y. Hou, A. R. Akhmerov, and C. W. J. Beenakker, Phys. Rev. B **82**, 085312 (2010).

[30] Y. Wang, Z. A. Xu, T. Kakeshita, S. Uchida, S. Ono, Y. Ando, and N. P. Ong, Phys. Rev. B **64**, 224519 (2001).

[31] E. H. Sondheimer, Proc. Roy. Soc. A **193**, 484 (1948).

[32] This note gives a qualitative explanation for why the relaxation-time approximation in Fig. 7.2 is better for negative than for positive ϵ. For $\epsilon > 0$ the Fermi surface has a small curvature in the x-direction and a large curvature in the y-direction. We have found that the relaxation-time approximation works better for smaller curvatures, being more accurate for $\Lambda_{k,x}$ than for $\Lambda_{k,y}$. For $\epsilon < 0$ the situation is reversed. Since $\mathcal{N}_{xy}$ is most sensitively affected by the energy dependence of $\Lambda_{k,y}$, the relaxation-time approximation is more accurate for $\epsilon < 0$ than for $\epsilon > 0$.

Samenvatting

Topologische supergeleiding is een nieuw verschijnsel, recentelijk voorspeld in dunne draden en wellicht ook al waargenomen. Het is een bijzondere supergeleidende toestand, die niet op basis van symmetrie maar op basis van topologie van de gewone supergeleidende toestand verschilt. Een kenmerk van topologische supergeleiding is het verschijnen van oppervlakte-toestanden. Het ligt voor de hand om te gaan onderzoeken hoe de bekende supergeleidende effecten in een topologische supergeleider optreden, en om wellicht nieuwe effecten te ontdekken. Dat is het hoofdonderwerp van dit proefschrift.

We beginnen met het onderzoek van de gebruikelijke thermodynamische eigenschappen van fase-overgangen, om te bezien hoe deze optreden bij een topologische fase-overgang. In een begrensd systeem is geen sprake van een scherpe overgang, en dus is het verschil tussen topologische en niet-topologische supergeleiders in een begrensd systeem geen scherp verschil. Dit lijkt in tegenspraak met eerder onderzoek, en in hoofdstuk 2 lossen we dit op. We identificeren een ander soort topologische fase-overgang, die de polen van de verstrooiingsmatrix in het complexe vlak betreft.

We vervolgen in hoofdstuk 3 met het onderzoek van de topologische fase in een heel algemeen model, geldig in de nabijheid van de fase-overgang. We laten zien dat de fase-overgang die de polen betreft niet samenvalt met de gebruikelijke overgang, maar wel in de buurt ervan ligt. We onderzoeken het universele gedrag van het geleidingsvermogen rond de beide overgangen.

In hoofdstuk 4 onderzoeken we opnieuw het geleidingsvermogen in een realistisch model van een supergeleidende dunne draad, zowel in de topologische als in de niet-topologische fase. We tonen aan dat het interferentie-effect dat zwakke antilocalisatie heet, omdat het 't ge-

leidingsvermogen zwak doet toenemen, een piek in de stroom-spanningskarakteristiek kan veroorzaken in de niet-topologische fase. Deze piek kan dus de zogenaamde Majorana-piek in de topologische fase verhullen. We brengen een verband aan tussen deze antilocalisatie piek en de eerder genoemde pool-overgang.

In hoofdstuk 5 vervolgen we het onderzoek van de supergeleidende draden met het bestuderen van het Josephson effect in de topologische fase. We leiden een algemeen geldig model af en onderzoeken de tijdsafhankelijkheid van de stroom bij constante spanning. Dit AC Josephson effect vertoont een ongebruikelijke ruis, met pieken bij frequenties die geen veelvoud van de Josephson frequentie zijn.

In hoofdstuk 6 stappen we over van de dunne draden naar het één-dimensionale kanaal aan de rand van een zogenaamde "quantum spin-Hall isolator". We laten zien dat een Josephson-junctie in dit systeem een onverwacht verschil vertoont tussen het Josephson effect met en zonder deeltjesbehoud. De superstroom kan twee keer zo groot worden met deeltjesbehoud.

Het proefschrift sluit af in hoofdstuk 7 met een geheel ander onderwerp uit de theorie van supergeleiding, namelijk het Nernst effect in hoge-temperatuur supergeleiders. Deze materialen hebben een anisotroop Fermi-oppervlak en anisotrope verstrooiing aan verontreinigingen. Deze complicatie is in de literatuur behandeld in de zogenaamde relaxatie-tijd benadering, maar wij tonen aan dat deze benadering fors tekort schiet. Zelfs het teken van het Nernst effect kan verkeerd uitkomen.

Summary

Topological superconductivity is a novel phenomenon, that has recently been predicted to exist in quantum wires. The first signatures of this new superconducting state have recently been reported. The difference with usual superconductors is the appearance of conducting edge states. It is of interest to investigate how all the well-known effects of superconductivity are modified by these edge states, and also to discover new effects that appear only in topological superconductors. This investigation is the main topic of the thesis.

We start with the examination of the usual thermodynamic properties of phase transitions, as they appear in topological phase transitions. Phase transitions become crossovers in finite systems, so strictly speaking, there are no topologically non-trivial finite systems. This apparent contradiction with previous research is discussed and resolved in chapter 2. Our analysis reveals a different type of topological transition in a finite system, concerning the poles in the complex energy plane of the scattering matrix.

We continue in chapter 3 with a study of the properties of the topological phase transition in a general model, universally valid near the transition. We show that the pole transition is displaced relative to the topological transition, but always occurs in its vicinity. We examine the universal behaviour of the conductance near the two transitions.

In chapter 4 we turn to the problem of the conductance of a realistic superconducting nanowire, both in the topological and non-topological regimes. We show that interference effect known as weak antilocalization, which enhances the conductance, may produce a zero-bias peak in the topologically trivial regime. It therefore may obscure the observation of the zero-bias peak due to topologically nontrivial Majorana bound states. We study both the average conductance and the conductance for

a single measurement. The zero-bias peak for a single measurement is explained in terms of the pole transition of chapters 2 and 3.

In chapter 5 we continue with the Josephson effect in topological superconductors. We derive a universal effective model of a Josephson junction and study its dynamics under constant voltage bias. We find an unexpected noise pattern, incommensurate with the Josephson frequency, which we call *any-*π Josephson effect.

In chapter 6 we compare long and short Josephson junctions at the edge of a Quantum Spin Hall insulator. We show that the long junction shows a difference between the parity-conserving and parity-non-conserving supercurrents, which can be measured in phase-insensitive measurements.

Finally, in chapter 7 we study the Nernst effect in superconductors with anisotropic Fermi surfaces and anisotropic scattering on impurities. We show that the widely accepted relaxation-time approximation fails to capture the features of the effect, to the extent that it may give a wrong sign of the Nernst coefficient.

List of Publications

1. *Penetration of hot electrons through a cold disordered wire*, A. S. Ioselevich and D. I. Pikulin, JETP Letters, **92**, 537 (2010).

2. *Topological properties of superconducting junctions*, D. I. Pikulin and Yu. V. Nazarov, JETP Letters, **94**, 693 (2011) [Chapter 2].

3. *Nernst effect beyond the relaxation-time approximation*, D. I. Pikulin, Chang-Yu Hou, and C. W. J. Beenakker, Phys. Rev. B **84**, 035133 (2011) [Chapter 7].

4. *Phenomenology and dynamics of a Majorana Josephson junction*, D. I. Pikulin and Yu. V. Nazarov, Phys. Rev. B **86**, 140504(R) (2012) [Chapter 5].

5. *Zero-voltage conductance peak from weak antilocalization in a Majorana nanowire*, D. I. Pikulin, J. P. Dahlhaus, M. Wimmer, H. Schomerus, and C. W. J. Beenakker, New J. Phys. **14**, 125011 (2012) [Chapter 4].

6. *Fermion-parity anomaly of the critical supercurrent in the quantum spin-Hall effect*, C. W. J. Beenakker, D. I. Pikulin, T. Hyart, H. Schomerus, and J. P. Dahlhaus, Phys. Rev. Lett. **110**, 017003 (2013) [Chapter 6].

7. *Two types of topological transitions in finite Majorana wires*, D. I. Pikulin and Yu. V. Nazarov, Phys. Rev. B **87**, 235421 (2013) [Chapter 3].

8. *Phase-locked magnetoconductance oscillations as a probe of Majorana edge states*, M. Diez, I. C. Fulga, D. I. Pikulin, M. Wimmer, A. R. Akhmerov, and C. W. J. Beenakker, Phys. Rev. B **87**, 125406 (2013).

9. *Proposal for the detection and braiding of Majorana fermions in a quantum spin Hall insulator*, Shuo Mi, D. I. Pikulin, M. Wimmer, and C. W. J. Beenakker, Phys. Rev. B **87**, 241405(R) (2013).

10. *Wigner-Poisson statistics of topological transitions in a Josephson junction*, C. W. J. Beenakker, J. M. Edge, J. P. Dahlhaus, D. I. Pikulin, Shuo Mi, and M. Wimmer, Phys. Rev. Lett. **111**, 037001 (2013).

Curriculum Vitæ

I was born in Arsamas-16, USSR on 10th of August 1987. I have completed my primary, secondary and high school education there. During my studies I participated in mathematics and physics Olympiads, winning the 2nd diploma in the National Physics Olympiad in 2004.

For my undergraduate studies I chose the Department of General and Applied Physics at the Moscow Institute of Physics and Technology in Dolgoprudniy. During my studies I was awarded scholarships from the funds "Dynasty" and "Charitable Foundation for the Development of Natural Science Innovation Education". My bachelor thesis "Non-equilibrium electron in a 1D disordered chain" and master thesis "Penetration of a non-equilibrium electron through a disordered system" were written under the encouraging supervision of Prof. Dr. Alexei Ioselevich.

After my graduation, I decided to continue my research in solid state physics and took the opportunity to join the group of Prof. Dr. Carlo Beenakker. I moved to the Netherlands and became a PhD student at the Instituut Lorentz, employed by the Foundation for Fundamental Research on Matter (FOM). I benefited a lot from the interactive environment in the group. I had a second supervisor Prof. Dr. Yuli Nazarov from the Technische Universiteit Delft who shared a very personal approach to physics with me.

During my PhD years, I was a teaching assistant for the course "Quantum Theory" of Dr. Peter Denteneer. I attended many schools, workshops and conferences and presented my work in Italy, Russia, Israel, France, USA, Vietnam, and the Netherlands.